UC Riverside
UC Riverside Electronic Theses and Dissertations

Title

Development of Nanofiber and Surface Plasmon Resonance Sensors for VOCs, Biochemical, and Bacterial Analysis

Permalink

https://escholarship.org/uc/item/04t6c00w

Author

Tran, Kelvin

Publication Date

2020

Copyright Information

This work is made available under the terms of a Creative Commons Attribution License, availalbe at https://creativecommons.org/licenses/by/4.0/

Peer reviewed|Thesis/dissertation

eScholarship.org Powered by the California Digital Library
University of California

UNIVERSITY OF CALIFORNIA
RIVERSIDE

Development of Nanofiber and Surface Plasmon Resonance Sensors for VOCs, Biochemical, and Bacterial Analysis

A Dissertation submitted in partial satisfaction
of the requirements for the degree of

Doctor of Philosophy

in

Environmental Toxicology

by

Kelvin Tran

March 2020

Dissertation Committee:
Dr. Quan Cheng, Chairperson
Dr. Wenwan Zhong
Dr. Ashok Mulchandani

Copyright by
Kelvin Tran
2020

The Dissertation of Kelvin Tran is approved:

Committee Chairperson

University of California, Riverside

Acknowledgements

Personal Acknowledgement

I would like to thank my advisor Prof. Jason Quan Cheng. Dr. Cheng has been supportive of me since I joined the lab as an undergraduate. I had joined the lab to experience academic research and the process of sensor development. I am grateful for the mentorship and guidance he provided. The freedom in the direction of the research that he encourages his students to partake allows us to learn and experience how to plan and implement experimental designs. While I was constantly focused on unexpected results, Dr Cheng would always encourage to think about the big picture and to approach the problem from a different angle. This mentality helped me stay sane and focused during times where there were little to no progress. I am thankful for his patience for there were several times where I had made mistakes, or my projects met dead ends. During these crisis, Dr. Cheng would always have time to examine the situation and give suggestions to overcome of these issues.

I would like to thank my mentor, Andrew Burris, for his mentorship when I first join the lab as an undergraduate and got me started on my first project that continued throughout my first year in this program. He is a great teacher and friend who has taught me a lot about research and optimization. Together we had published a paper that is detailed in chapter 2. I would also thank all the group members of Cheng lab, past and present, for their contributions and discussions. It was a joy working with this group of motivated and helpful individuals who are willing to set aside time to help or discuss about research.

Copyrights Acknowledgements

The text and figures in Chapter 2 of this dissertation, in part, are a reprint of the material as it appears in: Burris, A. J., et al. Tunable Enhancement of a Graphene/Polyaniline/Poly (ethylene oxide) Composite Electrospun Nanofiber Gas Sensor. Journal of Analysis and Testing **2017**, 1, 2, 12. The co-author listed in that publication, Andrew J. Burris, outlined the experimental design, fabricated the electrospinning setup, assembled the gas analyte testing chamber, and conducted the principle component analysis. The co-author listed in that publication, Prof. Quan Cheng, directed and supervised the research which forms the basis for Chapter 2.

\

This dissertation is dedicated to my family for their constant patience, love, support, and encouragement. I am thankful for my family who have encourage and supported me to pursue my dreams. A special thanks to my late grandmother who had always supported all her grandchildren to pursue our individual happiness, we all miss you very much.

ABSTRACT OF THE DISSERTATION

Development of Nanofiber and Surface Plasmon Resonance Sensors for VOCs, Biochemical, and Bacterial Analysis

by

Kelvin Tran

Doctor of Philosophy, Graduate Program in Environmental Toxicology
University of California, Riverside, March 2020
Dr. Quan Cheng, Chairperson

It is important to monitor potential exposure to various chemicals and toxicants that may adversely affect both human and environmental health. Biosensors have been developed to identify and quantify these analytes of interest in early warning systems and diagnosis devices. This dissertation implements nanomaterials, such as nanofibers and nanoparticles, into the biological recognition element of a biosensor for selectively and sensitively to detect trace analytes in either gas, liquid, or solid phases.

This dissertation is an agglomeration of several different projects that investigates the novel applications of nanomaterials into biosensor designs with two major application focuses: nanofibers and surface plasmon resonance (SPR) The first half of this dissertation focuses on the application of nanofiber surfaces for sensor developments. The nanofibers were fabricated through electrospinning and incorporated into various sensor designs. The first project develops polyaniline nanofibers into a chemiresistor sensor for sensitive detection of VOCs (small chain alcohols) by employing variants of reduced graphene oxides. The second project applies the nanofiber property of high surface area to volume ratio to maximize surface adsorption of EDTA-functionalized silver nanoparticles (AgNPs) as the biorecognition element of this sensor. The EDTA-AgNPs formulates a nickel ion bridge for selective capture and release of NTA and His tagged proteins that can be detected through fluorescent spectroscopy.

The second half of this dissertation transitions into the application of surface plasmon resonance for the development of biosensor signal transducers. The third project focused on combining the potential of 3D printing with gold nanoparticles (AuNPs) to create a novel integrated localized SPR (LSPR) sensor surface capable of sensitive protein detection. The synthesis of gold nanoparticles in-situ on a 3D printed prism surface enables the fabrication of a biosensor device for the disposable field of site usage with qualities comparable performances with sensors using commercial optical prisms. The last project focuses on developing an SPR experimental model of a double lipid bilayer membrane. This model mimics the unique structure of the double lipid bilayer membrane system found in the chloroplast, mitochondria, and gram-negative bacteria. This novel experimental model combined with SPR analysis creates a biosensor platform that enables the interrogation of chemical and protein interactions at interfaces such as the gram-negative bacteria cell wall and membrane system.

Table of Contents

List of Figures

List of Tables

Chapter 1: Electrospinning, Plasmonic Materials, and Lipid Bilayers for Sensor Interface of Chemical Analytes and Environmental Toxins.

1.1 Introduction.

As the incidents of chemical exposure escalate due to advancing technology fostering the tremendous increase of pharmaceutical drugs, consumer products, and toxic waste from productions. Demands to ascertain if exposure will consequently induce adverse effects and methods to mitigate these detriments will increase. *In vivo* studies have been extensively used to confirm toxicity results but suffer from prohibitive cost due to prolonged testing time required to raise, maintain, and sacrifice living animal test subjects utilized in series of experiments to confirm findings. While the *in vitro* study excels in identifying chemical pathways, it may suffer from inaccuracy due to the minimized scope of interaction of a living system that interacts with various external influences. This project aims to develop a biosensor pairing biological interactions with measurable responses that can facilitate chemical characterization, toxin interaction, and dose-responses at the cellular lipid membrane interface as a prime system for exploring primary molecular recognition events that are critical in understanding onset of adverse effects in organisms.

1.2 Biosensor.

The term biosensor refers to innovative analytical devices using a biological sensing element that can be applied to a wide range of applications areas of safety, monitoring, and medicine such as disease diagnosis, novel drug compound discovery, detecting trace chemicals and monitoring environmental conditions[1–5]. The biosensor is composed of two main components, a biologically sensitive element and a transducer element paired with an appropriate detector.

The biologically sensitive element is fabricated to interact with, bind, or recognize a specific target analyte through various methods that take advantage of bioreceptor pairing. The various combination of the biologically sensitive element and signal transducer element can form novel biosensors. There are six archetypes of bioreceptors used: 1) antibody/antigen, 2) enzyme/ligands, 3) RNA/DNA, 4) aptamers, 5) cells, or 6) biomimetic substrates. The transducer element transforms the signal of interaction into a measurable signal through physicochemical methods such: optical, piezoelectric, electrochemical, chemiluminescence, fluorescence, etc.

Biosensors utilizing antibody/antigen are commonly known as immunosensor as the target analyte is either the antigen or antibody that serves as a biomarker for the study[6–9]. The interaction between the antibody and antigen pair is akin a lock and key respectively such that the antibody typically only binds a single and specific antigen. The transducer of these binding pairs often relies on physicochemical changes combined with a reporter molecule, such as fluorescent probes, enzymes, or radioisotopes functionalized to either the antibody or antigen to generate a signal. The main benefit of utilizing this archetype is that the target selectivity of these binding pairs is well studied and can form various binding schemes of known interactions. There are several limitations of using antibodies in these sensors. A major concern in these sensors is the assay conditions as it can dramatically influence binding interaction between the antibody and antigen because this binding interaction can be highly sensitive to both the pH and temperature conditions of the assay. While the antibody-antigen interaction is robust, interference with the binding interaction can occur through stronger molecular interaction targeting either the antibody or antigen. It is noted that some antibodies are more promiscuous as it may bind several different antigens, akin to a puzzle piece that maybe slot in with several other pieces who share a similar binding segment, leading to non-specific binding and potential false positive/negative results. Careful optimizations of the experimental designs are required to allow these assays to perform at its peak sensitivity and selectivity.

Biosensors using enzyme/ligand paring are analytical devices that use an enzyme to generate a signal to measure the concentration of the present ligand[10–16]. The signal generated from the enzyme can be changes of 1) proton concentration, 2) consumption or production of specific compounds, 3) emission of light or heat, or 4) absorption/reflectance. The transducer element can convert this signal into a measurable unit: pH, current/potential, temperature, or absorption spectra through electrochemical, thermal, or optical methods. Detection of target analyte via enzymatic activity can be done in three major methods: 1) the enzymatic activity converts the target analyte into a product compound that can be easily detected, 2) turning on or off the enzymatic activity through activation or inhibition by the target analyte, or 3) monitoring changes in the enzymatic activity due to influences of the target analyte mainly through electrochemical or optical detection methods. With the catalytic property of the enzymes, it is possible to generate a large signal via the number of occurring reactions. The enzymatic activity has been well studied such that a single enzyme could be used to target various analytes through selecting its substrate, product, inhibitor/activator, and modulators as the target analyte of interest. Because covalent bonds are not typically involved in the enzymatic activity and are not consumed in the process, these types of biosensors can be continuously reused and only limited by the stability of the enzyme. Because the enzymes are highly specific and the catalytic activity can amplify the signal for lesser amounts, these sensors often have lower limits of detection compared to other binding techniques which are great for biosensor developments. However, like the antibodies, these enzymatic proteins are also influenced by its immediate environmental conditions works best in an optimize pH and temperature range with minimum external interferences from foreign molecular interactions.

Biosensors using RNA and/or DNA as part of the biological recognition system[17–26] often employs either one or a combination of the following: 1) complementary RNA/DNA sequence, 2) custom RNA/DNA oligomer sequences, or 3) specialized aptamers sequences. The transducer of these biosensors can translate the binding events into a quantifiable signal through 1) piezoelectric, 2) electrochemical, or 3) optical techniques. Single-strand RNA or DNA are well-known biomarkers involved in disease detection. The RNA biomarkers can be separated into two categories: 1) messenger RNA (mRNA), or 2) microRNA (miRNA). Messenger RNAs (mRNA) are large single-strand RNA transcribed from the RNA or DNA genome and are responsible for carrying information for protein translation. The detection of these mRNA is facilitated through fluorescently labeled single stand binding (SSB) proteins. However, these proteins will bind all single-strand DNAs and RNAs, so samples must be highly purified to accurately capture just the target strands. Micro RNA (miRNA) are small (~22 units) of non-coding RNA that is involved in RNA silencing and post-transcriptional regulation. The repression occurs by pairing with its targeted mRNA and induce cleavage of the target transcript which will cause gene suppression. The detection of these miRNA employs single-strand RNA that can be coupled with a fluorescence probe or immobilized on an electrode for the signal transducer. Another strategy centers around the aggregation of nanoparticles functionalized with complementary strands that will only aggregate upon the presence of the target strand. Probes for these can directly fish out the target strand from the sample and competitive binding to a mismatched strand can aid in suppressing non-specific binding as only the target strand will have a higher binding affinity than the mismatched probe.

Biosensors have utilized aptamers, an oligonucleotide or peptide sequence, as the biological recognition system for selective capturing of specific target molecules[27–33]. Sequential Evolution of Ligands by Experimental Enrichment (SELEX) is an iterative processed developed to screen a large library of ssRNA/ssDNA/peptides for selective binding of a specific target process and enrich the selected oligomers. A library of ssDNA, ssRNA, or peptide sequence is pre-generated based on ideal parameters that influence target binding. This pool of potential aptamers is screened with an affinity column functionalized with the target molecule, which will retain any viable aptamers on the column surface. The viable aptamers are eluted from the column, collected, and amplified via polymerase chain reaction (PCR). This pool of amplified aptamers is subjected to screening again to the same affinity column several times to enrich the aptamer pool, typically ending with a large pool of sequences (~10^6) that can bind to the target molecule. The aptamer of choice for target recognition will depend on desired binding interaction and often will employ the aptamer with the highest binding affinity for target-specific selectivity. There are various strategies employing aptamer for target selection. These aptamers have been paired with signal transducers for electrochemical, fluorescent, and plasmonic detection. While SELEX allows the fabrication of aptamers for various desired targets with high affinity, the screening process of a large pool of aptamers to identified optimal aptamer sequences can be costly and time-consuming.

Biosensors have employed whole cells as the biological recognition system to observe cellular response as environmental monitors for pollutants to a medical diagnosis of disease, and monitor drug-dosage responses[34–43]. These biosensor centers around a set of reporter genes and their regulatory proteins and monitors the changes in the regulation of the expression of the proteins as the signal transducer. These biosensors focus on analyzing the bioavailability for the rapid detection of pollutants and toxicants that are harmful to the cells. Bioavailability is a crucial factor to monitor as this determines the actual exposure amount that is biologically possible to a living organism. While bioavailability can estimate with traditional chemical analysis such as high-pressure liquid chromatography (HPLC), whole-cell sensors are much more sensitive to lower concentrations of these harmful analytes due to alteration during sample extraction. These sensors can be easily deployed for the field of site testing and can identify samples that contain a bioavailable contaminant.

The transducer elements for whole-cell biosensors center around changes in gene expression due to intercellular interaction with the target analyte. There are three key gene consecutive sequences that are required for this process: 1) the regulatory gene, 2) promoter gene, and 3) the reporter gene. The regulatory gene is responsible for coding a regulatory protein that can bind the targeted analyte. This regulatory protein is the biological recognition element within the cell cytosol. Once the analyte enters the cell, the regulatory protein will bind the analyte and enter the nucleus to act upon the promotor sequence downstream from the regulatory sequence. The interaction of the promotor sequence will alter gene expression levels in the reporter gene. The reporter gene is responsible for coding a reporter protein that can be optically observed when expressed. The physiochemical detectable signal from the lux (Bacterial luciferase) and luc (firefly luciferase) genes produces a bioluminescent signal, while the green fluorescent protein (GFP) produce a fluorescent signal. The lacZ (β-galactosidase) gene can be further modified to produce bioluminescence, fluorescence, colorimetric, or electrochemical signal[44–49]. These whole-cell biosensors can provide rapid and highly sensitive detection of targeted analytes with a variety of detection methods. But these sensors do have issues of strict requirements of temperature, O2, ATP, and substrates for cellular functions as well as low cellular permeability of some analytes.

Biosensors employing biomimetic structures have been developed as the biological recognition system to mitigate some of the issues from whole-cell biosensors[50–55]. This archetype takes the best attributes of the biological recognition elements such as the binding receptor proteins, cell membrane antigens, etc. from the whole-cell biosensors, and immobilizes it on a substrate to remove some of the strict biological requirements that are required to sustain the biorecognition process in living cells. These recognition elements can be extracted from the cells or synthesis of a structure that mimics the recognition function of these elements to replace proteins and the cellular membranes.

These biomimetic biosensors have utilized signal transducer that best matches the supporting substrates. Conductive substrates will often employ electrochemical or piezoelectric methods to measure the binding events on the surface. Optical detection can be achieved through labeling fluorescent probes or chemiluminescent enzymes onto secondary recognition elements for fluorescent and chemiluminescent detection of surface binding events. Alternatively, plasmonic surfaces such as gold and silver can provide a label-free optical detection method through surface plasmon resonance (SPR)[56–58] and localized SPR[59] to quantify these binding events. These biosensors can tailor to have high sensitivity (pM-nM) towards the target analyte of interest such that they have higher reproducibility and accuracy of detecting these analytes than whole-cell biosensors. Notably, these sensors require optimized experimental conditions to excel. False-positive/negative from non-specific binding, analysis time, ease of use, multiplexing, and high throughput capability are a few of the issues that are emphasized in biomimetic biosensor developments.

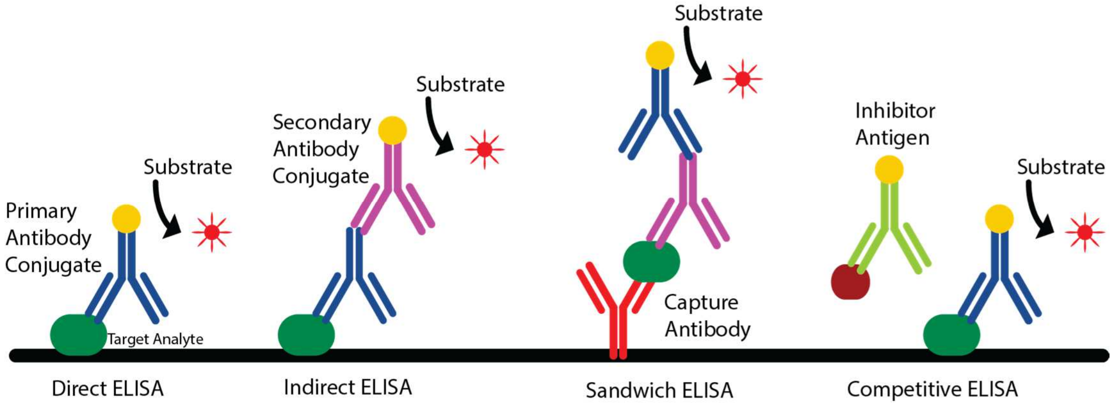

Figure 1.1. Four types of ELISA Assays: direct, indirect, sandwich, and competitive.

ELISA (enzyme-linked immunosorbent assay) is an analytical biochemistry assay that is often incorporated into biosensor designs[60,61]. ELISA centers around antibody-antigen pairing for the biological recognition element and conjugating an enzyme to the antibody for signal transducer element, often resulting in colorimetric change upon enzymatic reaction with substrate. Biosensor development will employ one of the four following types of ELISA assays: 1) direct, 2) indirect, 3) sandwich, and 4) competitive.

Direct ELISA is simple and straight forward. The antigen is adsorbed to the surface and then exposed to antibodies conjugated with enzymes that will facilitate a chemical reaction that will induce an observable colorimetric change measured by a spectrometer. Sandwich ELISA is a modification to the direct ELISA. It begins with coating the surface with capture antibodies before continuing with the procedures of the direct ELISA. This increases the capture of antigens to increase selectivity and sensitivity compared to direct ELISA. Competitive ELISA is a modified sandwich ELISA. The enzyme-conjugated antibodies will have a weaker binding interaction than the targeted antibodies. Upon exposure to the target antibodies in the sample, the targeted antibodies will outcompete the labeled antibodies on the surface, causing a detectable decrease in signal upon the presence of the targeted analyte. An alternative is that the surface is coated with unlabeled antibodies, and the signal is only observable when the labeled antibody with higher affinity outcompetes the unlabeled antibodies. This reversed setup aids in increasing selectivity towards the target analyte and aids in mitigating false positives. ELISA is one of the golden standards that biosensor development must compete against. ELISA has nanogram sensitivity and conducted in a 96 well plate, allowing for high throughput analysis of samples. One major issue that ELISA has is false positive from nonspecific binding of the labeled antibodies onto the surface.

Glucometer, a blood glucose biosensor, is a well notable example of a biosensor. These biosensors employ enzyme/ligand pairing as the biorecognition element with electrochemistry as the signal transducer. While the first blood glucose sensor used glucose oxidase and colorimetric analysis, these biosensors soon transitions to electrochemical detection. The glucose oxidase will convert glucose into gluconic aid and produce hydrogen peroxide as a byproduct[62,63]. The hydrogen peroxide will be oxidized at a catalytic anode and measures the electron transfers, allowing for indirect measurement of the glucose concentration. These devices provided a quick and accurate reading of blood glucose levels to aid in monitoring health and administering medication.

These blood glucose biosensors are a notable example of the transition of a clinical tool into handheld devices for point of care use by the patients.

Biosensor development is a growing field of interest for analytical, medical, industrial, and environmental purposes. There are many other notable biorecognition and transducer elements in found literature. The combination of various biorecognition elements and signal transducer provides customizations of a biosensor for specific analytes of interest. Advancement in biosensor development can arise from the novel application of materials improving biorecognition element and signal enhancement strategies to improve the sensitivity of the signal transducers.

1.3 Nanofibers.

Nanofibers are ultrathin fibers synthesized in the nanoscale through either electrochemistry or electrospinning. Fabricated from various polymers allow these fibers to have different properties that can be selectively optimized for scaffolds or sensor applications. The nanofibers provide advantages over their traditional counterparts of thin films, such as a high surface area to volume ratio, strong tensile property, and can be tailored for specific purposes across multiple applications. Electrospinning is a widely used technique for electrostatic fabrication of nanofibers from polymer solutions with diameters spanning from few nanometers to several microns. Electrospinning has been utilized extensively throughout literature[11,64–69] because of its versatility and ability to reproducibly fabricate continuous polymer fibers with nanometer diameters.

Electrospinning is an electrohydrodynamic process. A solution droplet is electrified with high voltage to produce a jet stream that will stretch and elongate to generate thinner fibers. The setup is quite simple and accessible to every lab (**Figure 1.2A**).

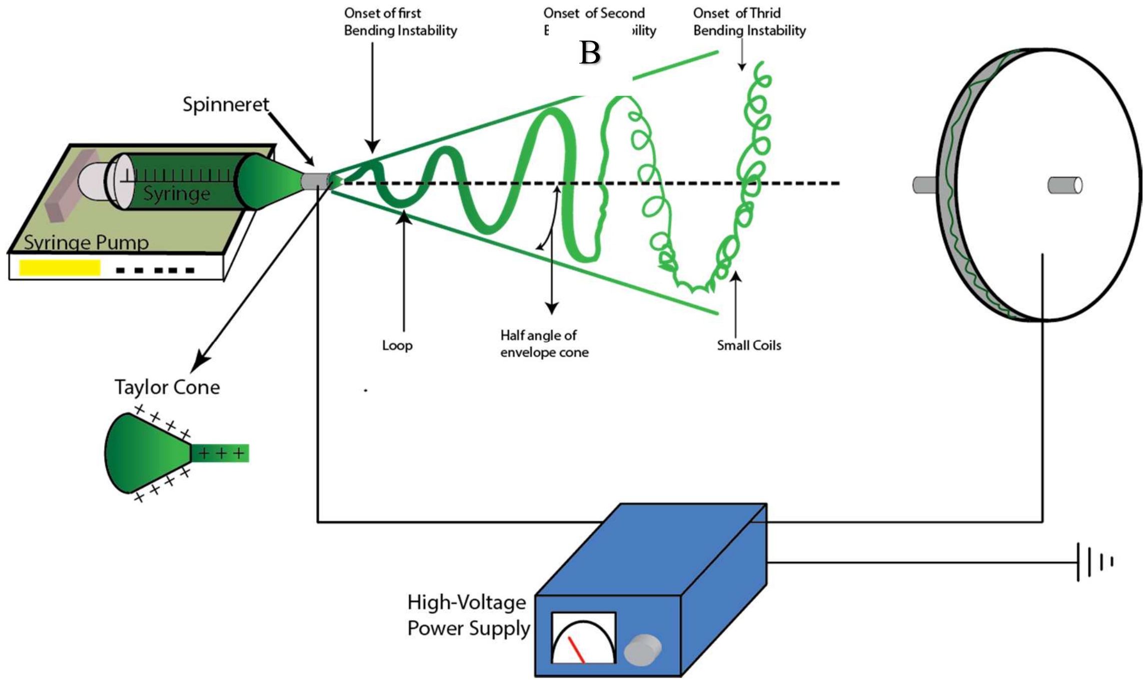

Figure 1.2 Basic setup for electrospinning. Diagram depicting the path of an electrospun jet.

The main components include a high voltage power supply, a syringe pump, a spinneret, and a conductive collector. The electrospinning process begins with polymer extruded from the spinneret or a blunt tip hypodermic needle to produce a pendant droplet because of surface tension. A Taylor cone is formed when the electrostatic repulsion among the surface causes the droplet to deform, and a charged jet is ejected[70–72]. The jet will initially travel in a straight line before undergoing vigorous whipping motion caused by bending instabilities. As the jet stretches into finer diameters, the solvent evaporates, and the solution solidifies quickly, leading to the deposition of solid fibers on the grounded collector.

The formation of the Taylor cone is an important process and is dependent on both the liquid's surface tension and applied charge. By applying high voltage, an external electric field is generated and acts upon the extruded droplet. To force the droplet into a conical shape to draw a jet stream, the strength of the electric field needs to surpass the capillary pressure caused by the surface tension of the droplet. This allows the electrostatic repulsion to be strong enough to overcome the surface tension and deform the droplet into the conical shape allowing the proper Taylor cone formation to guide the resulting jet towards the collection plate. As the jet travels towards the collection plate in a straight line, the diameter decreases monotonically, and the acceleration gradually drops to a constant.

After a certain distance, the straight jet is susceptible to instability because of the electrostatic repulsion of the surface charges. The jet is subjected to the far-field regime, which can be controlled by fine-tuning the physicochemical properties and the electrospinning parameters, (**Figure 1.2B**). Within this far-field region are two types of instabilities that can occur. The first is known as Rayleigh instability, an axisymmetric, which can lead to breaking up the jet into droplets. This instability is dictated by surface tension and can be mitigated using a strong electric field. The second type of instability is known as whipping or bending instability which is non-axisymmetric and is vital for the fabrication of ultrathin nanofibers.

These instabilities are caused by electrostatic repulsion among the surface charge. The jet is compelled to bend in the lateral electro stative force from, causing perturbations in a radial direction relative to the jet. This bending creates a lateral force perpendicular to the jet axis, which further promotes more bending perturbation to occur. Resulting in the jet trajectory to quickly bend at 90° angle and alters into a series of coils of continuous spirally and gradually thinning jet that oscillates at a high frequency. This causes the boundary of the jet to occupy a wide cone area as the whipping intensify, allowing elongation to occur and dramatically reduces the diameter of the jet as it continues towards the collection plate. Evaporation of solvent is a principal factor in this step as it will constantly reduce the volume and change viscoelastic parameters of the jet, which prevents large loop formation leading to thicker nanofibers. Literature has shown that the elongation of up to10,000 times can occur during the whipping process is vital for the formation of ultrathin nanofibers of nanometer dimensions.

To fine-tune the electrospinning process to control the fiber diameters, the following parameters are optimized: applied voltage, solution flow rate, and distance between needle tip and collector. These parameters will significantly influence the formation and structure of the produced nanofibers. Static DC high voltage is applied to generate the electric field with either negative or positive polarity that affects the distribution of the charged molecule within the surface of the jet. The critical voltage and correct charge are dependent on the solution and determine if fibers form or electrospraying occurs instead. While a higher voltage usually results in the formation of thinner fibers, it may also induce a higher ejection of fluid, resulting in fibers with thicker diameters.

Alternating current (AC) has been used to electrify the liquid for electrospinning, but the alternating current induces alternating segments of positive and negative charge with lengths dependent on the frequency of the AC potential. These alternating charged segments can cause bending instability within the jet hindering fiber elongation and forming thicker fiber. The frequency must be tuned so that it is fast enough to effectively electrify the liquid for electrospinning and allow bending instability to occur to elongate and thin the fibers. The collection of these formed threads may have an issue as these fibers do not readily attract toward grounded collector and can be deflected away. The parameter for the flow rate of liquid dictates how much material is available. An increase in flow rate will typically result in fibers with an enlarged diameter as the initial jet becomes thicker as the dynamics of the Taylor cone have changed. The working distance between the needle tip and collector determines the stage of the instabilities of the jet that is deposited. The longer distance is required to ensure full extension and solidification of the jet for thinner fiber formation. These parameters are interlinked, and all parameters must be adjusted to ensure optimized fiber formation of the desired size.

Electrospinning has utilized various polymers dissolved in an appropriate solvent to form nanofibers as the solution is stretched, elongated, and thinned by the whipping instability as the solvent evaporates. Both natural and synthetic polymers have been used in numerous studies to directly produce nanofibers. Example of these applications utilizes polystyrene (PS), poly (vinyl chloride) (PVC), etc. nanofibers for commercial application to protect the environment[64,73–75]. Biocompatible and biodegradable nanofibers composed from poly(ε-caprolactone) (PCL), poly (lactic acid) (PLA), etc. have been explored for scaffolds in biomedical applications. Natural biopolymers such as silk fibroin, dextran, collagen, etc. have been electrospun into nanofibers to explore the physical properties of these resources. Conductive polymers such as polyaniline (PANi)[64,76–80], polypyrrole (PPy)[81,82], etc. also have been fabricated into nanofiber to take advantage of piezoelectric and/or pyroelectric applications.

These solutions utilize an optimized organic solvent system to form a solution with high volatility to adjust the evaporation and solidification rate of the jet. If volatility is too high, the solution jet immediately solidifies and unable to form thin nanofibers. However, if volatility is too low, the fibers will still be wet when collected and swell due to the solvent content. Melts are a molten polymer solution that uses heat to aid in dissolve polymers that are difficult to dissolve in suitable solvents for solution electrospinning. It is necessary to add a heating device to keep the polymer in a molten state. After ejection, the molten polymer jet cools down and solidifies to generate fiber. Because of a lowered electrical conductivity and higher viscosity of the melts, the whipping instability of the jet is greatly reduced.

Small molecules can be directly integrated into the nanofiber during the electrospinning step if there are strong intramolecular interactions between such that these small molecules form self-assembled structures in solution. Similarly, colloidal particles[83] can also be doped into nanofibers if they are a certain size and don't affect the viscosity. Their incorporation can be improved with cross-linking polymer and dopant.

Composite nanofibers have been explored as a method to fabricate nanofiber of a novel material that cannot normally be electrospun by itself using a carrier polymer and removing it afterward. All these diverse types of functionalization increase the scope of application of electrospun nanofibers that can be tailored in size and property for the desired purpose.

1.4 3D Printing.

3D printing is an additive manufacturing process of fabricating three dimensional solid objects from a digital file. This 3D printing is done through fusing deposited material in a layer by layer process, which enables a wide range of complex shapes using less traditional manufacturing methods such as milling, subtractive manufacturing which cuts, and hollows out the substrate. This process enables rapid prototyping and mass production of custom objects for various applications[36,84–90]. The first application of 3D printing was in 1987 by Chuck Hull of 3D Systems utilizing stereolithography (SLA) process, which was quickly followed by other 3D printing technologies such as fused depositional modeling (FDM) by Stratasys and selective laser sintering (SLS) again by 3D Systems **(Figure 1.3)**. The prohibitive cost of these printers was restrictive and thus mainly used for industrial prototyping until these 3D printing technology patents expired in 2009, which opened the market from what used to exclusively be large $200,000 gigantic units to low-cost desktop 3D printers of $2,000.

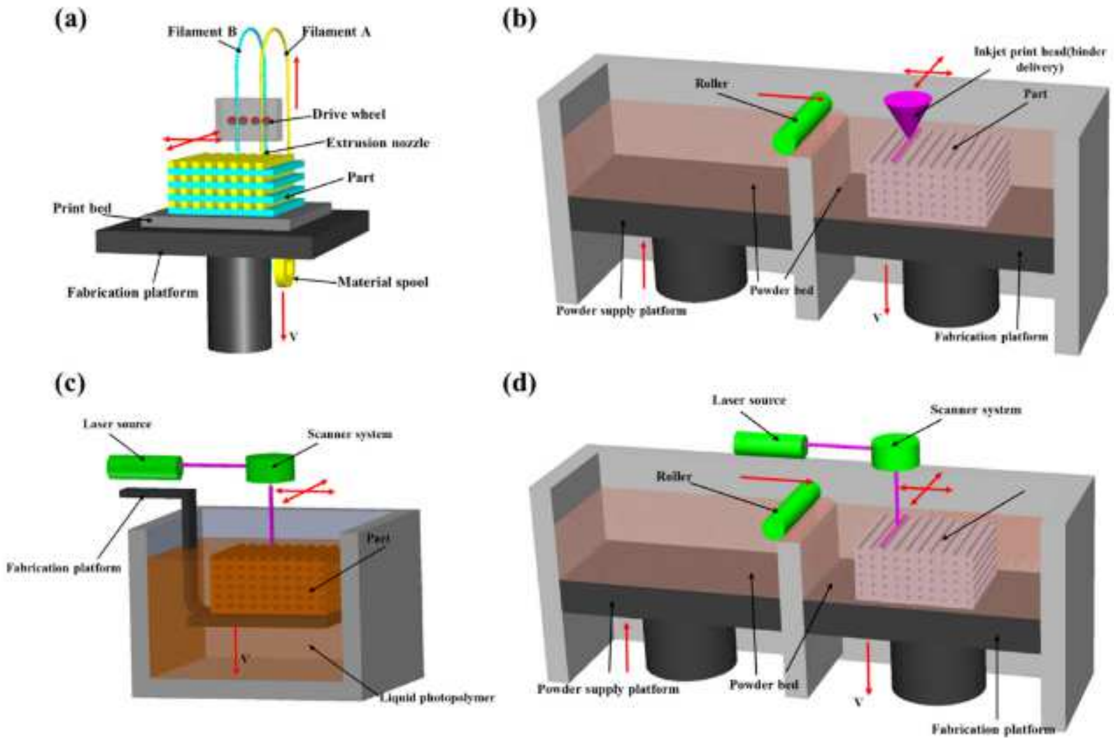

Figure 1.3 Schematic representation of a typical **(A)** FDM setup **(B)** Powder-liquid bed setup **(C)** SLA setup **(D)** SLS setup. Reprinted from Ref#90, Copyright 2017, with permission from Elsevier.

The principles of 3D printing can be divided into several categories: material extrusion, vat polymerization, material jetting, binder jetting, and powder bed fusion of polymers or metals. Out of these major branches of 3D printing, projects in this dissertation focuses on the vat polymerization technique and the advantages over the fusion deposition method (FDM) for our target application of optical components for sensor fabrication. Selective laser sintering (SLS) will also be discussed in this section as it is an exceptionally viable alternative to forming optical objects through porous silica sintering.

The fusion deposition method (FDM) is a layer by layer fabrication of a 3D object through melting and depositing substrates, commonly a spool of plastic filament[91] into the desired shape. This process is mechanized with motor controls to provide very precise movement of both the extrusion head and the stage to create seamless objects. The extrusion head equipped with a heated nozzle is responsible for melting the filament substrate and deposit material via motor controls. The molten substrate cools and solidifies, forming a single layer. The build platform shifts down to allow the next layer to form. The process continues until the object is fabricated. FDM is the most cost-effective method of producing custom thermoplastic objects for parts and prototypes. With a wide range of thermoplastic materials available, FDM is capable of prototyping and creating objects of various shapes, sizes, and properties. Objects made with thermoplastics can be recycled by melting the object into liquid form, conserving materials in cases of failed prototyping. But there are some flaws to FDM. It has the lowest dimensional accuracy and will have rough surfaces with visible seam lines from layering. It is also inherently anisotropic, which renders the fabricated objects unsuitable for critical applications.

Stereolithography (SLA) is a vat polymerization method that utilizing an ultraviolet (UV) light source to cure and solidify liquid resin in a vat through a layer by layer processes[84,92–94]. These printers are equipped with both a motorized build platform, and a mirror galvanometer to precisely cure preselected cross-sections of the resin. When a layer is complete, the build platform is moved away for a sweeper blade to recoat the scanning surface allowing for the next layer to be formed. The fully formed object may not be fully cured when completed, and additional post-processing under UV light is required. Unlike the thermoplastics of FDM, the liquid resin is solidified through photopolymerization by UV light exciting the photoinitiations, which catalyze the polymerization of thermoset polymers creating irreversible and unbreakable bonds. While SLA uses a single laser point to cure the resin, Digital Light Processing (DLP) is an advancement that takes advantage of a digital light projector to flash a single image of each layer at once, increasing the speed of production. The main advantage of utilizing a laser to cure resins in SLA and DLP is that these techniques can produce objects with extremely high dimensional accuracy with intricate details and exceptionally smooth surface finish. Along with a broad range of specialty material including clear, flexible, biocompatible resin (ceramic), and other materials tailored for specific interactions are available to produce custom objects that suit a variety of needs. However, objects fabricated in this fashion are often more brittle than FDM counterparts and not suited for physical functional prototypes and may degrade when exposed to prolonged UV radiation from the sun.

Selective laser sintering (SLS) is a powder bed fusion method utilizing powdered polymers[95,96]. The material is heated up to just below its melting point and thinly deposited on the build platform before a CO2 laser scans the surface of the powder bed. The printer selectively sinters the particles which bind them together in a predetermined pattern to form a single layer of the desired object. After a layer is complete, the build platformed is lower, and the process repeats, resulting in a bin containing the completed object surrounded by unsintered powder. While SLS printers are high-end industrial systems, the type of materials has good mechanical properties such as nylon, polystyrene, thermoplastics, polycarbonate, porous silica, etc. which further increases the materials available for 3D printing custom objects. Because the object is formed through sintering particles, the resolution is limited to the particle size distribution. Additionally, these objects tend to finish with a rough surface and internal porosity.

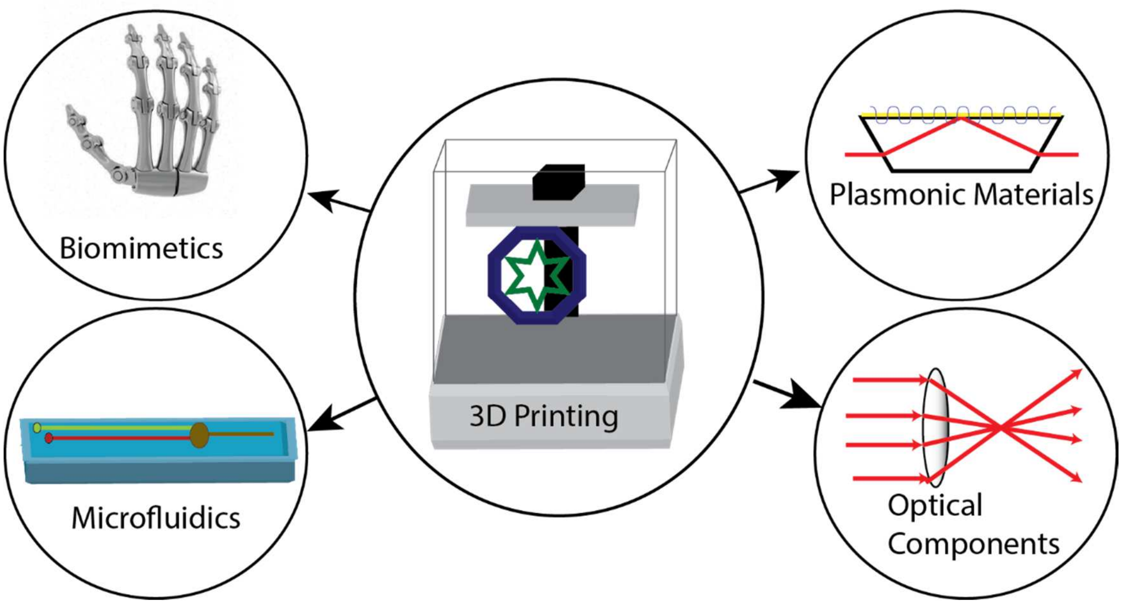

Figure 1.4 3D printing enables a wide range of applications. 3D printing's ability to prototype novel designs can be combined effectively with a range of optical techniques.

In the last decade, 3D printing has been focused on rapid prototyping and mass production of functional parts for industrial purposes. With the increase in availability, the application of 3D printing has risen around fabrication techniques for scientific equipment such as replacement parts, components, and devices. A major focus of this is sensor developments as 3D printing provides a reliable process of both rapid prototyping and mass production of microfluidic devices and other forms of sensors[85,98–103] (**Figure**

1.4). The investigation of applying 3D printing of optical components for sensor development has just begun[87,97]. Examples of forming glass objects from SLS technology have sparked interest in fabricating optical components. These works show that while SLS is capable of replicating glass components, these objects have issues with surface roughness and internal porosity affecting the light transversal path through the interface. Thus, the project in this dissertation utilizes SLA and clear resin as an alternative to form optically functional prisms that will be employ in this sensor development.

1.5 Surface plasmon resonance.

Surface plasmon resonance (SPR) is a nanomaterial facilitated optical phenomenon that has emerged as a robust technique for analytical chemistry and brought great enhancements to sensor developments. The main benefit of SPR is the ability to conduct a label-free analysis of protein affinity, lipid specificity, and a large collection of signal enhancement schemes.[57,58,104–108]

Principles and Theory. Surface plasmon resonance (SPR) is a phenomenon that occurs because of momentum transfer from an oscillating electromagnetic source such as light to a field of delocalized electron on metal surfaces. This transfer causes the free electrons to oscillate in resonance with the incoming incident light at the metal-dielectric interface, as depicted in **Figure 1.5a**. Several factors affect the conditions under which this transfer is possible. One of these factors has is keyed to the shape, size, and composition metal material. A key factor is the angular frequency of the incoming incident light, which dictates how much energy is available to be transferred to the surface. The last major factor is the dielectric constant of the metal and the surrounding media. The basis of common SPR set up utilize today was designed by Kretschmann and Raehter[109], forming a silver-air interface capable of generating plasmon waves through attenuated total reflection geometry.

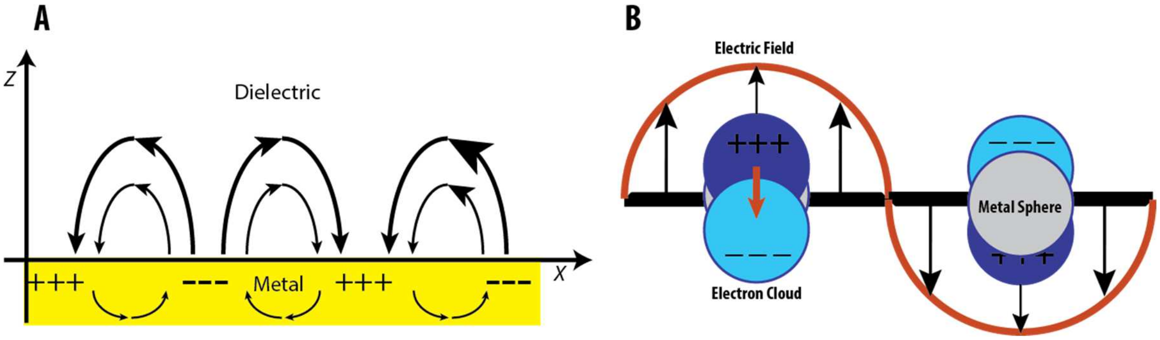

Figure 1.5 Schematic diagrams illustrating (A) a surface plasmon polariton (or propagating plasmon) and **(B)** a localized surface plasmon for SPR and LSPR, respectively.

The Otto configuration is another well-studied SPR set up that acts upon similar principles[111]. They take advantage of electrons collectively oscillating in resonance with the incident light source to generate a propagating plasmon wave at the metal-dielectric interface. Through their understanding, the many conditions critical for SPR to occur were discovered by their work.

$$k_{sp} = k_0 \sqrt{\frac{\varepsilon_m(\lambda)\varepsilon_s(\lambda)}{\varepsilon_m(\lambda) + \varepsilon_s(\lambda)}} \qquad \textbf{Eq1}$$

One of these conditions discovered deals with the coupling of the incident light to the metal's conduction electrons, which is only possible when the defined wavevector of incident light (k_0) is equal to the wavevector of the surface plasmon polaritons generated (k_{sp}) as defined in **Eq1**. Within this equation: λ is the wavelength of the incident light, ε_m is the dielectric constant of the metal, and ε_s is the dielectric constant of the surrounding medium on top of the metal (**Figure 1.5a**). SPR does not occur on all metal material because the dielectric constant is a complex value that is defined by both a real and imaginary component, $\varepsilon_m = \varepsilon_m' + i\varepsilon_m''$, thus only when a material possessing both a negative real component and a small imaginary component can the dielectric constant be satisfied to generate a surface plasmon wave. Given that ε_s can be reduced and redefined as n^2 (n = refractive index), SPR is sensitive to minute changes in the refractive index above the metal surface from sources such as large changes in buffer solutions, self-assemble monolayer adsorption, or molecular binding of protein or analyte of interest. This sensitivity promotes SPR development as novel binding techniques are developed to take advantage of this trait.

Because ksp is dependent on the dielectric constants, εm, εs, and k_{sp} cannot be equivalent to k_0 when freely traversing through a vacuum and thusly resonant conditions will not be met and no SPR occurs. This loss of angular momentum has been most commonly supplemented by guiding the incoming light through a high refractive index prism with ATR geometry to a thin metal surface deposited on the prism face. This will increase the effective wavevector of the incident light (k_{eff}) according to **Eq2**, n_D is the refractive index of the prism, and θ is the angle of the incident light striking the prism-metal interface, to reach resonance conditions necessary to generate observable SPR response. With this setup, surface plasmon polaritons are generated because k_{sp} is now equivalent to k_{eff}. This discovery allowed for adjustment of the coupling conditions to be tuned to a specific wavelength and or angle of the incident angle of the incoming light for many variations viable for different SPR setups. Under these conditions, the SPR phenomenon is observed as a dip in the reflectance spectrum of the surface material that shifts with incident angle or wavelength of light correspondingly in response due to changes in the dielectric constant es or increase of refractive index n_D.

$$k_{eff} = k_0 \, n_D \, \sin\theta = \frac{2\pi}{\lambda} \, n_D \sin\theta \qquad \textbf{Eq2}$$

The generated surface plasmon exponentially decays in the z-direction. Thus, after a certain total thickness of the sensor interface, the SPR phenomenon will no longer be detected. Penetration depth (δ_i) is utilized to determine how far any electromagnetic radiation, in this case, is the plasmon, can travel through the thin metal surface and what optimal range of distance from the substrate that measurements can be taken effectively. This distance is defined as the electric field of the surface plasmon decreases to 1/e of the maximum value expressed in **Eq3**. The penetration depth is estimated to be within 200nm when working with a 50nm thin gold film immersed in water.

$$\delta i = \frac{\lambda}{2\pi} \sqrt{\frac{{\varepsilon_m}' + \varepsilon_s}{\varepsilon_s}} \qquad \textbf{Eq3}$$

Localized Surface Plasmon Resonance (LSPR). Not only can surface plasmon can be generated on thin metal film as propagating polaritons, but surface plasmons can also be generated and contained onto discrete nanostructures in an event known as localized surface plasmon resonance (LSPR)[110,112,113]. This occurs in cases where the light interacts with nanoparticle structures that are much smaller than the wavelength of the incident light, generating surface plasmons that oscillate locally around the nanostructure (**Figure 1.5B**). This phenomenon results in amplifying the absorption and scattering properties of the nanomaterial. This effect is influenced by the nanoparticle shape, size, polarizability of the material used in the synthesis of the nanoparticle. Variation in these elements complexifies LSPR, which leads to computational work for complex modeling. There is a general relationship that can predict shifts in the wavelength of LSPR absorbance peak corresponding to changes in the dielectric refractive index of the surface interface as described in **Eq4**. This accounts for the changes in the bulk refractive index response of the nanoparticle (m), thickness in the altered layer of the dielectric (d), and the decay length of the LSPR field (l_d) is akin to the penetration depth of SPR (δi).

$$\Delta\lambda_{max} = m\Delta n\left[1 - exp\left(\frac{-2d}{l_d}\right)\right] \qquad \textbf{Eq}4$$

Despite the similarities between SPR and LSPR, many differences affect senor design. The plasmon is localized around the nanoparticles, the working range of plasmon detection is limited to 15nm in LSPR, compared to the 200nm of the thin gold film in SPR. Another difference is that while SPR utilizes a singular wavelength to probe changes in reflectivity due to SPR response of the sensor interface at a wide range of angles, LSPR utilizes a continuous spectrum of wavelength at a fixed angle to observe the shift in the absorption spectrum of the nanoparticle structures. Interestingly, because LSPR can be conducted either as colloids in solutions or immobilized on a solid support, LSPR can be utilized to enhance SPR as the plasmons can couple and generate greater sensitivity.

SPR Instrumentation. There are other variations in SPR configurations that employ different techniques to obtain equivalent results. The Otto configuration[111] has arranged space to exist between the metal and the total internal reflection surface such as a prism. Long-range SPR configurations allow the working area of plasmon detection to extend from 200nm up to microns. Plasmon waveguide resonance involves optical excitation of the plasmon of a thin metal film sandwich between a thicker dielectric film (silica) and the surface of a right-angle prism that excites both the S polarization found in conventional SPR and as well as the P polarization. The most commonly used in commercial and homebuilt instruments is an ATR set up known as “Kretschmann configuration”, developed by Kretschmann and Raether[109].

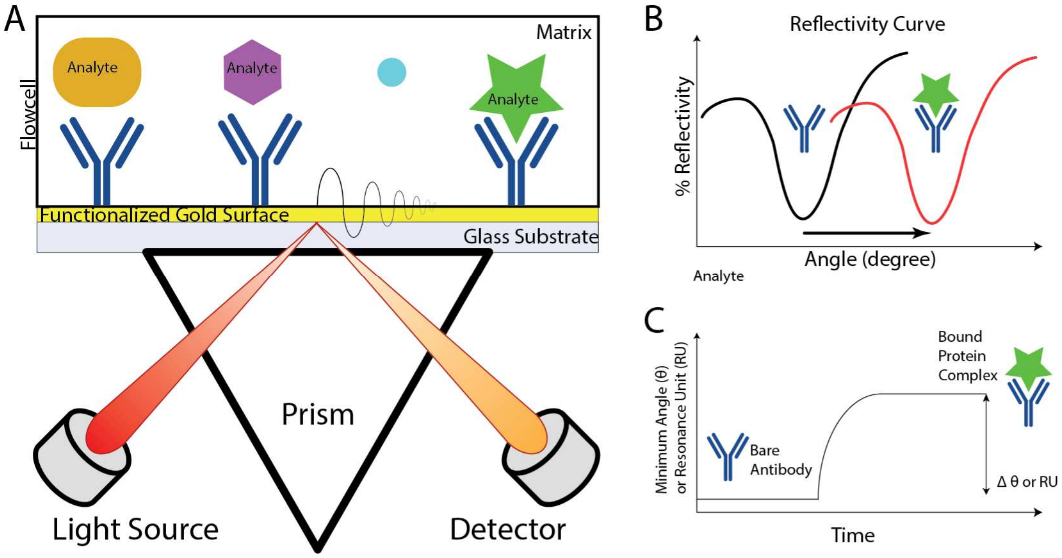

Figure 1.6 (A) Schematic of real-time biosensing on SPR interface upon analyte binding to plasmonic surface. The reflectivity curve **(B)** shifts right due to analyte binding and can be monitored in real-time with a sensorgram **(C)**.

Wavelength scanning instruments have simplified this setup even further by fixed light source specifically at an SPR active angle and spectrometer in place of the traditional CCD detector allowing for real-time analysis[58]. These slight changes in the resonance angle can be detected and measured in a reflectivity spectrum that exhibits a sharp dip due to excitement of the surface plasmon polariton and is expressed in either change in the degree of resonance angle or resonance unit (**Figure 1.6**). This high sensitivity to changes in the refractive index mitigates the needs of external fluorescent tags or radiolabels, enabling SPR methods to be label-free. Unlike endpoint assays, SPR data can be collected in real-time for protein binding and kinetics analysis. While conventional SPR suffers from a lack of multiplex analysis, SPR imaging has been developed the technique for high throughput analysis.

1.6 Lipid Membrane Modeling.

Because many toxins are required to enter the cell to act, it is important to understand how these compounds interact or bypass the plasma membrane, the cell's protective barrier. The plasma membrane is a complex interface that consists of various lipid groups, glycolipids, cholesterol, and transmembrane proteins. By creating a membrane model, it is possible to observe a toxin's initial interaction with the membrane, elucidating the toxin's mode of action. This information can aid in discovering new pathways for cures or preventive measures to combat these toxins.

Lipid membrane models have focused on a simplified system to represent single lipid bilayers for various applications such as proof of concepts, surface antigen recognitions, and molecular interactions. To mimic the lipid bilayer, not only the lipid and protein profile matters but so does the fluidity of the membrane. This fluidity grants semi-permeability, facilitating passive diffusion of small molecules such as oxygen, carbon dioxide, and hydrophobic molecules. Models of lipid membranes can be incorporated into biophysical sensors to help us understand protein interactions and dynamics. These sensors provide advantages over traditional cell assays, including the ability to tailor membrane surface for optimized assay reaction, minimize cellular interference, and increase reproducibility and reliability of interrogation of protein interactions[114–116].

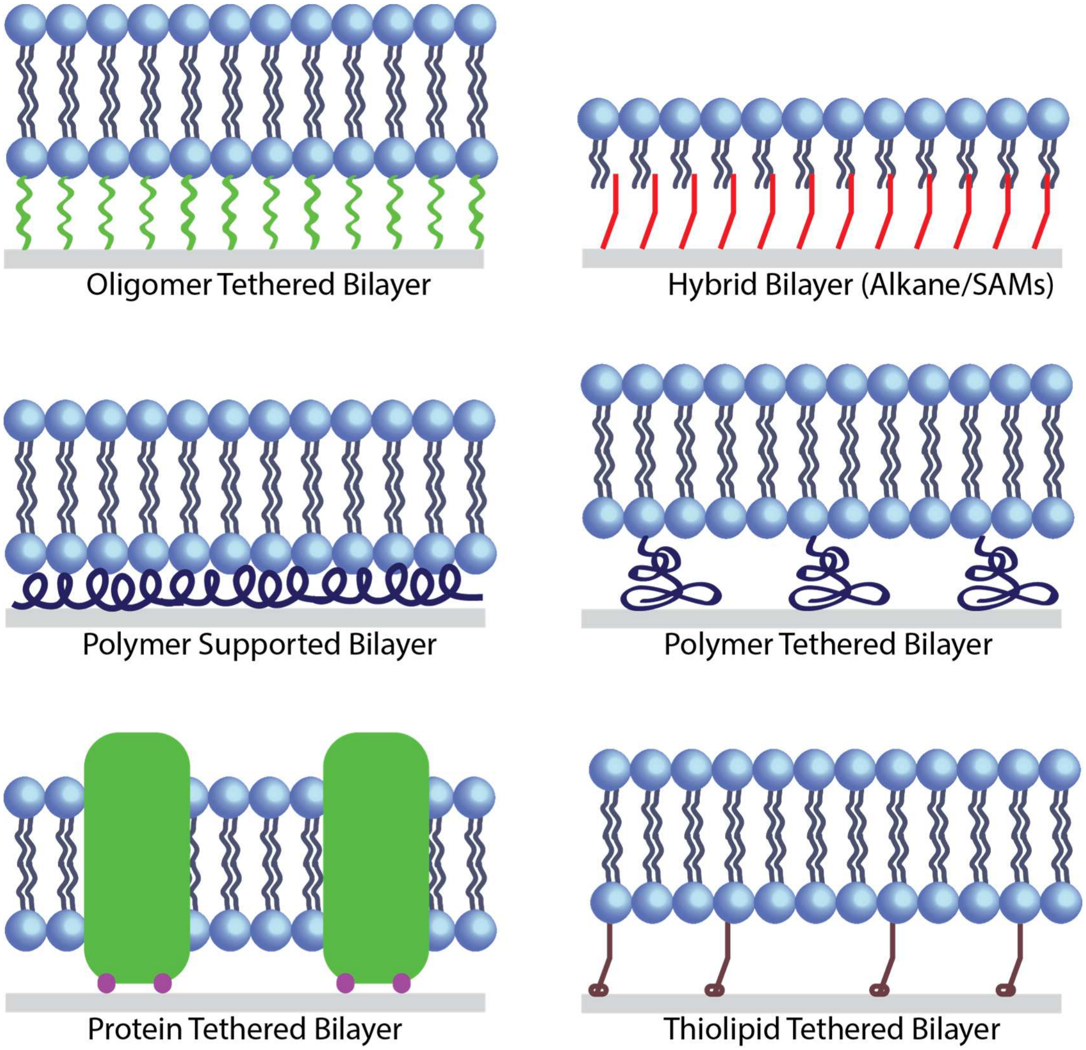

Figure 1.6 Lipid Bilayer Models. Design strategies for tethered lipid bilayers on solid supports. A wide range of tethering units can support the assembly of tethered lipid bilayers on solid supports.

Lipid bilayer membrane models used in conjunction with biophysical sensors have centered around four major archetypes[117]: 1) tethered lipid bilayer 2) hybrid lipid bilayer, 3) supported lipid bilayers, and 4) tethered lipid bilayers. The tethered models employ polymer, protein, and thiol to tether the membrane to the substrate (**Figure 1.6)**.

These single lipid bilayers can be tailored to specific reaction conditions and synthesized from a combination of synthetic lipids and or isolated lipids vesicles originated from either mammalian or bacterial cells to form bilayer facsimiles of their in vivo counterparts.

While single lipid bilayer has been extensively studied as computational[118,119] and experimental models[105,106,117,120], the double lipid bilayers are also an important system to model. Double lipid bilayer membranes are ubiquitous in nature, as they define vital organelles such as the mitochondria, chloroplasts, and gram-negative bacteria. Modeling these systems can improve our understanding of the complex protein machinery involved in these energy-producing organelles, and it can also help us uncover novel drug-membrane interactions of gram-negative bacteria[118,119,121]. These models will be better equipped than models of single lipid bilayers to study toxin interaction at the mitochondria and chloroplasts. By uncovering more compounds capable of interacting with the membranes, they can also aid the discovery of new antibiotics.

Recent literature demonstrates computational[122–124] and experimental models[125,126] of multi-lipid membrane layers. These models employ techniques such as tethered supported lipid bilayer[57,105,117,120,127–129], electrostatic interaction between lipid layers[130,131], and DNA hybridization[132–134] to form stacked lipid bilayers. These experimental models[124,135,136] form an imperfect double lipid bilayer membrane, with flawed incorporation of protein into the membrane, and even incomplete bilayers. The project in this dissertation employs an alternative method to form stacks of fully-formed and adherent bilayers by utilizing interactions between negatively-charged lipid headgroup and positively-charged polymer of poly-L-lysine[130,131]. These double lipid bilayer systems can be applied to biosensors to elicit a better understanding of protein-lipid interactions without cellular variance and interferences.

1.7 Dissertation Scope.

The goal of this thesis is to create a sensor from the novel application of nanomaterials for biosensor applications. The first half of this thesis focuses on utilizing nanofiber as the main substrate for sensor platforms for different purposes, while the second half shifts to the label-free optical detection method of SPR and LSPR. Chapter 2 is a collaborative work with another member of our lab, Andrew Burris, that focuses on applying nanofibers towards gas phase detection of volatile organic compounds like small chained alcohol. The main technique applied in the chapter was utilizing polyaniline (PANi) doped with camphor-sulfuric acid nanofiber as a chemiresistor for sensing application. Graphene oxide and various reduced states of graphene oxide were incorporated into the system to enhance the nanofiber's conductive property and increase sensitivity to the analyte. Nanofibers and thin films fabricated from the same solution were compared for their sensitivity, reproducibility, and recovery. By combining both sets of components into an array system using principal component analysis (PCA) to identify and quantify specific small chain alcohols exposed to the system.

Chapter 3 expands the nanofiber system towards a scaffold for nanoparticle aided extraction of protein measured by fluorescence. The nanofiber scaffold synthesized from polyvinyl alcohol (PVA) for increase biocompatibility was crossed linked via glutathione to promote fiber stability when exposed to an aqueous environment. Silver nanoparticles functionalized with ethylenediaminetetraacetic acid (EDTA) aid in the selective capture of the target analyte. The surfaces use the same traditional principles behind NTA columns. Upon exposure to a nickel ion solution, this surface could capture nitriloacetic acid (NTA) functionalized molecules or poly-histidine tagged (His-tagged) proteins for analysis. This capture scheme is reversible. The addition of EDTA can be introduced and outcompete the NTA and partial EDTA for the nickel ion chelation, removing the binding between the surface and the target analyte. In this work, fluoresce was utilized to verify and measure captured proteins analyte.

Chapter 4 begins the second half of the thesis as focus shifts from nanofibers to surface plasmon resonance (SPR), specifically localized SPR (LSPR) of nanoparticles immobilized for a setup akin SPR. This work also introduces 3D printing applied to the field of sensor development. Fabricating 3D printed prisms with the comparable optical quality of commercial optical prisms simplifies the experimental setup by fusing the sensing layer directly on the prism surface. The sensing layer comprised of nanoparticles was grown in-situ onto the prism surface. The surface is functionalized with DNA oligomers to aid in selective capture of target model protein, streptavidin. The quantification of captured protein was conducted via changes in the LSPR signal of the immobilized silver nanoparticles. This scheme can be further applied to target various analytes of interest.

Chapter 5 focuses on constructing a novel double lipid bilayer membrane model from stacking lipid bilayers with poly-L-lysine serving as the adhesive between the layers. SPR was used to monitor the fabrication of this lipid system at each step and quantify binding interactions that occur on this interface. Streptavidin and Cholera toxin was the model analytes studied to show the sensor capability to detect binding interactions. This novel interface has the potential to aid in the drug discovery process of compounds that acts upon these unique interfaces such as the membrane surfaces of mitochondria, chloroplast, and gram-negative bacteria. This work also investigated the use of Streptolysin O (SLO) to facilitate pore formation on the lipid bilayer to create a novel interface that uses the outer pore filled membrane as a size-selective barrier for analyte interaction occurring on the inner bilayer.

References

(1) Metkar, S. K.; Girigoswami, K. Diagnostic Biosensors in Medicine – A Review. *Biocatal. Agric. Biotechnol.* **2019**, *17*, 271–283.

(2) Carpenter, A. C.; Paulsen, I. T.; Williams, T. C. Blueprints for Biosensors: Design, Limitations, and Applications. *Genes (Basel).* **2018**, *9* (8).

(3) Mehrotra, P. Biosensors and Their Applications - A Review. *J. Oral Biol. Craniofacial Res.* **2016**, *6* (2), 153–159.

(4) Vigneshvar, S.; Sudhakumari, C. C.; Senthilkumaran, B.; Prakash, H. Recent Advances in Biosensor Technology for Potential Applications - an Overview. *Front. Bioeng. Biotechnol.* **2016**, *4* (FEB), 1–9.

(5) Morales, M. A.; Halpern, J. M. Guide to Selecting a Biorecognition Element for Biosensors. *Bioconjug. Chem.* **2018**, *29* (10), 3231–3239.

(6) Kang, J.; Kim, S.; Kwon, Y. Antibody-Based Biosensors for Environmental Monitoring. *Toxicol. Environ. Health Sci.* **2009**, *1* (3), 145–150.

(7) Sharma, S.; Byrne, H.; O'Kennedy, R. J. Antibodies and Antibody-Derived Analytical Biosensors. *Essays Biochem.* **2016**, *60* (1), 9–18.

(8) Byrne, B.; Stack, E.; Gilmartin, N.; O'Kennedy, R. Antibody-Based Sensors: Principles, Problems and Potential for Detection of Pathogens and Associated Toxins. *Sensors (Switzerland)* **2009**, *9* (6), 4407–4445.

(9) North, J. R. Immunosensors: Antibody-Based Biosensor. *Trends Biotechnol.* **1985**, *3* (7), 180–186.

(10) Justino, C.; Duarte, A.; Rocha-Santos, T. Recent Progress in Biosensors for Environmental Monitoring: A Review. *Sensors* **2017**, *17* (12), 2918.

(11) Bastürk, E.; Demir, S.; Danis, O.; Kahraman, M. V. Covalent Immobilization of α-Amylase onto Thermally Crosslinked Electrospun PVA/PAA Nanofibrous Hybrid Membranes. *J. Appl. Polym. Sci.* **2013**, *127* (1), 349–355.

(12) Jawaheer, S.; White, S. F.; Rughooputh, S. D. D. V.; Cullen, D. C. Development of a Common Biosensor Format for an Enzyme Based Biosensor Array to Monitor Fruit Quality. *Biosens. Bioelectron.* **2003**, *18* (12), 1429–1437.

(13) Simonian, A. L.; Grimsley, J. K.; Flounders, A. W.; Schoeniger, J. S.; Cheng, T. C.; DeFrank, J. J.; Wild, J. R. Enzyme-Based Biosensor for the Direct Detection of Fluorine-Containing Organophosphates. *Anal. Chim. Acta* **2001**, *442* (1), 15–23.

(14) Rocchitta, G.; Spanu, A.; Babudieri, S.; Latte, G.; Madeddu, G.; Galleri, G.; Nuvoli, S.; Bagella, P.; Demartis, M. I.; Fiore, V.; et al. Enzyme Biosensors for Biomedical Applications: Strategies for Safeguarding Analytical Performances in Biological Fluids. *Sensors (Switzerland)* **2016**, *16* (6).

(15) Kataria, M.; Swati, M.; Pathak, T.; Kumar, K. *Enzyme Based Biosensors and Their Applications*; Elsevier B.V., 2014.

(16) Fasoli, J. B.; Corn, R. M. Surface Enzyme Chemistries for Ultrasensitive Microarray Biosensing with SPR Imaging. *Langmuir* **2015**, *31* (35), 9527–9536.

(17) Liu, A.; Wang, K.; Weng, S.; Lei, Y.; Lin, L.; Chen, W.; Lin, X.; Chen, Y. Development of Electrochemical DNA Biosensors. *TrAC - Trends Anal. Chem.* **2012**, *37*, 101–111.

(18) Wu, Q.; Zhang, Y.; Yang, Q.; Yuan, N.; Zhang, W. Review of Electrochemical DNA Biosensors for Detecting Food Borne Pathogens. *Sensors (Switzerland)* **2019**, *19* (22).

(19) Hassan, R. A.; Heng, L. Y.; Tan, L. L. Novel DNA Biosensor for Direct Determination of Carrageenan. *Sci. Rep.* **2019**, *9* (1), 1–9.

(20) Carrascosa, L. G.; Huertas, C. S.; Lechuga, L. M. Prospects of Optical Biosensors for Emerging Label-Free RNA Analysis. *TrAC - Trends Anal. Chem.* **2016**, *80*, 177–189.

(21) Seefeld, T. H.; Halpern, A. R.; Corn, R. M. On-Chip Synthesis of Protein Microarrays from DNA Microarrays via Coupled in Vitro Transcription and Translation for Surface Plasmon Resonance Imaging Biosensor Applications. *J. Am. Chem. Soc.* **2012**, *134* (30), 12358–12361.

(22) Sohrabi, N.; Valizadeh, A.; Farkhani, S. M.; Akbarzadeh, A. Basics of DNA Biosensors and Cancer Diagnosis. *Artif. Cells, Nanomedicine Biotechnol.* **2016**, *44* (2), 654–663.

(23) Baeumner, A. J.; Cohen, R. N.; Miksic, V.; Min, J. RNA Biosensor for the Rapid Detection of Viable Escherichia Coli in Drinking Water. *Biosens. Bioelectron.* **2003**, *18* (4), 405–413.

(24) Halstead, J. M.; Lionnet, T.; Wilbertz, J. H.; Wippich, F.; Ephrussi, A.; Singer, R. H.; Chao, J. A. An RNA Biosensor for Imaging the First Round of Translation from Single Cells to Living Animals. *Science (80-.).* **2015**, *347* (6228), 1367–1370.

(25) Wang, Q.; Li, Q.; Yang, X.; Wang, K.; Du, S.; Zhang, H.; Nie, Y. Graphene Oxide-Gold Nanoparticles Hybrids-Based Surface Plasmon Resonance for Sensitive Detection of MicroRNA. *Biosens. Bioelectron.* **2016**, *77*, 1001–1007.

(26) Wang, J. SURVEY AND SUMMARY: From DNA Biosensors to Gene Chips. *Nucleic Acids Res.* **2000**, *28* (16), 3011–3016.

(27) Song, S.; Wang, L.; Li, J.; Fan, C.; Zhao, J. Aptamer-Based Biosensors. *TrAC - Trends Anal. Chem.* **2008**, *27* (2), 108–117.

(28) Bai, H.; Wang, R.; Hargis, B.; Lu, H.; Li, Y. A SPR Aptasensor for Detection of Avian Influenza Virus H5N1. *Sensors (Switzerland)* **2012**, *12* (9), 12506–12518.

(29) Zhang, W.; Liu, Q. X.; Guo, Z. H.; Lin, J. S. Practical Application of Aptamer-Based Biosensors in Detection of Low Molecular Weight Pollutants in Water Sources. *Molecules* **2018**, *23* (2), 12–16.

(30) Zhou, W.; Jimmy Huang, P. J.; Ding, J.; Liu, J. Aptamer-Based Biosensors for Biomedical Diagnostics. *Analyst* **2014**, *139* (11), 2627–2640.

(31) Zhang, Y.; Lai, B. S.; Juhas, M. Recent Advances in Aptamer Discovery and Applications. *Molecules* **2019**, *24* (5).

(32) Pehlivan, Z. S.; Torabfam, M.; Kurt, H.; Ow-Yang, C.; Hildebrandt, N.; Yüce, M. Aptamer and Nanomaterial Based FRET Biosensors: A Review on Recent Advances (2014–2019). *Microchim. Acta* **2019**, *186* (8).

(33) Mehlhorn, A.; Rahimi, P.; Joseph, Y. Aptamer-Based Biosensors for Antibiotic Detection: A Review. *Biosensors* **2018**, *8* (2).

(34) Gui, Q.; Lawson, T.; Shan, S.; Yan, L.; Liu, Y. The Application of Whole Cell-Based Biosensors for Use in Environmental Analysis and in Medical Diagnostics. *Sensors (Switzerland)* **2017**, *17* (7), 1–17.

(35) Heitzer, A.; Malachowsky, K.; Thonnard, J. E.; Bienkowski, P. R.; White, D. C.; Sayler, G. S. Optical Biosensor for Environmental On-Line Monitoring of Naphthalene and Salicylate Bioavailability with an Immobilized Bioluminescent Catabolic Reporter Bacterium. *Appl. Environ. Microbiol.* **1994**, *60* (5), 1487–1494.

(36) Dommati, H.; Ray, S.; Wang, J.; Chen, S. 3D Printing Technique for Ceramic Membrane Fabrication for Water Puri Fi Cation. **2019**, 16869–16883.

(37) Lin, C.; Zhang, Q. X.; Yeh, Y. C. Development of a Whole-Cell Biosensor for the Determination of Tyrosine in Urine for Point-of-Care Diagnostics. *Anal. Methods* **2019**, *11* (10), 1400–1404.

(38) Riangrungroj, P.; Bever, C. S.; Hammock, B. D.; Polizzi, K. M. A Label-Free

Optical Whole-Cell Escherichia Coli Biosensor for the Detection of Pyrethroid Insecticide Exposure. *Sci. Rep.* **2019**, *9* (1), 1–9.

(39) Gupta, S.; Saxena, M.; Saini, N.; Mahmooduzzafar; Kumar, R.; Kumar, A. An Effective Strategy for a Whole-Cell Biosensor Based on Putative Effector Interaction Site of the Regulatory Dmpr Protein. *PLoS One* **2012**, *7* (8).

(40) Gutiérrez, J. C.; Amaro, F.; Martín-González, A. Heavy Metal Whole-Cell Biosensors Using Eukaryotic Microorganisms: An Updated Critical Review. *Front. Microbiol.* **2015**, *6* (FEB), 1–8.

(41) Wan Jusoh, W. N. A.; Wong, L. S. Exploring the Potential of Whole Cell Biosensor : A Review in Environmental Applications. *Int. J. Chem. Environ. Biol. Sci.* **2014**, *2* (1), 52–56.

(42) Plotnikova, E. G.; Shumkova, E. S.; Shumkov, M. S. Whole-Cell Bacterial Biosensors for the Detection of Aromatic Hydrocarbons and Their Chlorinated Derivatives (Review). *Appl. Biochem. Microbiol.* **2016**, *52* (4), 347–357.

(43) Hansen, L. H.; Sørensen, S. J. Detection and Quantification of Tetracyclines by Whole Cell Biosensors. *FEMS Microbiol. Lett.* **2000**, *190* (2), 273–278.

(44) Girotti, S.; Ferri, E. N.; Fumo, M. G.; Maiolini, E. Monitoring of Environmental Pollutants by Bioluminescent Bacteria. *Anal. Chim. Acta* **2008**, *608* (1), 2–29.

(45) Chen, L.; Chen, L.; Dotzert, M.; Melling, C. W. J.; Zhang, J. Nanostructured Biosensor Using Bioluminescence Quenching Technique for Glucose Detection. *J. Nanobiotechnology* **2017**, *15* (1), 1–9.

(46) La Rosa, S. L.; Solheim, M.; Diep, D. B.; Nes, I. F.; Brede, D. A. Bioluminescence Based Biosensors for Quantitative Detection of Enterococcal Peptide - Pheromone Activity Reveal Inter-Strain Telesensing in Vivo during Polymicrobial Systemic Infection. *Sci. Rep.* **2015**, *5*, 8339.

(47) Alloush, H. M.; Lewis, R. J.; Salisbury, V. C. Bacterial Bioluminescent Biosensors: Applications in Food and Environmental Monitoring. *Anal. Lett.* **2006**, *39* (8), 1517–1526.

(48) Luo, J.; Liu, X.; Tian, Q.; Yue, W.; Zeng, J.; Chen, G.; Cai, X. Disposable Bioluminescence-Based Biosensor for Detection of Bacterial Count in Food. *Anal. Biochem.* **2009**, *394* (1), 1–6.

(49) Yeh, H.-W.; Ai, H.-W. Development and Applications of Bioluminescent and Chemiluminescent Reporters and Biosensors. *Annu. Rev. Anal. Chem.* **2019**, *12* (1), 129–150.

(50) Lu, L.; Hu, X.; Zhu, Z. Biomimetic Sensors and Biosensors for Qualitative and Quantitative Analyses of Five Basic Tastes. *TrAC - Trends Anal. Chem.* **2017**, *87*, 58–70.

(51) Malitesta, C.; Di Masi, S.; Mazzotta, E. From Electrochemical Biosensors to Biomimetic Sensors Based on Molecularly Imprinted Polymers in Environmental Determination of Heavy Metals. *Front. Chem.* **2017**, *5* (JUL), 1–6.

(52) Kozitsina, A. N.; Svalova, T. S.; Malysheva, N. N.; Okhokhonin, A. V.; Vidrevich, M. B.; Brainina, K. Z. Sensors Based on Bio and Biomimetic Receptors in Medical Diagnostic, Environment, and Food Analysis. *Biosensors* **2018**, *8* (2), 1–34.

(53) Hassler, B.; Worden, R. M.; Mason, A.; Kim, P.; Kohli, N.; Zeikus, J. G.; Laivenieks, M.; Ofoli, R. Biomimetic Interfaces for a Multifunctional Biosensor Array Microsystem. *Proc. IEEE Sensors* **2004**, *2*, 991–994.

(54) Wu, C.; Du, Y. W.; Huang, L.; Galeczki, Y. B. S.; Dagan-Wiener, A.; Naim, M.; Niv, M. Y.; Wang, P. Biomimetic Sensors for the Senses: Towards Better Understanding of Taste and Odor Sensation. *Sensors (Switzerland)* **2017**, *17* (12).

(55) Lee, J. H.; Jin, H. E.; Desai, M. S.; Ren, S.; Kim, S.; Lee, S. W. Biomimetic Sensor Design. *Nanoscale* **2015**, *7* (44), 18379–18391.

(56) Liu, Y.; Dong, Y.; Jauw, J.; Linman, M. J.; Cheng, Q. Highly Sensitive Detection of Protein Toxins by Surface Plasmon Resonance with Biotinylation-Based Inline Atom Transfer Radical Polymerization Amplification. *Anal. Chem.* **2010**, *82* (9), 3679–3685.

(57) Taylor, J. D.; Phillips, K. S.; Cheng, Q. Microfluidic Fabrication of Addressable Tethered Lipid Bilayer Arrays and Optimization Using SPR with Silane-Derivatized Nanoglassy Substrates. *Lab Chip* **2007**, *7* (7), 927–930.

(58) Linman, M. J.; Cheng, Q. J. Surface Plasmon Resonance: New Biointerface Designs and High-Throughput Affinity Screening. In *Optical Guided-wave Chemical and Biosensors I*; Zourob, M., Lakhtakia, A., Eds.; Springer Berlin Heidelberg: Berlin, Heidelberg, 2009; pp 133–153.

(59) Mejía-Salazar, J. R.; Oliveira, O. N. Plasmonic Biosensing. *Chem. Rev.* **2018**, *118* (20), 10617–10625.

(60) Enzyme-Linked Immunosorbent Assay (ELISA). *Bull World Heal. Organ.* **1976**, *54(2)*, 129–139.

(61) Weng, X.; Gaur, G.; Neethirajan, S. Rapid Detection of Food Allergens by Microfluidics ELISA-Based Optical Sensor. *Biosensors* **2016**, *6* (2), 1–10.

(62) Rahman, M. M.; Ahammad, A. J. S.; Jin, J. H.; Ahn, S. J.; Lee, J. J. A Comprehensive Review of Glucose Biosensors Based on Nanostructured Metal-Oxides. *Sensors* **2010**, *10* (5), 4855–4886.

(63) Yoo, E. H.; Lee, S. Y. Glucose Biosensors: An Overview of Use in Clinical Practice. *Sensors* **2010**, *10* (5), 4558–4576.

(64) Burris, A. J.; Tran, K.; Cheng, Q. Tunable Enhancement of a Graphene/Polyaniline/Poly(Ethylene Oxide) Composite Electrospun Nanofiber Gas Sensor. *J. Anal. Test.* **2017**, *1* (2), 12.

(65) Jo, S.; Kim, J.; Noh, J.; Kim, D.; Jang, G.; Lee, N.; Lee, E.; Lee, T. S. Conjugated Polymer Dots-on-Electrospun Fibers as a Fluorescent Nanofibrous Sensor for Nerve Gas Stimulant. *ACS Appl. Mater. Interfaces* **2014**, *6* (24), 22884–22893.

(66) Shi, Q.; Hou, J.; Zhao, C.; Xin, Z.; Jin, J.; Li, C.; Wong, S.-C.; Yin, J. A Smart Core-Sheath Nanofiber That Captures and Releases Red Blood Cells from the Blood. *Nanoscale* **2016**, *8* (4), 2022–2029.

(67) Bao, Y.; Fong, H.; Jiang, C. Manipulating the Collective Surface Plasmon Resonances of Aligned Gold Nanorods in Electrospun Composite Nanofibers. *J. Phys. Chem. C* **2013**, *117* (41), 21490–21497.

(68) Yanilmaz, M.; Lu, Y.; Dirican, M.; Fu, K.; Zhang, X. Nanoparticle-on-Nanofiber Hybrid Membrane Separators for Lithium-Ion Batteries via Combining Electrospraying and Electrospinning Techniques. *J. Memb. Sci.* **2014**, *456*, 57–65.

(69) Chen, D.; Lei, S.; Chen, Y. A Single Polyaniline Nanofiber Field Effect Transistor and Its Gas Sensing Mechanisms. *Sensors* **2011**, *11* (7), 6509–6516.

(70) Xue, J.; Wu, T.; Dai, Y.; Xia, Y.; States, U. Electrospinning and Electrospun Nano Fibers : Methods , Materials , and Applications. *Chem. Rev.* **2019**, *119*, 5298–5415.

(71) Haider, A.; Haider, S.; Kang, I. A Comprehensive Review Summarizing the Effect of Electrospinning Parameters and Potential Applications of Nanofibers in Biomedical and Biotechnology. *Arab. J. Chem.* **2018**, *11* (8), 1165–1188.

(72) Kong, C. S.; Yoo, W. S.; Jo, N. G.; Kim, H. S. Electrospinning Mechanism for Producing Nanoscale Polymer Fibers Electrospinning Mechanism for Producing. *J. Macromol. Sci. Part B Phys.* **2010**, *49*, 122–131.

(73) Chua, K.-N.; Chai, C.; Lee, P.-C.; Tang, Y.-N.; Ramakrishna, S.; Leong, K. W.; Mao, H.-Q. Surface-Aminated Electrospun Nanofibers Enhance Adhesion and Expansion of Human Umbilical Cord Blood Hematopoietic Stem/Progenitor Cells. *Biomaterials* **2006**, *27* (36), 6043–6051.

(74) Lin, Q.; Li, Y.; Yang, M. Polyaniline Nanofiber Humidity Sensor Prepared by Electrospinning. *Sensors Actuators, B Chem.* **2012**, *161* (1), 967–972.

(75) Lu, T.; Olesik, S. V. Electrospun Nanofibers as Substrates for Surface-Assisted Laser Desorption/Ionization and Matrix-Enhanced Surface-Assisted Laser Desorption/Ionization Mass Spectrometry. *Anal. Chem.* **2013**, *85* (9), 4384–4391.

(76) Chen, D.; Wang, C.; Chen, W.; Chen, Y.; Zhang, J. X. J. PVDF-Nafion Nanomembranes Coated Microneedles for in Vivo Transcutaneous Implantable Glucose Sensing. *Biosens. Bioelectron.* **2015**, *74*, 1047–1052.

(77) Gan, N.; Zhang, J.; Lin, S.; Long, N.; Li, T.; Cao, Y. A Novel Magnetic Graphene Oxide Composite Absorbent for Removing Trace Residues of Polybrominated Diphenyl Ethers in Water. *Materials (Basel).* **2014**, *7* (8), 6028–6044.

(78) Sutar, D. S.; Padma, N.; Aswal, D. K.; Deshpande, S. K.; Gupta, S. K.; Yakhmi, J. V. Preparation of Nanofibrous Polyaniline Films and Their Application as Ammonia Gas Sensor. *Sensors Actuators, B Chem.* **2007**, *128* (1), 286–292.

(79) Fratoddi, I.; Venditti, I.; Cametti, C.; Russo, M. V. Chemiresistive Polyaniline-Based Gas Sensors: A Mini Review. *Sensors Actuators, B Chem.* **2015**, *220*, 534–548.

(80) Pandey, S. Journal of Science : Advanced Materials and Devices Highly Sensitive and Selective Chemiresistor Gas / Vapor Sensors Based on Polyaniline Nanocomposite : A Comprehensive Review. *J. Sci. Adv. Mater. Devices* **2016**, *1* (4), 431–453.

(81) Qu, D.; Zheng, M.; Zhang, L.; Zhao, H.; Xie, Z.; Jing, X.; Haddad, R. E.; Fan, H.; Sun, Z. Formation Mechanism and Optimization of Highly Luminescent N-Doped Graphene Quantum Dots. *Sci. Rep.* **2014**, *4*, 5294.

(82) Haddour, N.; Cosnier, S.; Gondran, C. Electrogeneration of a Poly(Pyrrole)-NTA Chelator Film for a Reversible Oriented Immobilization of Histidine-Tagged Proteins. *J. Am. Chem. Soc.* **2005**, *127* (16), 5752–5753.

(83) Mahanta, N.; Valiyaveettil, S. Surface Modified Electrospun Poly(Vinyl Alcohol) Membranes for Extracting Nanoparticles from Water. *Nanoscale* **2011**, *3* (11), 4625.

(84) Ligon, S. C.; Liska, R.; Stampfl, J.; Gurr, M.; Mülhaupt, R. Polymers for 3D Printing and Customized Additive Manufacturing. *Chem. Rev.* **2017**, *117* (15), 10212–10290.

(85) Pi, H.; Tong, J.; Bian, C.; Xia, S. 3D Printed Micro / Nanofluidic Preconcentrator for Charged Sample Based on Ion Concentration Polarization. *J. Micromech. Microeng* **2017**, *27*, 55008(1-7).

(86) Gross, B.; Lockwood, S. Y.; Spence, D. M. Recent Advances in Analytical Chemistry by 3D Printing. *Anal. Chem.* **2017**, No. 89, 57–70.

(87) Hinman, S. S.; Mckeating, K. S.; Cheng, Q. Plasmonic Sensing with 3D Printed Optics. *Anal. Chem.* **2017**, No. 89, 12626–12630.

(88) Bhattacharjee, N.; Urrios, A.; Kang, S.; Folch, A. Lab on a Chip The Upcoming 3D-Printing Revolution in Microfluidics. *Lab Chip* **2016**, *16*, 1720–1742.

(89) Ngo, T. D.; Kashani, A.; Imbalzano, G.; Nguyen, K. T. Q.; Hui, D. Additive Manufacturing (3D Printing): A Review of Materials , Methods , Applications and Challenges. *Compos. Part B* **2018**, *143* (December 2017), 172–196.

(90) Wang, X.; Jiang, M.; Zhou, Z.; Gou, J.; Hui, D. 3D Printing of Polymer Matrix Composites : A Review and Prospective. *Compos. Part B* **2017**, *110*, 442–458.

(91) Popescu, D.; Zapciu, A.; Amza, C.; Baciu, F.; Marinescu, R. FDM Process Parameters in Fl Uence over the Mechanical Properties of Polymer Specimens : A Review. *Polym. Test.* **2018**, *69* (May), 157–166.

(92) Su, C. K.; Peng, P. J.; Sun, Y. C. Fully 3D-Printed Preconcentrator for Selective Extraction of Trace Elements in Seawater. *Anal. Chem.* **2015**, *87* (13), 6945–6950.

(93) Calderilla, C.; Maya, F.; Cerdà, V.; Leal, L. O. 3D Printed Device Including Disk-Based Solid-Phase Extraction for the Automated Speciation of Iron Using the Multisyringe Flow Injection Analysis Technique. *Talanta* **2017**, *175* (April), 463–469.

(94) Han, T.; Kundu, S.; Nag, A.; Xu, Y. 3D Printed Sensors for Biomedical Applications : *Sensors* **2019**, *19*, 1706–1728.

(95) Mazzoli, A. Selective Laser Sintering in Biomedical Engineering. *Med Biol Eng Comput.* **2013**, 245–256.

(96) Farid, S.; Shirazi, S.; Gharehkhani, S.; Mehrali, M.; Yarmand, H.; Simon, H.; Metselaar, C.; Kadri, N. A.; Azuan, N.; Osman, A. A Review on Powder-Based Additive Manufacturing for Tissue Engineering : Selective Laser Sintering and Inkjet 3D Printing. *Sci. Technol. Adv. Mater.* **2015**, *16* (033502).

(97) Lambert, A.; Valiulis, S.; Cheng, Q. Advances in Optical Sensing and Bioanalysis Enabled by 3D Printing. *ACS Sensors* **2018**, *3*, 2475–2491.

(98) Anciaux, S. K.; Geiger, M.; Bowser, M. T. 3D Printed Micro Free-Flow Electrophoresis Device. *Anal. Chem.* **2016**, No. 88, 7675–7682.

(99) Kataoka, E. M.; Murer, R. C.; Santos, J. M.; Carvalho, M.; Eberlin, M. N.; Augusto, F.; Poppi, R. J.; Gobbi, A. L.; Hantao, L. W. Simple, Expendable, 3D-Printed Micro Fl Uidic Systems for Sample Preparation of Petroleum. *Anal. Chem.* **2017**, No. 89, 3460–3467.

(100) Waheed, S.; Cabot, J. M.; Macdonald, N. P.; Lewis, T.; Guijt, R. M.; Breadmore, M. C. 3D Printed Microfluidic Devices: Enablers and Barriers. *Lab Chip* **2016**, *16*, 1993–2013.

(101) Dang, B. Van; Hassanzadeh-barforoushi, A.; Syed, M. S.; Yang, D. Microfluidic Actuation via 3D-Printed Molds toward Multiplex Biosensing of Cell Apoptosis. *ACS Sensors* **2019**, *4*, 2181–2189.

(102) Au, A. K.; Huynh, W.; Horowitz, L. F.; Folch, A. 3D-Printed Microfluidics. *Angew. Chemie - Int. Ed.* **2016**, *55*, 3862–3881.

(103) Meng, C.; Ho, B.; Ng, S. H.; Ho, K.; Li, H.; Yoon, Y. 3D Printed Microfluidics for Biological Applications. *Lab Chip* **2015**, *15*, 3627–3637.

(104) Moriwaki, H.; Yamada, K.; Nakanishi, H. Evaluation of the Interaction between Pesticides and a Cell Membrane Model by Surface Plasmon Resonance Spectroscopy Analysis. *J. Agric. Food Chem.* **2017**, *65* (26), 5390–5396.

(105) Taylor, J. D.; Linman, M. J.; Wilkop, T.; Cheng, Q. Regenerable Tethered Bilayer Lipid Membrane Arrays for Multiplexed Label-Free Analysis of Lipid−Protein Interactions on Poly(Dimethylsiloxane) Microchips Using SPR Imaging. *Anal. Chem.* **2009**, *81* (3), 1146–1153.

(106) Hinman, S. S.; Ruiz, C. J.; Drakakaki, G.; Wilkop, T. E.; Cheng, Q. On-Demand Formation of Supported Lipid Membrane Arrays by Trehalose-Assisted Vesicle Delivery for SPR Imaging. *ACS Appl. Mater. Interfaces* **2015**, *7* (31), 17122–17130.

(107) Chen, C. Y.; Hinman, S. S.; Duan, J.; Cheng, Q. Nanoglassified, Optically-Active Monolayer Films of Gold Nanoparticles for in Situ Orthogonal Detection by Localized Surface Plasmon Resonance and Surface-Assisted Laser Desorption/Ionization-MS. *Anal. Chem.* **2014**, *86* (24), 11942–11945.

(108) Duan, J.; Linman, M. J.; Cheng, Q. Ultrathin Calcinated Films on a Gold Surface for Highly Effective Laser Desorption/ Ionization of Biomolecules. *Anal. Chem.* **2015**, *82* (12), 5088–5094.

(109) Kretschman, E.; Raether, H. Radiative Decay of Non Radiative Surface Plasmons Excited by Light. *Naturforsch., A Astrophys. Phys. Phys. Chem* **1968**, No. November 1968, 2135–2136.

(110) Willets, K. A.; Duyne, R. P. Van. Localized Surface Plasmon Resonance Spectroscopy and Sensing. *Annu. Rev. Phys. Chem.* **2007**, No. 58, 267–297.

(111) Otto, A. Excitation of Nonradiative Surface Plasma Waves in Silver by the Method of Frustrated Total Reflection. *Zeitschrift ffir Phys.* **1968**, *410*, 398–410.

(112) Hall, W. P.; Ngatia, S. N.; Duyne, R. P. Van. LSPR Biosensor Signal Enhancement Using Nanoparticle - Antibody Conjugates. *J. Phys. Chem. C* **2011**, No. 115, 1410–1414.

(113) Wustholz, K. L.; Henry, A.; Mcmahon, J. M.; Freeman, R. G.; Valley, N.; Piotti, M. E.; Natan, M. J.; Schatz, G. C.; Duyne, R. P. Van. Structure - Activity Relationships in Gold Nanoparticle Dimers and Trimers for Surface-Enhanced Raman Spectroscopy. *J. Am. Chem. Soc.* **2010**, *132* (17), 10903–10910.

(114) Tanabe, M.; Ando, K.; Komatsu, R.; Morigaki, K. Nanofluidic Biosensor Created by Bonding Patterned Model Cell Membrane and Silicone Elastomer with Silica Nanoparticles. *Small* **2018**, *14* (49), 1802804.

(115) Osaki, T.; Takeuchi, S. Artificial Cell Membrane Systems for Biosensing Applications. *Anal. Chem.* **2017**, *89* (1), 216–231.

(116) Qiu, L.; Zhang, T.; Jiang, J.; Wu, C.; Zhu, G.; You, M.; Chen, X.; Zhang, L.; Cui, C.; Yu, R.; et al. Cell Membrane-Anchored Biosensors for Real-Time Monitoring of the Cellular Microenvironment. *J. Am. Chem. Soc.* **2014**, *136* (38), 13090–13093.

(117) Jackman, J. A.; Knoll, W.; Cho, N. J. Biotechnology Applications of Tethered Lipid Bilayer Membranes. *Materials (Basel).* **2012**, *5* (12), 2637–2657.

(118) Marrink, S. J.; Corradi, V.; Souza, P. C. T.; Ingólfsson, H. I.; Tieleman, D. P.; Sansom, M. S. P. Computational Modeling of Realistic Cell Membranes. *Chem. Rev.* **2019**, *119* (9), 6184–6226.

(119) Andoh, Y.; Okazaki, S.; Ueoka, R. Molecular Dynamics Study of Lipid Bilayers Modeling the Plasma Membranes of Normal Murine Thymocytes and Leukemic GRSL Cells. *Biochim. Biophys. Acta - Biomembr.* **2013**, *1828* (4), 1259–1270.

(120) Andersson, J.; Köper, I. Tethered and Polymer Supported Bilayer Lipid Membranes: Structure and Function. *Membranes (Basel).* **2016**, *6* (2).

(121) Pasenkiewicz-Gierula, M.; Baczynski, K.; Markiewicz, M.; Murzyn, K. Computer Modelling Studies of the Bilayer/Water Interface. *Biochim. Biophys. Acta - Biomembr.* **2016**, *1858* (10), 2305–2321.

(122) Sharma, S.; Kim, B. N.; Stansfeld, P. J.; Sansom, M. S. P. A Coarse Grained Model for a Lipid Membrane with Physiological Composition and Leaflet Asymmetry. *PLoS One* **2015**, *10* (12), 1–21.

(123) Wilson, B. A.; Ramanathan, A.; Lopez, C. F. Cardiolipin-Dependent Properties of Model Mitochondrial Membranes from Molecular Simulations. *Biophys. J.* **2019**, *117* (3), 429–444.

(124) Schindler, T.; Kröner, D.; Steinhauser, M. O. On the Dynamics of Molecular Self-Assembly and the Structural Analysis of Bilayer Membranes Using Coarse-Grained Molecular Dynamics Simulations. *Biochim. Biophys. Acta - Biomembr.* **2016**, *1858* (9), 1955–1963.

(125) Michel, J. P.; Wang, Y. X.; Kiesel, I.; Gerelli, Y.; Rosilio, V. Disruption of Asymmetric Lipid Bilayer Models Mimicking the Outer Membrane of Gram-Negative Bacteria by an Active Plasticin. *Langmuir* **2017**, *33*, 11028–11039.

(126) Andersson, J.; Fuller, M. A.; Wood, K.; Holt, A. A Tethered Bilayer Lipid Membrane That Mimics Microbial Membranes. *PCCP* **2018**, *20*, 12958–12969.

(127) Squillace, O.; Esnault, C.; Pilard, J.-F.; Brotons, G. Electrodes for Membrane Surface Science. Bilayer Lipid Membranes Tethered by Commercial Surfactants on Electrochemical Sensors. *ACS Sensors* **2019**, *4* (5), 1337–1345.

(128) Raguse, B.; Braach-Maksvytis, V.; Cornell, B. A.; King, L. G.; Osman, P. D. J.; Pace, R. J.; Wieczorek, L. Tethered Lipid Bilayer Membranes: Formation and Ionic Reservoir Characterization. *Langmuir* **1998**, *14* (3), 648–659.

(129) Wang, Z.; Wilkop, T.; Cheng, Q. Characterization of Micropatterned Lipid Membranes on a Gold Surface by Surface Plasmon Resonance Imaging and Electrochemical Signaling of a Pore-Forming Protein. *Langmuir* **2005**, *21* (23), 10292–10296.

(130) Heath, G. R.; Li, M.; Polignano, I. L.; Richens, J. L.; Catucci, G.; Shea, P. O.; Sadeghi, S. J.; Gilardi, G.; Butt, J. N.; Jeuken, L. J. C. Layer-by-Layer Assembly of Supported Lipid Bilayer Poly-L-Lysine Multilayers. *Biomacromolecules* **2016**, No. 17, 324–355.

(131) Heath, G. R.; Li, M.; Rong, H.; Radu, V.; Frielingsdorf, S.; Lenz, O.; Butt, J. N.; Jeuken, L. J. C. Multilayered Lipid Membrane Stacks for Biocatalysis Using Membrane Enzymes. *Adv. Funct. Mater.* **2017**, *27* (17).

(132) Hartman, K. L.; Kim, S.; Kim, K.; Nam, J.-M. Supported Lipid Bilayers as Dynamic Platforms for Tethered Particles. *Nanoscale* **2015**, *7* (1), 66–76.

(133) Chung, M.; Boxer, S. G. Stability of DNA-Tethered Lipid Membranes with Mobile Tethers. *Langmuir* **2011**, *27* (9), 5492–5497.

(134) Chung, M.; Lowe, R.; Chan, Y.-H. M.; Ganesan, P. V.; Boxer, S. G. DNA-Tethered Membranes Formed by Giant Vesicle Rupture Boxer*. *J. Struct Biol.* **2009**, *168* (1), 190–199.

(135) Maynard, J. A.; Lindquist, N. C.; Sutherland, J. N.; Lesuffleur, A.; Warrington, A. E.; Rodriguez, M.; Oh, S.-H. Next Generation SPR Technology of Membrane-Bound Proteins for Ligand Screening and Biomarker Discovery. *Biotechnol J.* **2019**, *4* (11), 1542–1558.

(136) Robertson, J. L. The Lipid Bilayer Membrane and Its Protein Constituents. *J. Gen. Physiol.* **2018**, *150* (11), 1472–1483.

Chapter 2: Electrospun Nanofiber and Drop-Cast Film Sensors of Tunable Graphene/Polyaniline/Poly (ethylene oxide) Composites

2.1 Introduction.

The detection of harmful airborne compounds is important to maintain and protect human health in both industrial and domestic environments. Accurate and precise measurement of gaseous compounds using traditional analytical techniques can be tedious and expensive. Thus, innovation for rapid and economical advances, alongside portability and real-time analysis, has been in demand for new methods and sensor development. Electrospinning, an electrostatic fiber fabrication method, enables the production of continuous polymer fibers with diameters ranging between a few nanometers to several microns. Electrospun nanofiber has been applied as solid-state sensors due to their advantages such as high surface area, mechanical properties, cost efficiency, facile fabrication, and modification potential[1–3].

Polyaniline (PANi) is a conductive polymer that has been electrospun into nanofibers for chemiresistor sensors due to the facile fabrication and excellent electrical and mechanical properties[4–7]. These PANi sensors have detected many gases, including ammonia (NH3), nitrogen dioxide (NO2), hydrogen sulfide (H2S), hydrogen (H2), and carbon monoxide (CO)[8–11]. To improve the fiber performance, (+)-camphor-10-sulfonic acid (HCSA) have been doped into the nanofiber matrix to modify the PANi nanofiber conductivity. However, there is difficulty in fabricating nanofibers from a PANi/HSCA solution due to the low molecular adhesion of the polymer due to the low molecular weight and rigid backbone structure[12–14]. Thus, poly(ethylene oxide) (PEO) has been added to assist the electrospinning fabrication of PANi-based nanofibers, resulting in a conductive composite nanofiber[15,16]. These composite nanofibers can be tuned for selectivity, response time, robustness, and further modification by additional dopants, such as graphene.

Graphene, a single-atom-thick sheet of sp2 hybridized carbon atom network, is well known for its unique electrical and chemical properties. Graphene has been used in sensing applications for its high specific surface area, mechanical flexibility, and high conductivity. While there are a few reported work of PANi/PEO/Graphene nanofibers and comparing its properties to PANi/PEO nanofibers, there are few applications of this composite nanofiber for sensor applications[17,18]. Sensing applications of graphene have focused on variants of reduced graphene oxides (rGO) and its interaction with gaseous analytes[19–21]. Graphene oxide (GO) readily interacts with gaseous analytes through the oxygen-containing functional group on the surface. While conductivity increases as a higher degree of reduction occur on the GO, the loss of the oxygen-containing functional group reduces surface functionality and solubility in organic solvents. However, it is known that partially reduced graphene oxide contains the benefits of both GO and rGO, as it has an optimal balance between chemical adsorption capacity provided by GO and electronic characteristics of rGO which are key factors for gas sensor development.

In this chapter22, electrospun composite PANi/HSCA/PEO nanofibers were functionalized by doping variants of reduced graphene oxides (rGOs) and examined its capability as a room temperature gas sensor. Chemical and thermal reduction of GO generated two sets of rGO denoted as crGO and trGO, respectively. The time allotted for the chemical reduction process was further modified to 6 hours or 12 hours to form two variants noted as crGO-6 and crGO-12 for the indicated reaction time. Additionally, the temperature for the thermal reduction process was also adjusted to 500 ºC or 900 ºC to create two more variants noted as trGO-500 and trGO-900. These rGO variants were used to tune the nanofiber sensitivity towards the gaseous analytes. Thin-film sensors were fabricated from the electrospinning solutions with the rGO variants. The performance of both the nanofiber and thin-film sensors were compared. A sensor array utilizing all the rGO variant components in conjunction with principal component analysis was used to successfully identify the gaseous analytes: methanol, ethanol, and 1-propanol.

2.2 Experimental Detail.

Materials. Polyaniline (PANi) emeraldine base (Mw = 65,000), (1S)-camphor-10-sulfonic acid (HCSA), polyethylene oxide (PEO) (Mw = 2,000,000), sulfuric acid (H_2SO_4), potassium persulfate ($K_2S_2O_8$), phosphorus pentoxide (P_2O_5), potassium permanganate ($KMnO_4$), hydrogen peroxide (H_2O_2, 30%), hydrochloric acid (HCl), trisodium citrate ($Na_3C_6H_5O_7$), chloroform ($CHCl_3$), dimethylformamide (DMF), methanol (MeOH), ethanol (EtOH), and 1-propanol (PrOH) were purchased from Sigma-Aldrich (St. Louis, MO). Graphite powder was purchased from Alfa Aesar (Haverhill, MA).

Instrumentation. A Lindberg/Blue M tube furnace (Thermo Fisher, Waltham, MA) was used for thermal reduction of graphene oxide. PTFE syringe filters (0.45 µm) were purchased from Scientific Strategies (Yukon, OK). Interdigitated microelectrodes were purchased from Case Western University, OH. The electrospinning setup utilize a syringe pump (KD Scientific, 200 Series) and a high voltage power supply (Spellman CZE1000R).

Atomic force miscopy (AFM) and Raman characterization was conducted on an OmegaScope™ 1000 from AIST-NT (Novato, CA). SEM imaging was conducted on a Hitachi TM-1000 (Tokyo, Japan). The electrical conductivity was monitored using a Keithley 236 electrometer (Cleveland, OH).

Graphene oxide preparation. Graphene oxide (GO) was synthesized from graphite powder using a modified Hummer's method[23]. Initial 2 g of graphite powder, 1 g K2S2O8, and 1 g P2O5 was mixed with 20mL of concentrated H2SO4 at 80˚C under constant stirring with a reflux condenser for an hour. The resulting mixture turns dark blue and is cooled to room temperature before diluting (tenfold) with ultrapure water, filtered, and washed. After drying the graphene oxide overnight, the GO is mixed in 46 mL of ice-cold concentrated H2SO4, followed by the gradual addition of 6 g KMnO4. The solution is mixed at 35˚C for 2 hours and diluted with 375 mL ultrapure water. Dropwise addition of 5 mL of 30% H2O2 proceeded to quench the reaction. The resulting yellow solution is filtered and washed with dilute HCl. The graphene oxide solution is further purified by several rounds of dialysis. Sonication of the suspension produced a uniform yellow-brown GO solution, which was then subjected to centrifugation to remove unreacted graphite.

Reduction of graphene oxide. The graphene oxide was reduced by two methods: 1) thermal or 2) chemical methods. Two sets of thermal reduction of GO was carried out in a tube furnace in forming gas atmosphere. The temperature was ramped to either 500 ºC or 900 ºC for 15 minutes and held for 30 minutes to form two batches of thermally reduced graphene oxide (trGO). The trGO was re-suspended in DMF (5 mg/mL), but the trGO reduced at 900ºC is insoluble in the given DMF concentration. The chemical reduction of GO was facilitated through citrate reduction. Sodium citrate (688 mg) was added to 200 mL of GO (0.267 mg/mL), mixed at 95 ºC with a reflux condenser. The reaction lasted for 6 hours or 24 hours to produce two separate sets of reduced graphene oxide: crGO-6 and crGO24, respectively. After cooling down to room temperature, the crGO solution was purified in several rounds of dialysis to remove residual salts. The purified solution was oven-dried at 60 ºC and resuspended in DMF (5 mg/ML) with sonication to aid the dissolution.

Electrospinning solution preparation. The stock solution of the doped PANi solution was created from equimolar amounts of PANi (400 mg) and HCSA (520 mg) dispersed in chloroform (30 mL), mixed for 12 hours at room temperature, and then sonicated for 20 mins. The resulting HCSA-PANi solution is a dark green dispersion and is filtered through a 0.45 μm PTFE syringe filter to remove large undispersed PANi particles. Electrospinning solutions were prepared by combining HCSA-PANi dispersion (750 μL) with chloroform (150 μL), PEO (7mg), and DMF (100μL) or graphene oxide solution

(GO, trGO, crGO-6, or crGO-24) (100uL). The mixtures were stirred for 2 hours at room temperature, yielding a slightly viscous solution. In total, five different sets of electrospinning solutions were prepared: PANi, PANi/GO, PANi/trGO, PANi/crGO-6, and PANi/crGO-24.

Electrospun nanofiber sensor fabrication. Electrospun nanofibers were fabricated in a home-built device[22] and were collected directly onto interdigitated microelectrodes (IMEs). IMEs consisted of 8 x 8 mm silicon substrates with a SiO2 passivation layer, a 10 nm Ti adhesion layer, and a 200 nm Au conductive layer. The interdigitated fingers consisted of 30 µm lines and 30 µm gaps (73 lines total). Electrospinning solutions were loaded into a glass syringe equipped with a 20 ga blunt-tip dispensing needle mounted on a syringe pump set at 1.25 mL/hr. and electrospun using a high voltage power supply at 10–15 kV. IMEs were attached to a rotating aluminum disc collector (8cm diameter, 5mm width) placed at a set distance of 14 cm from the syringe needle tip.

Drop-cast film sensor fabrication. Thin-film sensors were fabricated by depositing 10 µL of the electrospinning solution directly onto an IME and allowed to dry at ambient conditions.

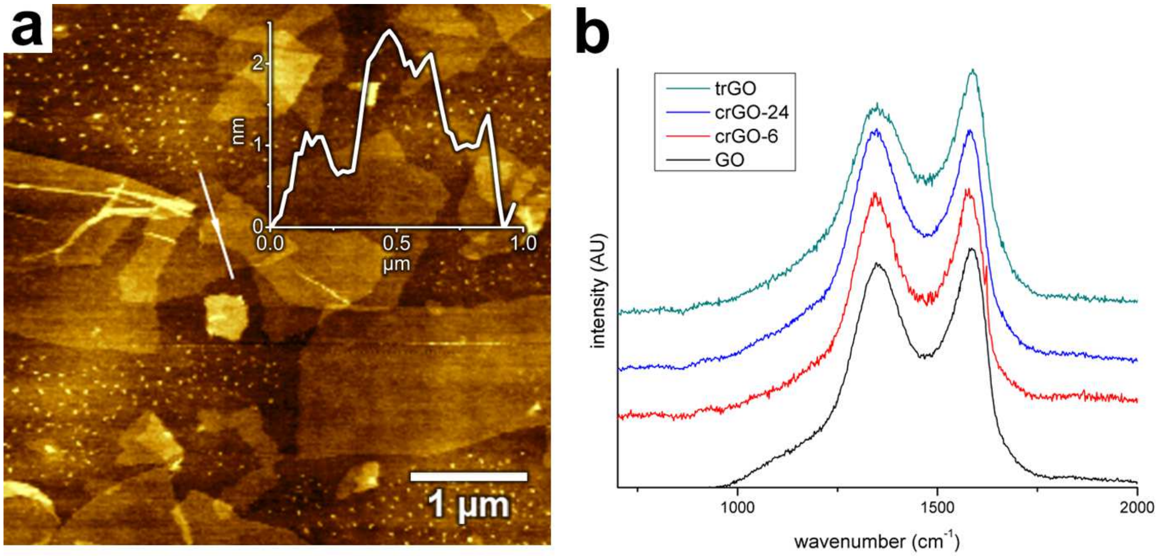

Figure 2.1. (A) AFM image of rGO, **(B)** Raman spectra of rGO variants.

Characterization. The graphene variants GO, trGO, crGO-6, and crGO-24 were characterized using Raman spectroscopy (**Figure 2.1B**) on an SPM with confocal Raman using a 532 nm laser source. Graphene oxide was further characterized using atomic force microscopy (AFM) (**Figure 2.1A**) in tapping mode. The electrospun nanofibers and drop cast thin film was characterized using scanning electron microscopy (SEM) (**Figure 2.2**).

Alcohol vapor detection. Gas sensing tests were performed in a home-built system using a sealed glass chamber with electrode leads running into the chamber. A baseline resistance was acquired at ambient laboratory conditions (24 ºC, 42% RH). Exposure to analyte vapor was accomplished by injecting known volumes of the volatile liquids (methanol, ethanol, or 1-propanol) through a septum housed in the chamber lid. A small electric fan placed inside the chamber accelerated analyte diffusion. Analyte concentrations were determined by applying the ideal gas law. An electrometer sourced

0.1 V to the sensor, and the current was monitored in real-time by a custom LabView program. The measured current was converted to resistance using Ohm's Law. Principal component analysis (PCA) was performed on the data set using R software (version 3.0.1 Mac OS, The R Foundation, Vienna, Austria, www.r-project.org).

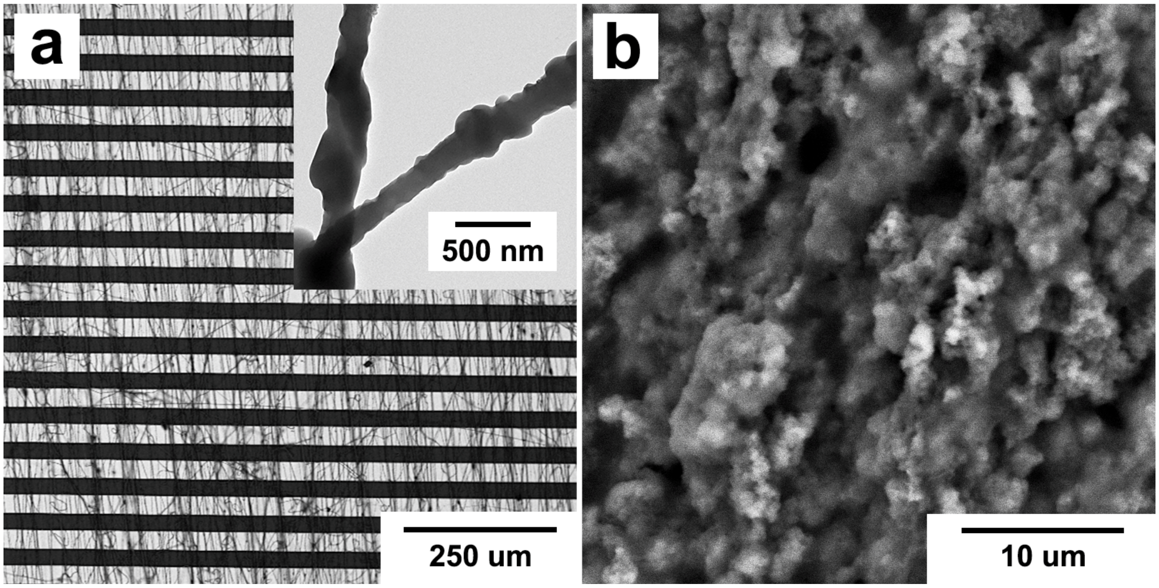

Figure 2.2 (A) SEM image of typical PANi/PEO/GO composite nanofibers (TEM inset) collected on interdigitated microelectrode and **(B)** SEM image of PANi/PEO/GO drop-cast film.

2.3 Results and Discussion.

Graphene oxide and reduced graphene oxide variants. Graphene oxides (GO) and four sets of reduced graphene oxides (rGO) were successfully synthesized. Thermal reduction of graphene oxide (trGO) produced two variants based on the temperature set for the reduction: 500 ºC (trGO-500) and at 900 ºC (trGO-900). Because the trGO-900 was insoluble in DMF at 5mg/mL, this trGO variant was not used. The designation of trGO-500 is simplified to trGO in the rest of this chapter. Citrate reduction of graphene oxide (crGO) was conducted for 6 hours (crGO06) or 24 hours (crGO-24). Each of these GO and rGO variants were then dissolved in DMF to create 5mg/mL stocks of GO, trGO, crGO-6, and crGO-24.

The reduction of the GO species was characterized by Raman spectroscopy (Figure 2.1 B). The Raman spectra confirm the structural differences between the rGOs as the reduction occurred. The GO spectrum displays the characteristic D and G peaks at 1351 cm-1 and 1591 cm-1, respectively. The change in this D/G intensity ratio of the crGO-6 (0.98) and the crGO-24 (1.01) compared to that of GO (0.95) is consistent with reduced graphene oxide. According to literature, this is due to an increase in the total number of sp2 domains accompanied by a decrease in their average size[22,24]. Furthermore, crGO-24 exhibits a higher D/G ratio than its crGO-6 counterpart suggesting that reduction has proceeded further as the reaction time increased. The Raman spectra of trGO exhibit a decrease of the D/G band ratio from GO (0.95) to trGO (0.88), which is consistent with partial restoration of graphite lattice reported in the literature[25,26]. These are four variants of GO and rGO that affect the sensor performance towards detecting alcohol vapor can be mixed into the electrospinning solution to form four distinct sets of sensors using either electrospun composite nanofibers or their drop cast thin-film counterparts.

Nanofiber sensor fabrication. The electrospinning of the PANi/HCSA/PEO/rGO solution produces 5 sets of composite nanofibers: 1) No GO, 2) GO, 3) trGO, 4) crGO-6, and 5) crGO-24. These composite nanofibers were collected on an interdigitated microelectrodes (IMEs) attached to a grounded rotating aluminum disc collector. The rotation of the disc controls the deposition of parallel nanofibers to be perpendicular to the orientation of gold fingers on the IMEs (Figure 2.2A). The roughness depicted in the SEM image along with alternating dark and light areas within the nanofibers suggests the overlapping of PANi and GOs in the composite. The nanofibers were characterized by SEM imaging to show that the fibers had average diameters of 800nm, providing high surface area ratios that are fundamental for quick interaction with analyte vapors.

Drop cast thin film sensor fabrication. Deposition of 10µL of the PANi/HCSA/PEO/rGO solution used in electrospinning onto the IMES produces five sets of composite thin films: 1) No GO, 2) GO, 3) trGO, 4) crGO-6, and 5) crGO-24. While the thickness of the film could be an issue, we attempted to spin-coat the IMEs with the electrospinning solutions. But the high speed ended up removing most of the PANi from the film, which renders the film non-conductive. Although PEO is used as a carrier polymer for electrospinning, it is not required for thin films and would perform better without it. The PEO concentrations were maintained in the thin film fabrication to make a 1:1 comparison of the nanofiber and thin-film sensors. Characterization by SEM shows that the surface morphology is very rough, providing more surface area for analyte interaction compared to a flat film.

Conductivity of composite nanofiber and drop cast thin film sensors. The typical current-voltage (IV) curves for nanofiber and thin-film sensors (**Figure 2.3**) synthesized from the PANi/PEO/crGO-6 solution was obtained by sweeping the source voltage from -0.2 to 0.2 V. Both substrate response curves are linear and is consistent with ohmic contacts between the PANi composite and gold electrodes for the voltage sourced (0.1 V) for all gas sensing experiments. Notably, the thin film sensors exhibited higher conductivity than their nanofiber counterparts. This is due to the increased contact area of the film with the electrode surface, as well as higher mass loading of the PANi compared to composite Nanofiber. Additionally, PEO, an insulating polymer, acts as a host for the formation of uniform films and fibers. Thus, the HCSA-doped PANi and GO variants are responsible for the electrical conductivity of the composite sensor material.

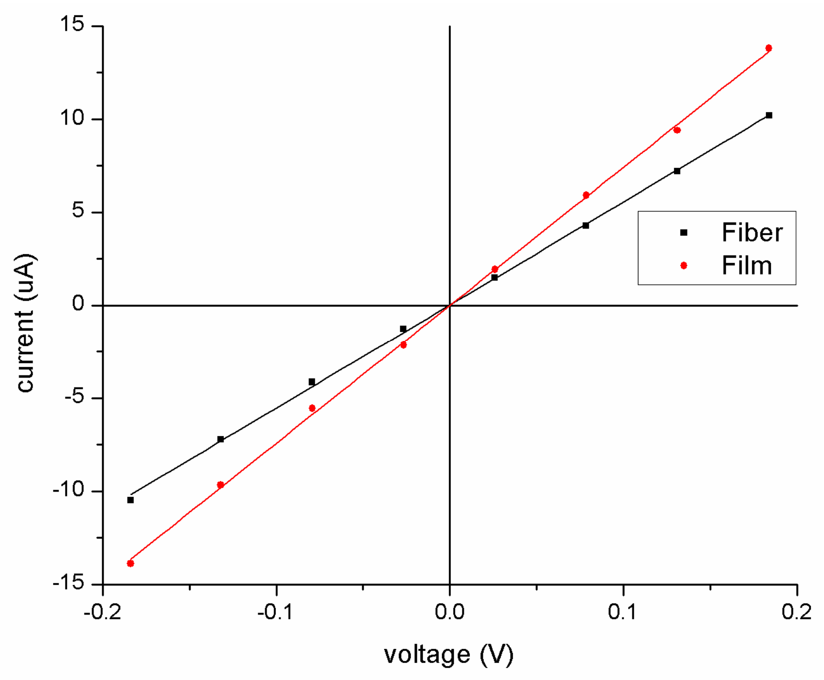

Figure 2.3. IV curves of typical PANi/PEO/GO composite gas sensors.

Nanofiber and thin film sensor arrays. Five sets of electrospun nanofiber and five sets of drop-cast thin-film sensors were prepared from PANi/HCSA/PEO and varying graphene material. The four sensing surface composed of 1) GO, 2) trGO, 3) crGO-6, and 3) crGO-24, while a nanofiber with no GO was used as a control. Thus, a total of 10 different sensor surfaces were fabricated and assembled for an array-based sensor system.

Detection of aliphatic alcohol vapors. The performances of the electrospun nanofiber (**Figure 2.4**) and drop cast thin film (**Figure 2.5**) surfaces were evaluated as room temperature chemiresistor sensors for pure samples of methanol, ethanol, and 1-propanol vapors at 50, 200, 350, 500, and 650 ppm. Sensor responses were evaluated using $\Delta R/R_0$, where R_0 is baseline resistance and ΔR changes in resistance upon exposure to analyte vapor.

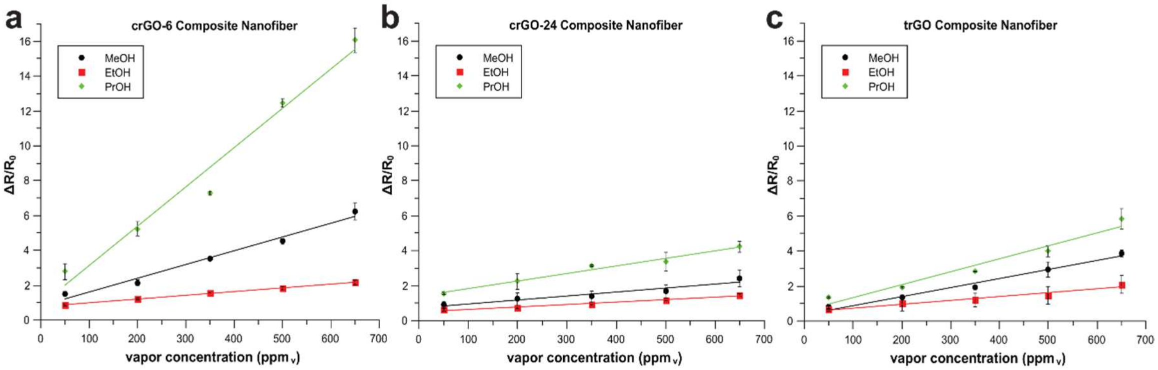

Figure 2.4. Changes in resistance of electrospun nanofiber PANi-based composite drop-cast films doped with different variants of rGO: (**A**) GO, (**B**) crGO-6, (**C**) crGO-24, and (**D**) trGO, upon exposure to different aliphatic alcohols.

Electrospun nanofiber performance. The various rGOs nanofiber variants were examined as a room temperature gas sensor, and the results were compiled into calibration curves (Figure 2.4). As expected, the nanofiber control with no GO was not conductive and did not exhibit any changes in electrical resistance upon exposure to alcohol vapors at the tested concentrations. The GO-doped composite nanofibers were also non-conductive and there were no observable changes in electrical resistance. Given that PEO and GO are innately insulators, these results were not completely unexpected.

The remaining three rGO variants: trGO, crGO-6, and crGO-24, exhibited an increase in electrical resistance in response to alcohol vapors. These nanofibers exhibit strong linear correlations (0.92-1), Among these three nanofiber composites, the crGO-6 doped nanofiber exhibited the largest increase in resistance upon exposure to aliphatic alcohols. The sensor responses and response time were recorded (Figure 2.6A). The crGO-24 nanofibers display the highest sensitivity towards methanol (2.3 ppm), ethanol (1.4 ppm), and propanol (4.3 ppm). Notably, the sensing response toward different aliphatic alcohol vapors is in the order: 1-propanol (PrOH) > methanol (MeOH) > ethanol (EtOH).

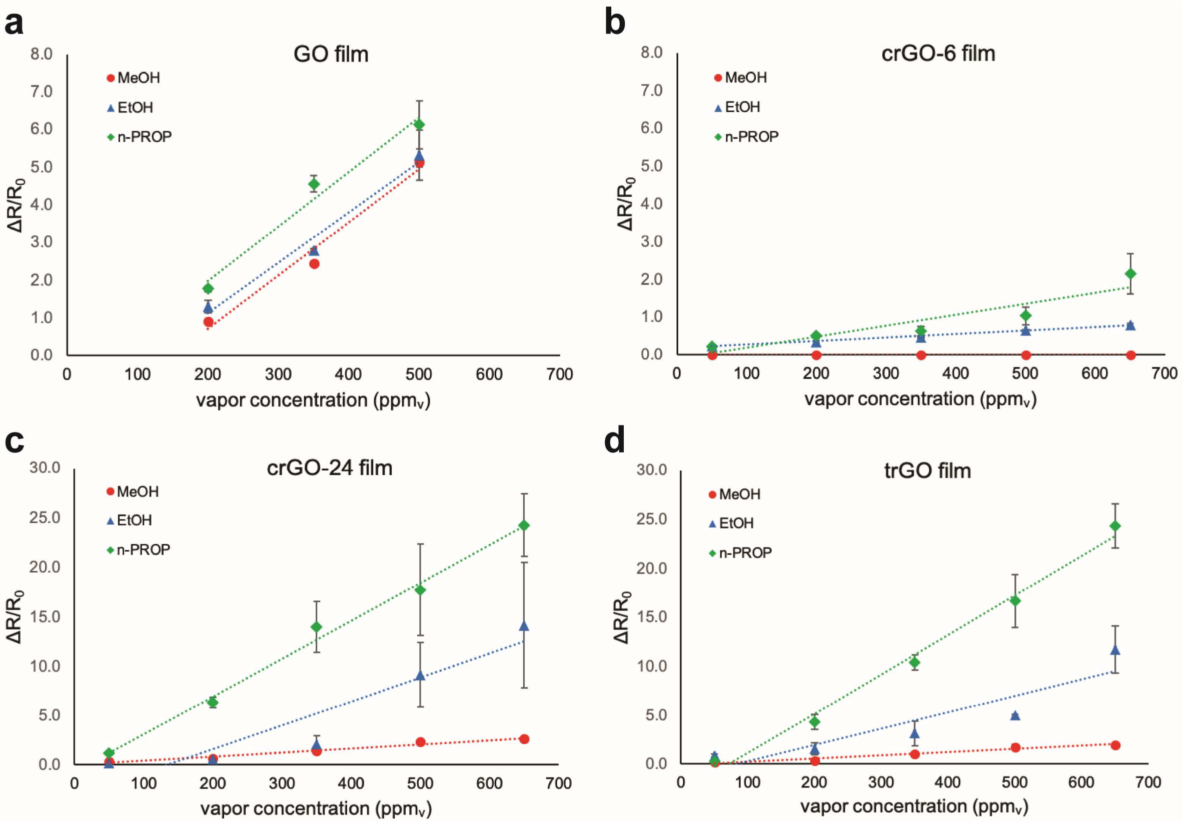

Figure 2.5. Changes in resistance of electrospun PANi-based composite drop-cast films doped with different variants of rGO: **(A)** GO, **(B)** crGO-6, **(C)** crGO-24, and **(D)** trGO, upon exposure to different aliphatic alcohols.

Drop cast thin film sensor performance. The various rGOs thin-film variants were examined as a room temperature gas sensor, and the results were compiled into calibration curves (Figure 2.5). Similarly, the drop cast thin film control with no GO is also nonconductive and exhibited no changes to electrical resistance upon exposure to the aliphatic alcohol vapors. Unlike the nanofiber surface, the GO doped thin film sensor was conductive due to higher surface contact to the electrode and the mass loading of PANi onto the sensor surface compared to the electrospun nanofiber. These nanofibers exhibit strong linear correlations (0.83-1). The sensor surface with trGO, crGO-6, and crGO-24, also exhibited an increase in electrical resistance in response to alcohol vapors. Among these three thin film surfaces, the trGO doped nanofiber exhibited the largest increase in resistance upon exposure to aliphatic alcohols. The sensor response and response time was recorded (Figure 2.6B). The crGO-6 thin-film displays the highest sensitivity towards ethanol (1.4 ppm), propanol (4.3 ppm), while non-responsive to methanol. The trGO thin film is sensitive to methanol (3.3 ppm). The response pattern for the drop cast thin film toward different aliphatic alcohol vapors is in the order: 1-propanol (PrOH) > ethanol (EtOH) > methanol (MeOH).

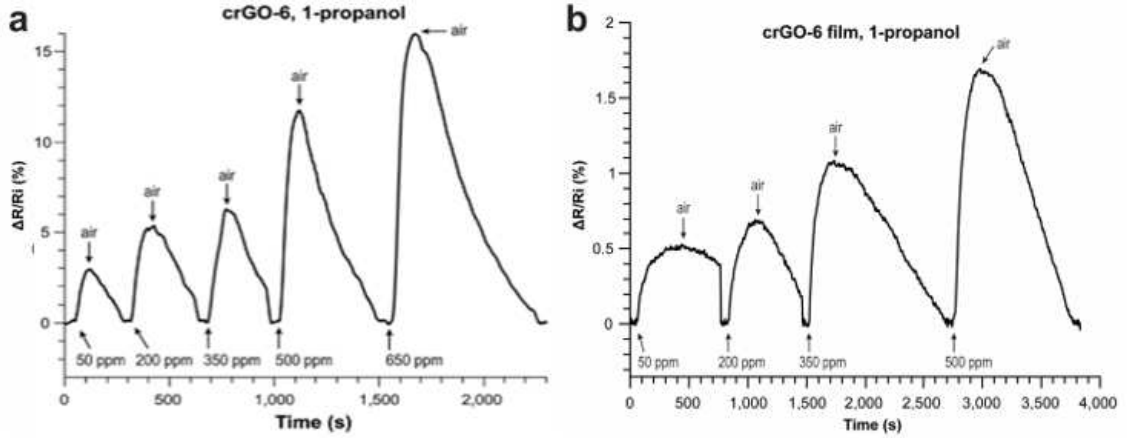

Figure 2.6. Example time response of PANi-based composite **(A)** nanofiber sensor and **(B)** drop-cast film sensor doped with partially reduced graphene oxide.

Detection of Aliphatic Alcohol Vapors. The detection of the pure analytes is accomplished by measuring changes in the electrical conductivity of the various sensor surfaces. The response trend from the nanofiber and thin-film sensor differs due to how the analytes interact with the sensor surfaces. There are three main mechanisms by which an analyte could influence the conductivity of the surfaces, described individually below.

The first mechanism of action is the swelling of the host polymer matrix caused by the analyte adsorbing onto the sensor surfaces. As the molecules of the analyte are adsorbed onto the sensor surface, the polymer matrix will swell. This swelling increases the distances between neighboring PANi chains, widening the gaps that the electron must transverse[27]. This effect is more pronounced as the adsorbed molecule increases in size. Considering the given analytes, this mechanism would suggest that the sensor would be most responsive to 1-propanol, ethanol, and methanol in decreasing order.

The second mechanism focuses on the ion-dipole interaction of the alcohol molecules with the imine nitrogen groups of the PANi. This interaction causes the PANi backbone to shift into a more linter conformation, correlating to a decrease in electrical resistance as the path for electron travel becomes shorter[6,28,29]. Therefore, the polarity of the analytes is key to the mechanism, suggesting that the stronger the polarity the stronger the confirmation shifts. Given alcohol analytes and their polarity: methanol (0.762), ethanol (0.654), and 1-propanol (0.617), this mechanism predicts that the sensor would be most responsive towards methanol, ethanol, and 1-propanol in decreasing order.

The third mechanism centers around the hydrogen bonding between the aliphatic alcohols to the oxygen-containing functional groups of the rGOs. This interaction leads to a larger distance between the PANi/rGO and or the rGO/rGO interfaces that the electrons travel through, causing an increase in electrical resistance[30,31]. Alcohols with stronger polarity will react more strongly with the rGOs. Smaller alcohols are better able to penetrate the polymer matrix. Thusly, the predicted response trend for this mechanism suggests that the sensor would be most sensitive to methanol, ethanol, and 1-propanol in decreasing order.

The drop cast thin film response pattern of 1-propanol > ethanol > methanol, best matches the first mechanism: polymer matrix swelling. Due to the sheer volume used to fabricate the film, the drop cast thin film has a higher total surface area allowing for more surface adsorption of the gas analytes. Because of the high total surface area, the signal contribution from the first mechanism outweighs the other two mechanisms.

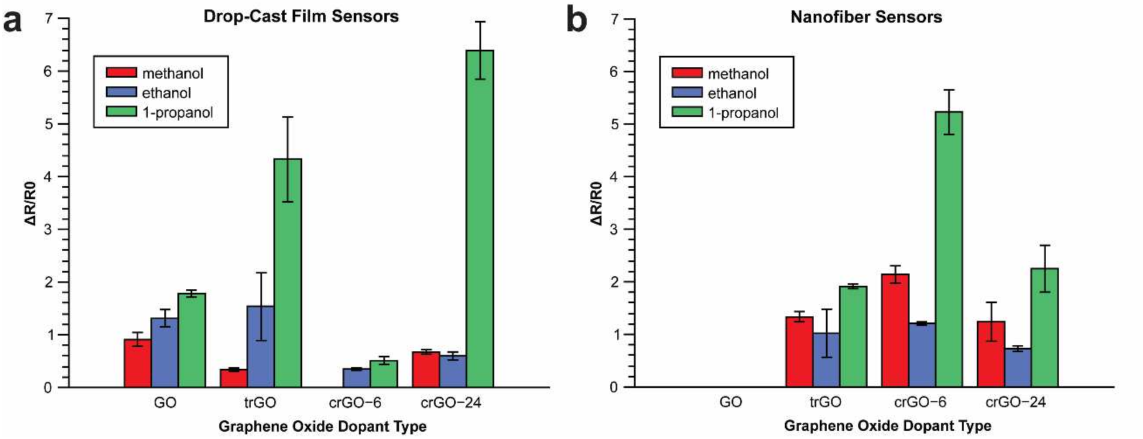

Figure 2.7. Comparison of the response of **(A**) drop-cast film and **(B)** electrospun nanofiber sensors to 200 ppm of methanol, ethanol, or 1-propanol.

The nanofiber response pattern does not directly match a single mechanism. Just like the thin films, the swelling of the nanofiber matrix caused by the surface adsorption of analyte plays a significant role as the sensor was most responsive towards 1-propanol. But the nanofiber sensor was more responsive to methanol than ethanol, suggests that there are some contributions from the second and third mechanisms of ion-dipole and hydrogen bonding influencing the change in electrical resistance exhibited by the sensor. Thus, the response pattern of 1-propanol > methanol > ethanol suggests that the primary mechanism is the swelling of the nanofiber matrix caused by analyte adsorption while ion-dipole and hydrogen-bonding interactions cause the flip in signal response from methanol and ethanol.

Table 2.1 Compiled sensor component responses at room temperature and 42% relative humidity.

Dopant	Analyte	Sensitivity (x10^{-3}, ppm_v^{-1})		Correlation (r^2)		200 ppm Response (min)		200 ppm Recovery (min)	
		Fiber	Film	Fiber	Film	Fiber	Film	Fiber	Film
GO	methanol	-	14	-	0.98	-	1.6	-	3.4
	ethanol	-	13	-	0.98	-	2.7	-	3.6
	1-propanol	-	15	-	0.97	-	3.9	-	8.3
crGO-6	methanol	7.9	-	0.98	-	0.4	-	1.4	-
	ethanol	2.1	0.9	1.0	0.99	0.5	2.2	4.2	7.4
	1-propanol	23	2.9	0.97	0.85	1.0	5.1	4.1	10.3
crGO-24	methanol	2.3	4.2	0.92	0.97	0.7	2.2	1.9	2.8
	ethanol	1.4	24	0.97	0.88	0.8	3.5	1.4	2.5
	1-propanol	4.3	38	0.98	0.99	1.4	7.1	3.0	9.2
trGO	methanol	5.2	3.3	0.98	0.96	0.5	1.7	1.9	2.6
	ethanol	2.0	17	0.95	0.83	0.6	2.6	4.4	7.5
	1-propanol	7.4	40	0.96	0.99	3.2	8.7	6.7	10.1

Sensor Component Comparison. The electrospun nanofiber and drop cast thin-film sensor responses were compiled (**Figure 2.7**) for comparison of the induvial component's sensitivity, linear correlation, response time, and recovery time (**Table 2.1**). Because nanofiber possesses a high surface area to volume ratio, the sensor observes higher signal response for individual analytes interacting with the surface and will have lower limits of detection than their thin-film counterparts. Due to the bulk of the thin film, the thin film has a higher total surface area in contact with the electrode, thus observes higher signals at a given concentration. But the thin-film sensor observes larger fluctuation in signal response, lowering the sensor precision compared to the nanofiber counterpart. This is supported as the nanofiber components have stronger linear correlations and more concise error bars than the thin film counterpart. The nanofiber sensor has a faster response and recovery time compared to the thin film counterparts, due to less surface area for the analytes to saturate and de-adsorb from. While one component may excel over the other in certain aspects, both the nanofiber and thin-film sensor components are capable of sensitive detection of the gas analytes.

Principal component analysis (PCA). While both the thin film and nanofiber sensor components are sensitive towards analyte detection and provide quantification. The sensor is unable to selectively identify the analyte present. Principal component analysis, a statistical analytic technique, is used to interrogate the given data and compiled a chart that aids in identifying the analyte based on the pattern response of all the components and rGO variants. Variability in $\Delta R/R0$ response among the 3 PANi-based drop-cast film sensor components doped with different reduced GO variants (trGO, crGO-6, or crGO-24) was analyzed to distinguish a sample of a single pure aliphatic alcohol. The sensor array provided a large data set with many variables (3 analytes x 5 concentrations x 3 sensors x triplicate analysis = 135 data points). PCA (Figure 2.8) was performed on the data obtained from the film-based sensor array, resulting in 12 principal components (PCs). A significant amount of variance in the data was captured by PC1 (77.8%) and PC2 (16.6%) for a total of 94.4%. By applying Horn's parallel analysis to the PCA data, it was revealed that only the first PC need be retained. For clarity of presentation, a 2D PCA plot was generated (Figure 7) which shows 3 separate clusters, confirming that the sensor array successfully classified the 3 short-chain aliphatic alcohols: methanol, ethanol, and 1-propanol. The error ellipses (95% CI) indicate good reproducibility of the sensor array. PCA with the same parameters was also performed on the data from the 3 PANi-based nanofiber sensor components doped with different reduced GO variants (trGO, crGO-6, or crGO-24). This allows the sensor to further distinguish different aliphatic alcohols. The results highlight the ability of both the drop-cast film and nanofiber-based sensor arrays to successfully classify alcohol vapors at ppm concentrations from a sample containing only one analyte. Like many sensors, this faces difficulty in identifying analytes in a mixed sample and will require separation to correctly identify the analytes within the mixture.

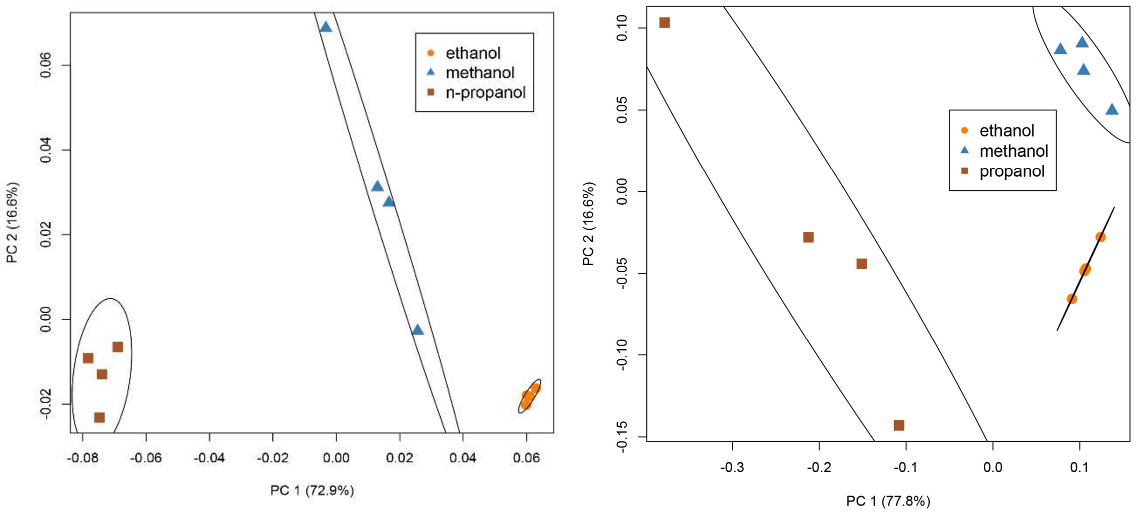

Figure 2.8. PCA plot demonstrating the classification of aliphatic alcohols by a PANi/HCSA/PEO **(A)** Left. nanofiber drop-cast and **(B)** Right. film sensor array doped with three different rGO variants.

2.4 Conclusion.

In this study, PANi composite nanofiber and drop-cast film sensors doped with rGO variants were fabricated and tested as room temperature alcohol sensors. All three sensors rGO variants (trGO, crGO-6, and crGO-24) exhibited strong linear responses to aliphatic alcohol vapors, strong responses, quick recovery times and PPM level of sensitivity. The crGO-6 provided the best balance between electrical conductivity and functional group for analyte interaction for the tunability of the electrospun nanofiber sensor. The trGO provided similar property and function for the drop cast thin-film sensor. The combination of multiple PANi/PEO sensor components doped with rGO (trGO, crGO-6, or crGO24) formed a sensor array capable of identifying methanol, ethanol, and 1-propanol using principal component analysis (PCA). After identification, the signal response can be matched to an appropriate calibration curve to quantify the pure analyte present. In the future, the sensor components can be assembled into a singular field-ready device. These portable gas sensors can be used in households or industries to monitor air samples for alcohol and other VOCs that are PANi or rGO sensitive gases such as NO2, NH3, and CO.

References:

(1) Calderilla, C.; Maya, F.; Cerdà, V.; Leal, L. O. 3D Printed Device Including Disk-Based Solid-Phase Extraction for the Automated Speciation of Iron Using the Multisyringe Flow Injection Analysis Technique. *Talanta* **2017**, *175* (April), 463–469.

(2) Aliheidari, N.; Aliahmad, N.; Agarwal, M.; Dalir, H. Electrospun Nanofibers for Label-Free Sensor Applications. *Sensors (Switzerland)* **2019**, *19* (16).

(3) Lu, Z.; Zhou, Q.; Wei, Z.; Xu, L.; Peng, S.; Zeng, W. Synthesis of Hollow Nanofibers and Application on Detecting SF6 Decomposing Products. *Front. Mater.* **2019**, *6* (July), 1–7.

(4) Rozemarie, M. L.; Andrei, B.; Liliana, H.; Cramariuc, R.; Cramariuc, O. Electrospun Based Polyaniline Sensors - A Review. *IOP Conf. Ser. Mater. Sci. Eng.* **2017**, *209* (1).

(5) Abd Razak, S. I.; Wahab, I. F.; Fadil, F.; Dahli, F. N.; Md Khudzari, A. Z.; Adeli, H. A Review of Electrospun Conductive Polyaniline Based Nanofiber Composites and Blends: Processing Features, Applications, and Future Directions. *Adv. Mater. Sci. Eng.* **2015**, 1–19.

(6) Virji, S.; Huang, J.; Kaner, R. B.; Weiller, B. H. Polyaniline Nanofiber Gas Sensors: Examination of Response Mechanisms. *Nano Lett.* **2004**, *4* (3), 491–496.

(7) Pandey, S. Highly Sensitive and Selective Chemiresistor Gas/Vapor Sensors Based on Polyaniline Nanocomposite: A Comprehensive Review. *J. Sci. Adv. Mater. Devices* **2016**, *1* (4), 431–453.

(8) Arsat, R.; Yu, X. F.; Li, Y. X.; Wlodarski, W.; Kalantar-zadeh, K. Hydrogen Gas Sensor Based on Highly Ordered Polyaniline Nanofibers. *Sensors Actuators, B Chem.* **2009**, *137* (2), 529–532.

(9) Ji, S.; Li, Y.; Yang, M. Gas Sensing Properties of a Composite Composed of Electrospun Poly(Methyl Methacrylate) Nanofibers and in Situ Polymerized Polyaniline. *Sensors Actuators, B Chem.* **2008**, *133* (2), 644–649.

(10) Ding, B.; Wang, M.; Yu, J.; Sun, G. Gas Sensors Based on Electrospun Nanofibers. *Sensors* **2009**, *9* (3), 1609–1624.

(11) Talwar, V.; Singh, O.; Singh, R. C. ZnO Assisted Polyaniline Nanofibers and Its Application as Ammonia Gas Sensor. *Sensors Actuators, B Chem.* **2014**, *191*, 276–282.

(12) Qavamnia, S. S.; Nasouri, K. Conductive Polyacrylonitrile/Polyaniline Nanofibers Prepared by Electrospinning Process. *Polym. Sci. - Ser. A* **2015**, *57* (3), 343–349.

(13) Zhou, Y.; Freitag, M.; Hone, J.; Staii, C.; Johnson, A. T.; Pinto, N. J.; MacDiarmid, A. G. Fabrication and Electrical Characterization of Polyaniline-Based Nanofibers with Diameter below 30 Nm. *Appl. Phys. Lett.* **2003**, *83* (18), 3800–3802.

(14) Aussawasathien, D.; Dong, J. H.; Dai, L. Electrospun Polymer Nanofiber Sensors. *Synth. Met.* **2005**, *154* (1–3), 37–40.

(15) Pinto, N. J.; Johnson, A. T.; MacDiarmid, A. G.; Mueller, C. H.; Theofylaktos, N.; Robinson, D. C.; Miranda, F. A. Electrospun Polyaniline/Polyethylene Oxide Nanofiber Field-Effect Transistor. *Appl. Phys. Lett.* **2003**, *83* (20), 4244–4246.

(16) Li, C.; Chartuprayoon, N.; Bosze, W.; Low, K.; Lee, K. H.; Nam, J.; Myung, N. V. Electrospun Polyaniline/Poly(Ethylene Oxide) Composite Nanofibers Based Gas Sensor. *Electroanalysis* **2014**, *26* (4), 711–722.

(17) Huang, J.; Virji, S.; Weiller, B. H.; Kaner, R. B. Polyaniline Nanofibers: Facile Synthesis and Chemical Sensors. *J. Am. Chem. Soc.* **2003**, *125* (2), 314–315.

(18) Zhang, K.; Zhang, L. L.; Zhao, X. S.; Wu, J. Graphene/Polyaniline Nanofiber Composites as Supercapacitor Electrodes. *Chem. Mater.* **2010**, *22* (4), 1392–1401.

(19) Huang, X.; Hu, N.; Gao, R.; Yu, Y.; Wang, Y.; Yang, Z.; Siu-Wai Kong, E.; Wei, H.; Zhang, Y. Reduced Graphene Oxide-Polyaniline Hybrid: Preparation, Characterization and Its Applications for Ammonia Gas Sensing. *J. Mater. Chem.* **2012**, *22* (42), 22488–22495.

(20) Moayeri, A.; Ajji, A. Fabrication of Polyaniline/Poly(Ethylene Oxide)/Non-Covalently Functionalized Graphene Nanofibers via Electrospinning. *Synth. Met.* **2015**, *200*, 7–15.

(21) Wang, L.; Lu, X.; Lei, S.; Song, Y. Graphene-Based Polyaniline Nanocomposites: Preparation, Properties and Applications. *J. Mater. Chem. A* **2014**, *2* (13), 4491–4509.

(22) Burris, A. J.; Tran, K.; Cheng, Q. Tunable Enhancement of a Graphene/Polyaniline/Poly(Ethylene Oxide) Composite Electrospun Nanofiber Gas Sensor. *J. Anal. Test.* **2017**, *1* (2), 12.

(23) Zaaba, N. I.; Foo, K. L.; Hashim, U.; Tan, S. J.; Liu, W. W.; Voon, C. H. Synthesis of Graphene Oxide Using Modified Hummers Method: Solvent Influence. *Procedia Eng.* **2017**, *184*, 469–477.

(24) Ramesha, G. K.; Sampath, N. S. Electrochemical Reduction of Oriented Graphene Oxide Films: An in Situ Raman Spectroelectrochemical Study. *J. Phys. Chem. C* **2009**, *113* (19), 7985–7989.

(25) Yang, H.; Hu, H.; Ni, Z.; Poh, C. K.; Cong, C.; Lin, J.; Yu, T. Comparison of Surface-Enhanced Raman Scattering on Graphene Oxide, Reduced Graphene Oxide and Graphene Surfaces. *Carbon N. Y.* **2013**, *62*, 422–429.

(26) Kaniyoor, A.; Ramaprabhu, S. A Raman Spectroscopic Investigation of Graphite Oxide Derived Graphene. *AIP Adv.* **2012**, *2* (3).

(27) Low, K.; Horner, C. B.; Li, C.; Ico, G.; Bosze, W.; Myung, N. V.; Nam, J. Composition-Dependent Sensing Mechanism of Electrospun Conductive Polymer Composite Nanofibers. *Sensors Actuators, B Chem.* **2015**, *207* (Part A), 235–242.

(28) Pirsa, S. Chemiresistive Gas Sensors Based on Conducting Polymers. *Mater. Sci. Eng. Concepts, Methodol. Tools, Appl.* **2017**, *1–3*, 543–574.

(29) Liu, S. S.; Bian, L. J.; Luan, F.; Sun, M. T.; Liu, X. X. Theoretical Study on Polyaniline Gas Sensors: Examinations of Response Mechanism for Alcohol. *Synth. Met.* **2012**, *162* (9–10), 862–867.

(30) MacAgnano, A.; Zampetti, E.; Pantalei, S.; De Cesare, F.; Bearzotti, A.; Persaud, K. C. Nanofibrous PANI-Based Conductive Polymers for Trace Gas Analysis. *Thin Solid Films* **2011**, *520* (3), 978–985.

(31) Athawale, A. A.; Kulkarni, M. V. Polyaniline and Its Substituted Derivatives as Sensor for Aliphatic Alcohols. *Sensors Actuators, B Chem.* **2000**, *67* (1), 173–177.

Chapter 3: Silver-EDTA Nanoparticle Decorated PVA Nanofibers for Reversible Capture and Quantification of Proteins

3.1 Introduction.

The detection of harmful compounds is important in protecting and maintaining both human and environmental health. While volatile organic compounds in the gaseous state were the focus in the earlier chapter, there are other physical states of these potential analytes. This chapter focuses on applying nanofibers in biosensors for the detection of protein analytes in aqueous samples. This requires the implementation of new strategies to fabricate a nanofiber sensor capable of detecting and quantifying protein in liquid samples.

Electrospun Polyvinyl alcohol (PVA) is a water-soluble hydrophobic polymer that has been studied for various applications. For example, biological studies have employed PVA nanofibers in cell-based studies for cytotoxicity[1–3], drug delivery[4–7], and scaffolds for cell growth and proliferation [8–11]. Electrospun PVA nanofibers have also been examined as electrodes in batteries[12–16], and employed in conjunction with mass spectrometry as a platform for ionizing molecules with minute surface functionalization[17,18]. Additionally, many studies incorporate various elements to enhance the detection of molecules, such as carbon nanotubes (CNT)[19–22], fluorescent probes[23–29], and nanoparticles[30–34].

While applications of PVA are limited due to dissolution, chemical cross-linking by glutaraldehyde (GA) can improve stability in aqueous media. This mechanism of the cross-linking reaction has been well studied and reveals the hydroxyl group of the PVA reacts with the aldehyde group of GA in the presence of a strong acid. These cross-linked nanofiber mats have been utilized in membrane and filtration applications because the fibers are rendered insoluble in most solvents[35–39]. These properties are also beneficial as a substrate for biosensor surfaces.

Cross-linked PVA nanofiber has potential as a biosensor surface, but due to lack of both the biorecognition and signal transducer elements, additional modifications are required to employ this as a functioning biosensor. Nanoparticles have been incorporated into nanofiber as either the biorecognition or signal transducer elements. Nanoparticles have been used in electrochemical or chemoresistance based nanofiber sensors as they can improve signal sensitivity by increasing conductivity of the nanofibers or by coupling with fluorescent probes. They have also shown to improve selectivity by supplying areas of biorecognition in these nanofiber biosensors. Silver nanoparticles (AgNPs) are stable, non-toxic, and has great biocompatibility that have been implemented into biosensor as either part of the biological recognition element[40,41] or to enhance the signal transducer element[42,43]. This project utilizes AgNPs capped by ethylenediaminetetraacetic acid (EDTA) as the biological recognition element of the biosensor.

The biorecognition element employed in this biosensor leverages the ability of EDTA-functionalized AgNPs to chelate metal ion. Metal ion chelation (binding) is an area of interest for the development of sensors for two different purposes. Firstly, metal ion chelation is an important interaction for heavy metal ion in water for the health safety of potable water and water waste treatment and management. Surfaces that can effectively and cleanly remove metal ions in aqueous media is highly sought after to improve current water waste treatment methods and processes. Secondly, metal ion chelation plays a significant role in biological studies. One major application is purifying recombinant proteins functionalized with polyhistidine tag (His-tag). Nitriloacetic Acid (NTA) has been used in Nickel affinity purification columns and resin to facilitate the purification of His-tag proteins. These His-tag proteins are important in biological experiments involving genetic modification to study genetic diseases. Metal ion chelation is vital for metalloproteins, a family of protein that binds metal ions. These metalloproteins are important in the biological systems as they serve diverse functions, from oxygen transport of the hemoglobin to protein transcription and iron-responsive element-binding protein (IRE-BP) aids in regulation mRNA transcription.[44] Developing biorecognition elements for these proteins can provide new avenues in studies related diseases.

This biosensor employed silver nanoparticles as the signal transducer using an optical detector to monitor shifts in localized surface plasmon resonance (LPSR)[45–49]. LSPR is a phenomenon occurring in structures that are much smaller than the wavelength of incoming light. This causes the electrons on these nanostructures to oscillate, generating an evanescent field surrounding the nanostructure[50]. Various interactions with the surface of these structures will alter the peak absorption wavelength of the nanoparticles. LSPR analysis of nanofiber-nanoparticles interface has shown that these substrates are sensitive to changes in refractive indexes.[51] In our initial study, we were able to demonstrate that PVA nanofibers decorated with EDTA-AgNP's do exhibit this LSPR property of high sensitivity to changes in the bulk refractive indexes. Unfortunately, our preliminary results from metal ion binding demonstrated that the surface is not sensitive to small analytes.

Further examination also showed that the sensor surface was not responsive to protein binding. While the literature has demonstrated LSPR can detect protein binding, due to the current arrangement of adsorbing the nanoparticle on the nanofiber surface prevents nanoparticle aggregation. Aggregation is one of the main attributes contributing to nanoparticle LSPR sensitivity in solution. Thus, this sensor surface would require further modifications to increase its sensitivity to protein binding. Fluorescence spectroscopy was used as an alternative detection method to confirm protein binding on the surface by employing Rhodamine tagged proteins.

3.2 Experimental Details.

Materials. Polyvinyl Alcohol (PVA, Mw 146-180 kDa), isopropyl alcohol (IPA), silver nitrate ($AgNO_3$), ethylenediaminetetraacetic acid (EDTA), sodium hydroxide (NaOH), nickel (II) chloride ($NiCl_2$), copper (II) Sulfate Pentahydrate ($CuSO_4$), Biotin-Nitriloacetic Acid (NTA), and Neutravidin (Mw 66 kDa) were purchased from Sigma-Aldrich (St. Louis, MO). 50 wt. % Glutaraldehyde was purchased from Electron Microscopy Services (Hatfield, PA). NHS-Rhodamine was purchased from Thermo Fisher Scientific (Waltham, MA). The Amicron centrifuge filter columns (3 kDa) were purchased from EMD Millipore (Burlington, MA).

Instruments. The electrospinning was conducted on a home-built device composing of a variable power supply controller, a syringe pump, and a rotating disc collector. A Hitachi-1000 scanning electron microscope (SEM) was used to characterize the nanofiber and nanoparticle dimensions. Absorbance spectra were a Cary50 from Agilent (Santa Clara, CA). Fluorescence spectroscopy was conducted on a QM-400 Fluorometer from Horiba Scientific (Kyoto, Japan).

Sol Gel Preparation. A 6.6% w/v PVA sol-gel solution was prepared by dissolving 330mg of PVA into 4mL of deionized water obtained from an ultrapure filtration system. While PVA does dissolve in water, it requires time to fully hydrate and increased temperature to fully dissolve the polymer. The polymer was split into three portions to assist the dissolution process. The first portion was placed into 4ml of deionized water and heated close to boiling to dissolve the polymer. Once the first portion was fully dissolved, the second portion was added, and the process repeated for the final portion. The resulting solution is a clear homogenous mixture of dissolved PVA with no clumps. An aliquot of 0.5mL glutaraldehyde solution (50 wt.% concentration) was added into the sol-gel to facilitate the cross—linking process to ensure the nanofibers would not dissolve in water. A small amount (0.5mL) of isopropyl alcohol to act as a surfactant and lower the surface tension of the sol-gel to maintain a constant Taylor cone was used to ensure the fabricated fibers were uniform and have smaller diameters.

Electrospun Nanofiber Fabrication. The PVA sol-gel solutions were loaded into a plastic syringe equipped with a 23-gauge blunt-tip dispensing needle and was electrospun using a high voltage power supply (Spellman, CZE1000R) at 15kV. Untreated precut glass slides of 1cm x 1cm were attached to foil strips taped onto a rotating aluminum disc collector (8 cm diameter, 5mm width), placed 15 cm from the syringe needle tip. A steady flow of the sol-gel solution was maintained at 1.00 mL/hour using a syringe pump (KD Scientific, 200 Series) to form a Taylor cone for nanofiber formation.[52] The fibers were deposited on top of the glass slides during the electrospinning process. These substrates were then exposed to hydrochloric acid vapor in a sealed chamber for ten minutes to induce cross-linking of the glutaraldehyde to the hydroxyl groups of the PVA. The substrates were then transferred to a vacuum desiccator for one hour to remove any lingering solvent on the substrate. This cross-linking of the PVA nanofiber made the nanofiber stable in an aqueous environment where untreated fibers would dissolve when in an aqueous environment. The fiber dimensions were characterized by SEM imaging.

EDTA-Silver Nanoparticle Synthesis. Ethylenediaminetetraacetic acid (EDTA) capped silver nanoparticles were prepared as followed from Simpson et al's paper[53,54] with some minor modifications[55,56]. All glassware was cleaned with Aqua Regia and rinsed thoroughly with distilled water to remove all lingering acidity. 200mL deionized H_2O with 0.12 mM (9.2mg) EDTA was heated in a 250mL Erlenmeyer flask while stirring at 90° C. 4 mM (32mg) of sodium hydroxide was added to the mixture and heated to boiling. Once boiling, 8.8mg of silver nitrate in 5mL deionized H_2O was slowly added dropwise while stirring. The solution was then boiled for a further 30 minutes with stirring before removing the flask from heat. The solution cooled to room temperature while stirring. These EDTA-capped silver nanoparticles (EDTA-AgNP) were stored in plastic containers wrapped in foil to avoid direct sunlight exposure.

Nanoparticle Attachment to PVA Nanofiber. Nanoparticles were adsorbed onto the PVA nanofiber through electrostatic interaction between the negative charge of deprotonated alcohol groups on the surface from the hydrochloric acid vapor treatment to cross-link hydroxyl group of the PVA to glutaraldehyde. Incubation of 1mL aliquot of

EDTA-capped AgNPs deposited on the surface of the PVA nanofiber substrate. The spotted nanoparticles dried and rinsed with deionized water several times to remove unbound EDTA-AgNPs Both UV-Vis spectroscopy (**Figure 3.1**) and SEM imaging (**Figure 3.2**) were used to characterize the AgNPs.

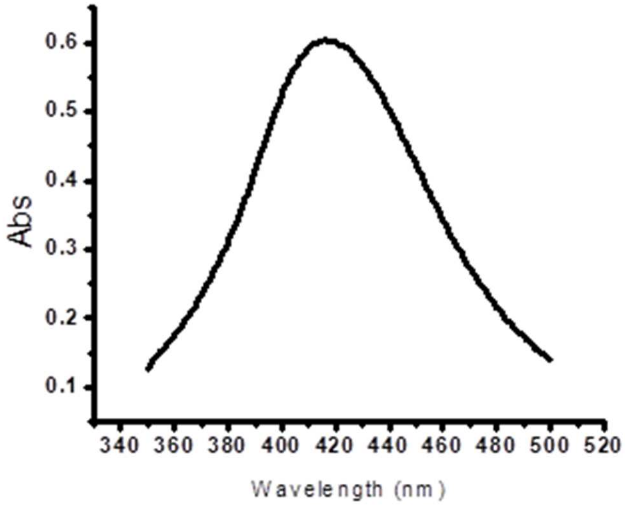

Figure 3.1 Absorbance spectra of the Ethylenediaminetetraacetic acid (EDTA) silver nanoparticles (AgNPs) having a max absorbance peak of 421 nm and a full-width half maximum of 73 nm, correlating to AgNPs with diameters of 50nm.

Sample Preparation. Biotin-NTA was diluted to a 1mM stock concentration. Neutravidin was diluted to 1uM aliquots for stocks used in the experiments. NHS-Rhodamine was diluted to 10uM concentration and mixed with 1uM Neutravidin to fluorescently tag the proteins. The tagged Neutravidin proteins are processed through a 3 kDa centrifuge filter to remove excess unbound Rhodamine molecules and were reconstituted into the desired concentration. The Neutravidin mixed with biotin in a 1:10 ratio of NHS-Neutravidin to Biotin NTA to initiate binding of the Neutravidin-Biotin complex as the sample.

Bulk Refractive Index Sensitivity Study. This study was carried out using UV-Vis spectroscopy for the analysis of EDTA-AgNP PVA nanofibers prepared on a narrow glass slide, which was then placed into a plastic cuvette. The cuvette was filled with varying solvents to induce a change in the refractive index observed by the sensing substrate. UV-VIS readings were taken by the Cary-50 from the 300 nm to 600 nm range to study the maximum peak shift and correlate it with changes in the refractive index. The solvents used were water, methanol, ethanol, propanol, 10%, and 20% glucose solution, which had a refractive index of 1.330, 1.3314, 1.3617, 1.3768, 1.3477, and 1.3635, respectively.

Metal Ion Chelation Study. This study (**Figure 3.4**) tested the EDTA-AgNP ability to chelate metal ions. Metal ions tested in this study were Silver (I), Nickel (II), and Copper (II). The metal ions salt was dissolved into a stock solution and diluted down to varying concentration to verify the chelation property of EDTA-AgNP persist. 1mL of 10nM EDTA-AgNP was mixed with Silver(I) at 170, 850, 1700 PPM; Nickel (II) at 2.4, 12, 24 PPM; and Copper (II) at 2.5, 12.5, 25 PPM. The mixed solution was examined with UV-Vis spectroscopy by a Carry 50.

Fluorescent Detection. This study was carried out a QM-400 fluorescent spectrometer. The EDTA-AgNP/PVA nanofiber incubated a solution 3 mM of nickel (II) chloride on the surface. The substrate was rinsed thoroughly to remove any non-specific binding and excess material off the surface. Various amounts (1 to 15uM) of Rhodamine-NeutrAvidin-Biotin-NTA was spotted on the surface for 10mins before rinsed to remove any unbound protein complex and salts (**Figure 3.5**). Experiments for control parameters were tested by not including the Biotin-NTA to examine non-specific binding and background signal. Another control experiment tested varying amount of Ni^{2+} effects on the binding of the fluorescent protein complex. The prepared sample was analyzed via fluorescent spectrometry, and the fluorescent intensity exhibited by the surface was recorded.

3.3 Results and Discussions.

The polyvinyl alcohol (PVA) nanofibers were synthesized from a sol-gel, a mixture of monomers in a colloidal solution (sol) that facilitates the integerated network (gel) of polymers. The electrospinning of a sol-gel provides a quick and reproducible method of fabricating nanofiber in bulk. The sol-gel for the PVA nanofiber synthesized in this experiment is composed of 6.6% wt. PVA monomers (MW 146-180 kDa) dissolved in deionized water. While PVA monomers readily dissolve in water, creating small batches (<20mL) of solutions comprised of PVA concentrations above 2% will often require additional aid to fully dissolve the polymer.The PVA monomers were split into three equal portions to facilitate the dissolution of the PVA monomers. The first PVA portion was dissolved in deionized water while mixing. The second and third portions were sequentially added to the mixture as the monomers dissolved over time. This dissolution process takes several hours (12+ hrs) at room temperature and can be accelerated (4 hrs) by heating the solution to near boiling temperatures (99 C). Nanofibers can be produced from this 6.6% wt PVA sol-gel with diameters of 300nm with the parameters detailed in the experimental section.

While these pure PVA nanofibers readily dissolving in water is a good factor biodegradability for various applications, this prevents liquid sample handing when utilized in sensor applications. In order to prevent the dissolution of these nanofibers upon incubation of an aqueous sample, glutaraldehyde cross-linking as implemented. This was facilitated by mixing a 50% solution of glutaraldehyde solution with the dissolved PVA mixture. The electrospinning fabrication of nanofibers from this two-part sol-gel has complications. The glutaraldehyde mixture increased sol-gel viscosity, causing several issues. The increase in surface tension of the extruded droplet greatly alters the parameters required to maintain a constant formation of the Taylor cone in electrospinning. The extruded amount of solution becomes sporadic, greatly affecting the fabrication of nanofibers, resulting in nanofibers with diameters of varying sizes (100-800nm) and broken segments instead of continuous strands.

To alleviate these issues, isopropanol was added to the sol-gel for two purposes. The isopropanol behaves as a surfactant and lowers the surface tension of the extruding droplet, which allows the electrospinning process to maintain a consistent and constant flow of solution. Isopropanol also increases the volatility of the sol-gel, allowing the electrified jet to uniformly evaporate as it travels in the Taylor cone towards the sample collection plate. The final mixture composition of 4mL of 6.6%wt PVA (MW 146-180 kDa) in deionized water, 0.5mL of 50% glutaraldehyde, and 0.5mL of isopropanol resulted in continuous and uniformed glutaraldehyde infused nanofibers with diameters of 350nm. These nanofibers are then exposed to hydrochloric acid vapor to facilitate the cross-linking of the glutaraldehyde. The cross-linked nanofibers are then thoroughly washed in deionized water to confirm the cross-linking did occur and remove any remaining hydrochloric acid. The wet nanofibers are then dried and stored for future use. The characterization of the nanofibers was conducted via SEM imaging (**Figure 3.2A**) and confirming continuous nanofiber with diameters of 350nm. Silver nanoparticles were utilized in this sensor application as the functionalized surface for the biological recognition element in this biosensor. Three differnet methods of functionalizing these PVA nanofibers with silver nanoparticles (AgNPs) were explored. The first method attempted to fabricated nanofibers infused with silver nanoparticles. This was accomplished by incorperating silver nitrate into the sol-gel mixture to electrospun nanofibers evenly infused with silver nitrate[57,58]. These nanofibers were then treated with UV exposure to facilitate the transformation of silver nitrate into silver nanoparticles.[57,58] This process did successfully create AgNP infused PVA nanofiber, the density of the AgNPs was not high enough to be optically observed via UV-VIS spectroscopy and not abundant enough to provide areas of functionalization for surface chemistry.

The second method was to separately synthesize silver nanoparticles (AgNPs) and infuse them into the sol-gel to create nanofibers embedded with AgNPs[31,34,59,60]. The AgNPs were synthesized in the process described in the experimental section earlier in this chapter. The ethylenediaminetetraacetic acid (EDTA) serves as the capping reagent to stop nanoparticle growth and stabilizes the nanoparticle in solution. Characterization of the silver nanoparticle was done through UV-VIS spectroscopy (**Figure 3.1**), showing a λ max at 420.93nm, FWHM at 72.95nm, and estimated[61] to be roughly 50nm in diameter from the λ max and confirmed in SEM images. The initial stock concentration of the EDTA-AgNPs of 2.4nM was concentrated through centrifugation to a max concentration of 15nM. Concentrations higher than 15nM suffer from irreversible aggregation and was not used as the resulting sol-gel mixture was not homogenous. While the characterization of these nanofibers via SEM imaging (**Figure 3.2B**) did show successful incorporation of AgNPs, the resulting nanofibers did not exhibit any signs of AgNP trait when observed in UV-VIS spectroscopy regardless of the EDTA-AgNPs used.

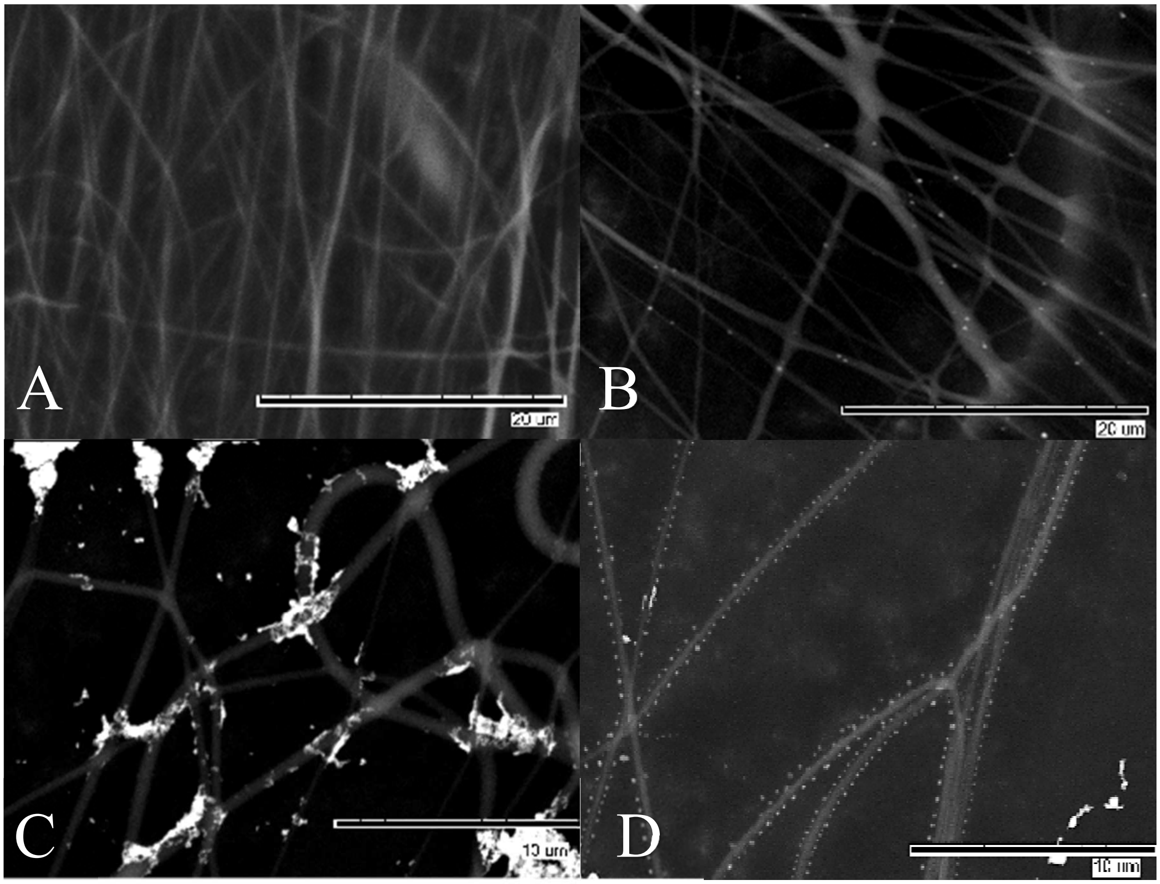

Figure 3.2 (A) Top Left. Polyvinyl alcohol (PVA) nanofiber cross-linked with glutaraldehyde (GA). **(B)** Top Right. PVA nanofiber with silver nanoparticles (AgNPs) generated from embedded silver nitrate ($AgNO_3$) and exposure to UV irradiation. **(C)** Bottom Left. PVA nanofibers incubated with ethylenediaminetetraacetic acid (EDTA) capped AgNPs. **(D)** Bottom Right. PVA nanofiber with EDTA-AgNP after thorourghly rinsing**.**

The third method utilizes surface adsorption of the EDTA-AgNPs onto the PVA nanofibers. Because of the high surface area to volume ratio of nanofibers, this provided higher surface adsorption than a flat substrate. A 1mL aliquots of EDTA-AgNPs were incubated on the nanofiber surface and dried over time in a vacuum desiccator. The EDTA-AgNPs decorated nanofibers (**Figure 3.2C**) are then thoroughly rinsed and re-dried in the vacuum desiccator (**Figure 3.2D**) and saved for future use. This EDTA-AgNP adsorbed on the nanofiber substrate through this process resulted in a local surface plasmon resonance (LSPR) responsive surface to bulk refractive index with strong linear correlation (R^2=0.98) that could be observed through UV-VIS spectroscopy (**Figure 3.3**).

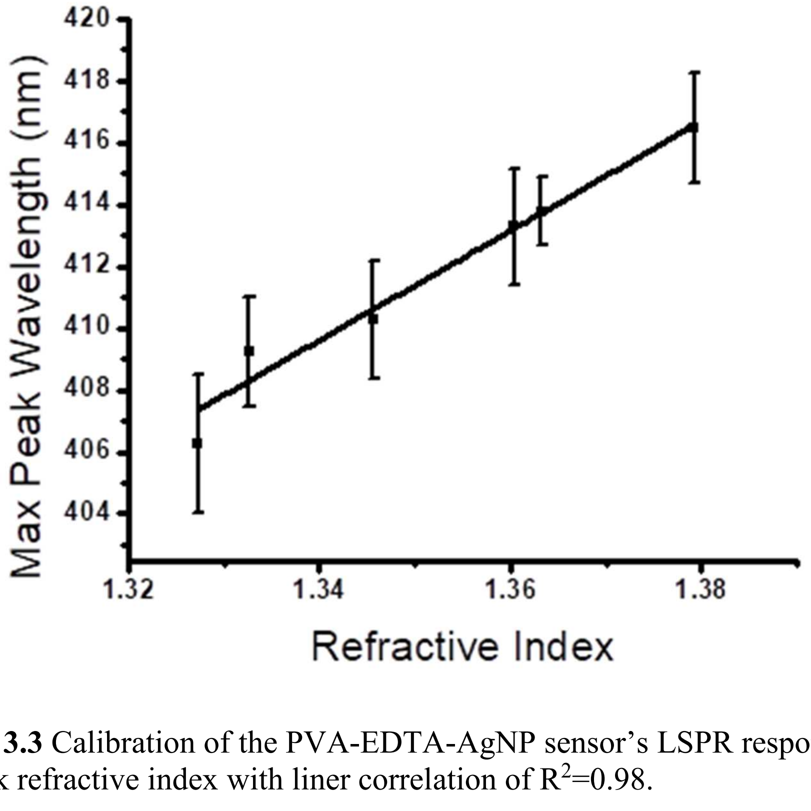

Figure 3.3 Calibration of the PVA-EDTA-AgNP sensor's LSPR response to changes in the bulk refractive index with liner correlation of R^2=0.98.

Because EDTA was used as the capping reagent for the silver nanoparticles, the EDTA-AgNPs may retain metal chelating properties. Exposing the EDTA-AgNPs adsorbed on the nanofiber substrate to metal ions of Silver (I), Nickel (II), and Copper (II) did not show a sensitive LSPR response. Thus, the metal ion chelation study was conducted with the nanoparticles and metal ions in solution. UV-VIS spectroscopy (**Figure 3.4**) of the EDTA-AgNPs and metal ion mixture verifies that aggregation of the nanoparticles occurred proportionally to the concentrations of the metal ions. This confirmed that the EDTA-AgNPs on the nanofiber surface is capable of chelating metal ions and by adsorbing the nanoparticles on the nanofiber surface prevented aggregation of the nanoparticles. This novel surface can be used as a biological recognition element in a biosensor.

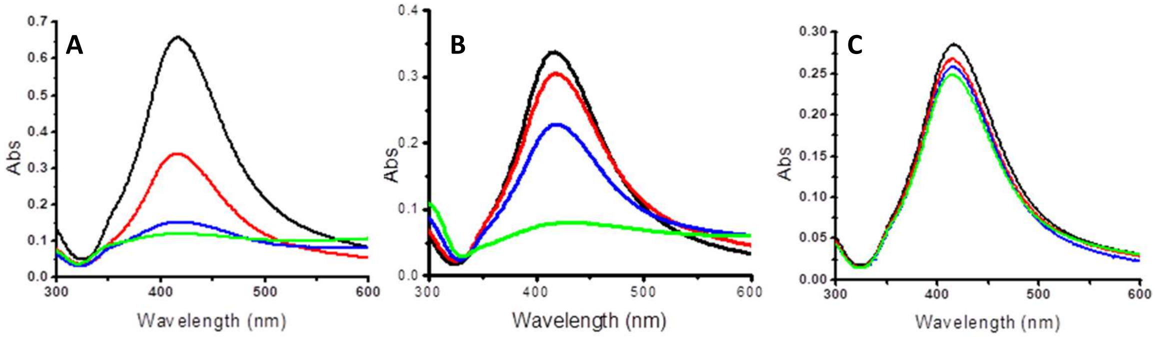

Figure 3.4 Metal ion chelation to the EDTA-Silver Nanoparticles as they bind to various metal ions. **(A)** Silver (I) ions. Black: 0 PPM, Red: 170 PPM, Blue: 850 PPM, and Green: 1700 PPM. **(B)** Nickel (II) ions. Black: 0 PPM, Red:2.4 PPM, Blue: 12 PPM, and Green: 24 PPM. **(C)** Copper (II) Ion. Black: 0 PPM, Red: 2.5 PPM, Blue: 12.5 PPM, and Green: 25 PPM.

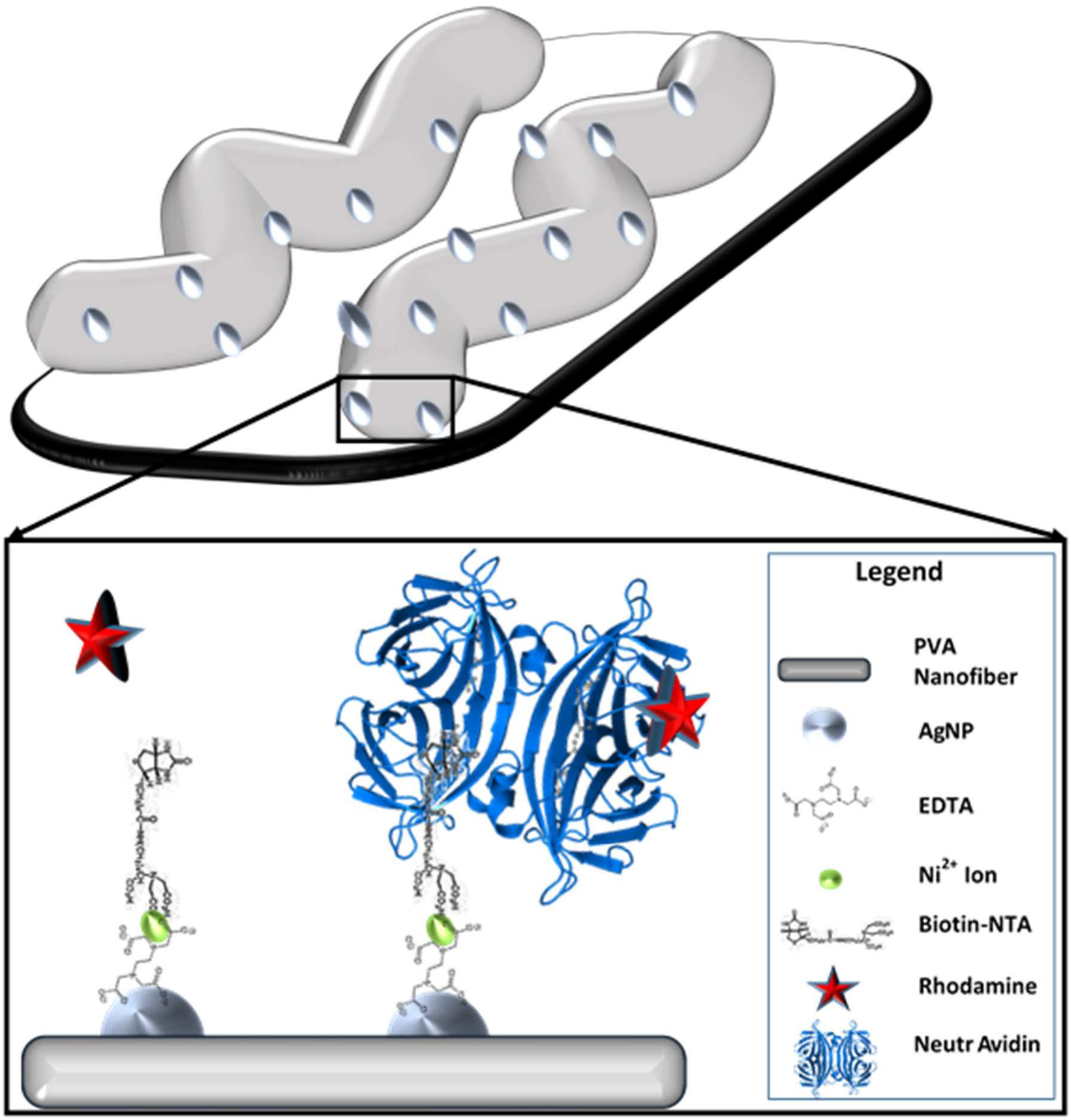

Figure 3.5 Polyvinyl alcohol (PVA) nanofibers with diameter of 350nm are electrospun onto the surface of a glass slide. A 6nM solution of 50nm EDTA-AgNPs is incubated onto surface of the PVA fibers for 1 hour and then thoroughly rinsed with diH$_2$O. Once the substrate is dried a 3.4mM solution of NiCl solution is incubated on surface of substrate to induce chelation of Ni^{2+} ions to the EDTA for 30 mins and then thoroughly rinsed with diH$_2$O. Analyte samples of 0.1mg/ml to 1.0mg/ml of Rhodamine-tagged Neutravidin-Biotin-NTA complex were incubated on the surface for 10 mins to bind to the Ni^{2+} ions that have been chelated by the EDTA-AgNP surface and then the substrate is thoroughly rinsed with diH2O.

Nickel (II) and NTA is a well-studied metal chelation system often used in functionalized silica gel columns.[62] **Figure 3.5** outlines the surface chemistry binding mechanism used in this experiment. The electrospun PVA nanofibers collected on glass slides and are incubated with EDTA-AgNP to give surface specificity with the EDTA functional group. Using the EDTA metal ion chelating property, Ni^{2+} chelated onto the EDTA surface but was still exposed enough to facilitate the binding of Ni2+ to NTA molecules. By having the EDTA-AgNP bound to a surface, as is the case with the PVA nanoparticle system, it prevents the nanoparticles from aggregating when incubating with the Ni^{2+} ions. These exposed Ni^{2+} ions provide good binding sites for NTA and other NTA modified molecules. The NeutrAvidin-Biotin binding complex has been well studied as a model protein-ligand binding interaction. The biotin used was modified with an NTA attachment, which will allow biding to the exposed Ni2+ ions on the surface. NTA-Biotin attachment to the surface before incubation of NeutrAvidin was tested but showed very low levels of binding, which may have been due to the orientation of the NTA-biotin on the surface[63,64], thus prior mixing of the NTA-Biotin with NeutrAvidin was performed and showed much higher binding. The detection of the binding was carried out using NHS-Rhodamine, a fluorescent dye. NHS-Rhodamine was attached to NeutrAvidin following a standard procedure from Thermo Fisher Scientific. These Rhodamine-NeutrAvidin preparations also included sample purification with a 3kDa centrifuge filter from Amicron to remove non-reacted dyes and were prepared weekly and stored in a refrigerator before use. Characterization (Figure 4A) of the labeled protein was carried out, revealing the stoichiometry between Rhodamine to Neutravidin was 4:1 ratio. This fluorescent dye allowed confirmation of the binding events. Control tests (**Figure 3.6**) show that without the NTA-Biotin that the protein did exhibit nonspecific binding to the surface when using Avidin but was significantly reduced when using NeutrAvidin.

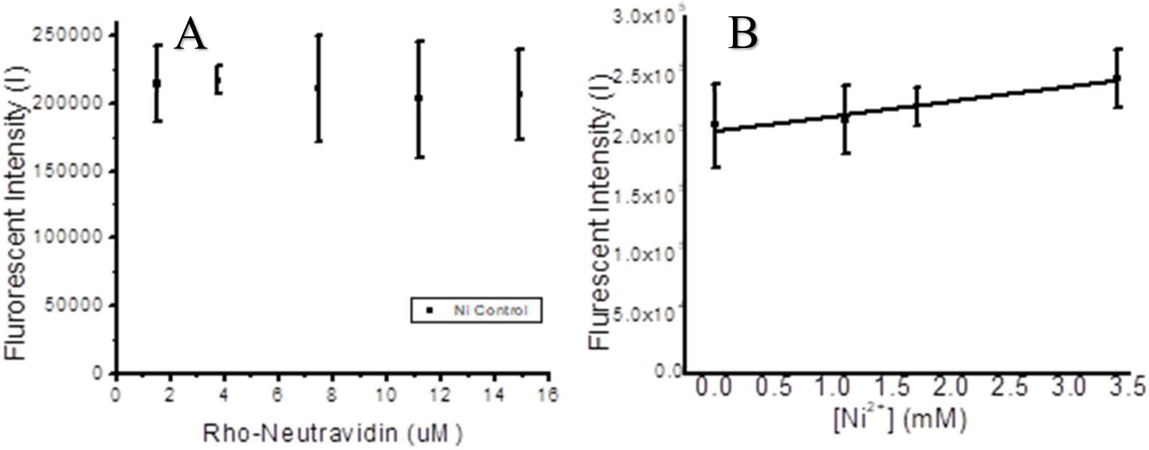

Figure 3.6 (A) Left. Control study for unspecific binding, no Biotin-NTA, showing a baseline amount of nonspecific binding of the NHS-Neutravidin to the EDTA-AgNP PVA nanofiber surface. **(B)** Right. Control study for nickel dependency of complex binding to the surface shows a linear correlation between the increase in nickel ion concentration and resulting fluorescence signal from bound protein.

Control studies were carried out to examine both the background fluorescence and effects of Ni^{2+} concentration on NTA-protein complex binding on the surface. The background control tested the non-specific binding of NHS-Neutravidin onto the surface by not including the NTA-Biotin. The results (**Figure 3.6A**) shows that the background signal from the non-specific binding is the same level regardless of the amount (1 μM to 15 μM) of NHS-Neutravidin incubated on the surface. Ni^{2+} concentration on NTA-protein complex binding experiment was tested by using a set concentration of 1 μM Rhodamine-NeutrAvidin-Biotin-NTA complex while varying the concentration (0 μM to 3.4 μM) of

Ni2+ to examine the relationship between Ni2+ concentration and fluorescent intensity from the protein binding (**Figure 3.6B**). The linear correlation (R^2=0.964) indicates that the NTA-protein complex binding onto the surface is dependent on the presence of Ni^{2+} chelated to the EDTA-AgNP on the surface of the PVA nanofibers.

With the control studies done, the next study was the sensitivity of detection of varying amounts of the protein complex binding to this novel substrate surface. The concentration of Ni^{2+} on the surface was set by incubating 3.4 mM of $NiCl_2$ on the surface and thoroughly rinsed to remove non-bound nickel and chloride ions. With a high concentration of Ni2+ on the surface, this sets up a large surface area of possible binding sites for these protein complex containing NTA. The NTA binds to the exposed Ni^{2+} ion that is partially chelated onto the EDTA molecules, which are bound to the silver nanoparticles on the nanofiber surface. The sensitivity of the substrate to the bound protein complex was tested using varying concentrations of the rhodamine-NeutrAvidin-biotin-NTA complex.

The data was collected from concentrations ranging from 0 to 14 μM were plotted into a calibration curve (**Figure 3.7**), which shows a strong linear correlation (R^2=0.964) between the amount of protein complex incubated and the fluorescent intensity recorded. This sensor has a limit of detection at 1.11μM (66.6 μg/mL) and a limit of quantification at 3.70μM (222 μg/mL) of the rhodamine tagged NeutrAvidin. Secondary chelation was conducted with concentrated EDTA solution to rinse the nanofiber surface to dislodge the bound NTA-protein complex. The unbound EDTA outcompetes the NTA bound on the

Ni^{2+} ions on the surface and breaks the bridge between the protein complex and the surface, facilitating the removal of the analyte and regenerating the sensor surface.

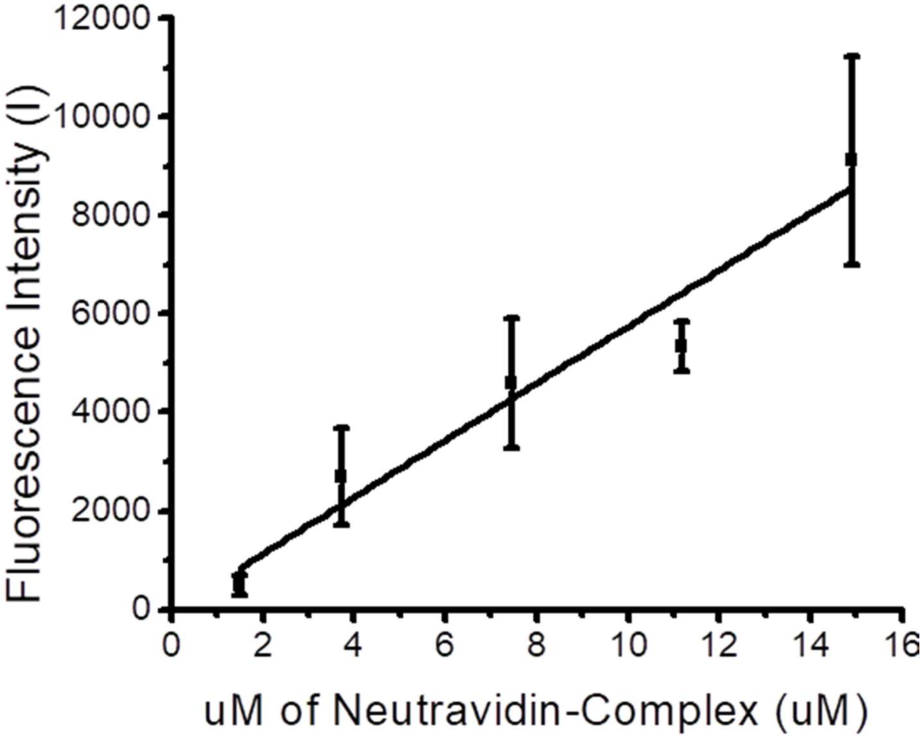

Figure 3.7 Fluorescent reading of various sample concentration was taken and a calibration curve showing linear correlation ($R^2 = 0.964$) between fluorescent intensity and concentration of the sample with error bars showing the variation between substrate sensitivity.

3.4 Conclusions.

We have created a nanofiber substrate capable of forming metal ion bridges for selective capture of metal ions binding analytes such as NTA or His-tagged functionalized biomolecules. This enables on-chip enrichment and detection with a fluorescent spectrometer. In this study, nickel (II) ions were incorporated into the binding scheme to facilitate the recruitment of NTA-biotin to the sensor surface. The biotin moiety surface as the surface ligand-receptor for the Neutravidin tagged with rhodamine and fluorescence spectroscopy was used to optically confirm and quantify the presence of the bound proteins. Control studies that were carried out showed a low level of nonspecific binding. But the amount of nonspecific binding observed was uniform across the concentration gradient, signifying that increases in fluorescent readings can be attributed to binding events from the Rhodamine-Neutravidin-NTA-Biotin complex anchored onto the surface.

While this novel platform can concentrate analytes on the surface through this specific binding interaction, this surface interaction is simple and can be further used for protein separation techniques that target his-tagged protein. This sensor surface can also chelate as copper and iron ions. These metal ions can serve as anchor points to facilitate biorecognition to metal binding entities or metalloproteins, such as Copper Binding Protein (CBP) family found in the liver that binds copper ions, and iron \-binding proteins include transferrin, hemoglobin among many others. Additionally, post-experimental washing of the sensor surface with a high EDTA concentration solution has shown to elute the bound analyte due to EDTA’s higher binding affinity to the nickel ions than both the partial EDTA and the NTA, enabling the regeneration of this sensor surface for future use.

References

(1) Yoo, J. J.; Kim, C.; Chung, C. W.; Jeong, Y. Il; Kang, D. H. 5-Aminolevulinic Acid-Incorporated Poly(Vinyl Alcohol) Nanofiber-Coated Metal Stent for Application in Photodynamic Therapy. *Int. J. Nanomedicine* **2012**, *7*, 1997–2005.

(2) Chun, J. Y.; Kang, H. K.; Jeong, L.; Kang, Y. O.; Oh, J. E.; Yeo, I. S.; Jung, S. Y.; Park, W. H.; Min, B. M. Epidermal Cellular Response to Poly(Vinyl Alcohol) Nanofibers Containing Silver Nanoparticles. *Colloids Surfaces B Biointerfaces* **2010**, *78* (2), 334–342.

(3) Koosha, M.; Mirzadeh, H.; Shokrgozar, M. A.; Farokhi, M. Nanoclay-Reinforced Electrospun Chitosan/PVA Nanocomposite Nanofibers for Biomedical Applications. *RSC Adv.* **2015**, *5* (14), 10479–10487.

(4) Yang, D.; Li, Y.; Nie, J. Preparation of Gelatin/PVA Nanofibers and Their Potential Application in Controlled Release of Drugs. *Carbohydr. Polym.* **2007**, *69* (3), 538–543.

(5) Li, X.; Kanjwal, M. A.; Lin, L.; Chronakis, I. S. Electrospun Polyvinyl-Alcohol Nanofibers as Oral Fast-Dissolving Delivery System of Caffeine and Riboflavin. *Colloids Surfaces B Biointerfaces* **2013**, *103*, 182–188.

(6) Zhang, X.; Tang, K.; Zheng, X. Electrospinning and Crosslinking of COL/PVA Nanofiber-Microsphere Containing Salicylic Acid for Drug Delivery. *J. Bionic Eng.* **2016**, *13* (1), 143–149.

(7) Sharma, A.; Gupta, A.; Rath, G.; Goyal, A.; Mathur, R. B.; Dhakate, S. R. Electrospun Composite Nanofiber-Based Transmucosal Patch for Anti-Diabetic Drug Delivery. *J. Mater. Chem. B* **2013**, *1* (27), 3410–3418.

(8) Enderami, S. E.; Kehtari, M.; Abazari, M. F.; Ghoraeian, P.; Nouri Aleagha, M.; Soleimanifar, F.; Soleimani, M.; Mortazavi, Y.; Nadri, S.; Mostafavi, H.; et al. Generation of Insulin-Producing Cells from Human Induced Pluripotent Stem Cells on PLLA/PVA Nanofiber Scaffold. *Artif. Cells, Nanomedicine Biotechnol.*

2018, *46* (sup1), 1062–1069.

(9) Asran, A. S.; Razghandi, K.; Aggarwal, N.; Michler, G. H.; Groth, T. Nanofibers from Blends of Polyvinyl Alcohol and Polyhydroxy Butyrate as Potential Scaffold Material for Tissue Engineering of Skin. *Biomacromolecules* **2010**, *11* (12), 3413–3421.

(10) Abdal-Hay, A.; Hussein, K. H.; Casettari, L.; Khalil, K. A.; Hamdy, A. S. Fabrication of Novel High Performance Ductile Poly(Lactic Acid) Nanofiber Scaffold Coated with Poly(Vinyl Alcohol) for Tissue Engineering Applications. *Mater. Sci. Eng. C* **2016**, *60*, 143–150.

(11) Abedi, G.; Sotoudeh, A.; Soleymani, M.; Shafiee, A.; Mortazavi, P.; Aflatoonian, M. R. A Collagen-Poly(Vinyl Alcohol) Nanofiber Scaffold for Cartilage Repair. *J. Biomater. Sci. Polym. Ed.* **2011**, *22* (18), 2445–2455.

(12) Yanilmaz, M.; Lu, Y.; Dirican, M.; Fu, K.; Zhang, X. Nanoparticle-on-Nanofiber Hybrid Membrane Separators for Lithium-Ion Batteries via Combining Electrospraying and Electrospinning Techniques. *J. Memb. Sci.* **2014**, *456*, 57–65.

(13) Lee, H. J.; Lim, J. M.; Kim, H. W.; Jeong, S. H.; Eom, S. W.; Hong, Y. T.; Lee, S. Y. Electrospun Polyetherimide Nanofiber Mat-Reinforced, Permselective Polyvinyl Alcohol Composite Separator Membranes: A Membrane-Driven Step Closer toward Rechargeable Zinc-Air Batteries. *J. Memb. Sci.* **2016**, *499*, 526–537.

(14) Liu, C.; Shao, Z.; Wang, J.; Lu, C.; Wang, Z. Eco-Friendly Polyvinyl Alcohol/Cellulose Nanofiber-Li+ Composite Separator for High-Performance Lithium-Ion Batteries. *RSC Adv.* **2016**, *6* (100), 97912–97920.

(15) Gu, P.; Zheng, M.; Zhao, Q.; Xiao, X.; Xue, H.; Pang, H. Rechargeable Zinc-Air Batteries: A Promising Way to Green Energy. *J. Mater. Chem. A* **2017**, *5* (17), 7651–7666.

(16) Dirican, M.; Yanilmaz, M.; Fu, K.; Yildiz, O.; Kizil, H.; Hu, Y.; Zhang, X. Carbon-Confined PVA-Derived Silicon/Silica/Carbon Nanofiber Composites as

Anode for Lithium-Ion Batteries. *J. Electrochem. Soc.* **2014**, *161* (14), A2197–A2203.

(17) Bian, J.; Olesik, S. V. Surface Assisted Laser Desorption/Ionization Time of Flight Mass Spectrometry of Small Drug Molecules and High Molecular Weight Synthetic/Biological Polymer Using Electrospun Composite Nanofibers. *Analyst* **2017**, *142*, 1125–1132.

(18) Lu, T.; Olesik, S. V. Electrospun Nanofibers as Substrates for Surface-Assisted Laser Desorption/Ionization and Matrix-Enhanced Surface-Assisted Laser Desorption/Ionization Mass Spectrometry. *Anal. Chem.* **2013**, *85* (9), 4384–4391.

(19) Bian, J.; Olesik, S. V. Surface-Assisted Laser Desorption/Ionization Time-of-Flight Mass Spectrometry of Small Drug Molecules and High Molecular Weight Synthetic/Biological Polymers Using Electrospun Composite Nanofibers. *Analyst* **2017**, *142* (7), 1125–1132.

(20) Naebe, M.; Lin, T.; Staiger, M. P.; Dai, L.; Wang, X. Electrospun Single-Walled Carbon Nanotube/Polyvinyl Alcohol Composite Nanofibers: Structure-Property Relationships. *Nanotechnology* **2008**, *19* (30).

(21) Xiao, S.; Shen, M.; Guo, R.; Huang, Q.; Wang, S.; Shi, X. Fabrication of Multiwalled Carbon Nanotube-Reinforced Electrospun Polymer Nanofibers Containing Zero-Valent Iron Nanoparticles for Environmental Applications. *J. Mater. Chem.* **2010**, *20* (27), 5700–5708.

(22) Kim, M. J.; Lee, J.; Jung, D.; Shim, S. E. Electrospun Poly(Vinyl Alcohol) Nanofibers Incorporating PEGylated Multi-Wall Carbon Nanotube. *Synth. Met.* **2010**, *160* (13–14), 1410–1414.

(23) Mantilaka, M. M. M. G. P. G.; De Silva, R. T.; Ratnayake, S. P.; Amaratunga, G.; de Silva, K. M. N. Photocatalytic Activity of Electrospun MgO Nanofibres: Synthesis, Characterization and Applications. *Mater. Res. Bull.* **2018**, *99*, 204–210.

(24) Jo, S.; Kim, J.; Noh, J.; Kim, D.; Jang, G.; Lee, N.; Lee, E.; Lee, T. S. Conjugated

Polymer Dots-on-Electrospun Fibers as a Fluorescent Nanofibrous Sensor for Nerve Gas Stimulant. *ACS Appl. Mater. Interfaces* **2014**, *6* (24), 22884–22893.

(25) Li, M.; Zhang, J.; Zhang, H.; Liu, Y.; Wang, C.; Xu, X.; Tang, Y.; Yang, B. Electrospinning: A Facile Method to Disperse Fluorescent Quantum Dots in Nanofibers without Förster Resonance Energy Transfer. *Adv. Funct. Mater.* **2007**, *17*, 3650–3656.

(26) De Melo, E. F.; Alves, K. G. B.; Junior, S. A.; De Melo, C. P. Synthesis of Fluorescent PVA/Polypyrrole-ZnO Nanofibers. *J. Mater. Sci.* **2013**, *48* (10), 3652–3658.

(27) Zhang, W.; Yan, E.; Huang, Z.; Wang, C.; Xin, Y.; Zhao, Q.; Tong, Y. Preparation and Study of PPV/PVA Nanofibers via Electrospinning PPV Precursor Alcohol Solution. *Eur. Polym. J.* **2007**, *43* (3), 802–807.

(28) He, J.; He, Y.; Chen, Y.; Zhang, X.; Hu, C.; Zhuang, J.; Lei, B.; Liu, Y. Construction and Multifunctional Applications of Carbon Dots/PVA Nanofibers with Phosphorescence and Thermally Activated Delayed Fluorescence. *Chem. Eng. J.* **2018**, *347* (April), 505–513.

(29) Zhang, P.; Zhao, X.; Ji, Y.; Ouyang, Z.; Wen, X.; Li, J.; Su, Z.; Wei, G. Electrospinning Graphene Quantum Dots into a Nanofibrous Membrane for Dual-Purpose Fluorescent and Electrochemical Biosensors. *J. Mater. Chem. B* **2015**, *3* (12), 2487–2496.

(30) Fang, X.; Ma, H.; Xiao, S.; Shen, M.; Guo, R.; Cao, X.; Shi, X. Facile Immobilization of Gold Nanoparticles into Electrospun Polyethyleneimine/Polyvinyl Alcohol Nanofibers for Catalytic Applications. *J. Mater. Chem.* **2011**, *21* (12), 4493–4501.

(31) Jin, W. J.; Jeon, H. J.; Kim, J. H.; Youk, J. H. A Study on the Preparation of Poly(Vinyl Alcohol) Nanofibers Containing Silver Nanoparticles. *Synth. Met.* **2007**, *157* (10–12), 454–459.

(32) Bai, J.; Li, Y.; Yang, S.; Du, J.; Wang, S.; Zheng, J.; Wang, Y.; Yang, Q.; Chen, X.; Jing, X. A Simple and Effective Route for the Preparation of Poly(Vinylalcohol) (PVA) Nanofibers Containing Gold Nanoparticles by Electrospinning Method. *Solid State Commun.* **2007**, *141* (5), 292–295.

(33) Celebioglu, A.; Aytac, Z.; Umu, O. C. O.; Dana, A.; Tekinay, T.; Uyar, T. One-Step Synthesis of Size-Tunable Ag Nanoparticles Incorporated in Electrospun PVA/Cyclodextrin Nanofibers. *Carbohydr. Polym.* **2014**, *99*, 808–816.

(34) He, D.; Hu, B.; Yao, Q. F.; Wang, K.; Yu, S. H. Large-Scale Synthesis of Flexible Free-Standing SERS Substrates with High Sensitivity: Electrospun PVA Nanofibers Embedded with Controlled Alignment of Silver Nanoparticles. *ACS Nano* **2009**, *3* (12), 3993–4002.

(35) Yang, Z.; Peng, H.; Wang, W.; Liu, T. Crystallization Behavior of Poly(ε-Caprolactone)/Layered Double Hydroxide Nanocomposites. *J. Appl. Polym. Sci.* **2010**, *116* (5), 2658–2667.

(36) Qin, X.; Dou, G.; Jiang, G.; Zhang, S. Characterization of Poly (Vinyl Alcohol) Nanofiber Mats Cross-Linked with Glutaraldehyde. *J. Ind. Text.* **2013**, *43* (1), 34–44.

(37) Tang, C.; Saquing, C. D.; Harding, J. R.; Khan, S. A. In Situ Cross-Linking of Electrospun Poly(Vinyl Alcohol) Nanofibers. *Macromolecules* **2010**, *43* (2), 630–637.

(38) Li, Y.; Yao, S. High Stability under Extreme Condition of the Poly(Vinyl Alcohol) Nanofibers Crosslinked by Glutaraldehyde in Organic Medium. *Polym. Degrad. Stab.* **2017**, *137*, 229–237.

(39) Destaye, A. G.; Lin, C. K.; Lee, C. K. Glutaraldehyde Vapor Cross-Linked Nanofibrous PVA Mat with in Situ Formed Silver Nanoparticles. *ACS Appl. Mater. Interfaces* **2013**, *5* (11), 4745–4752.

(40) Marega, C.; Maculan, J.; Andrea Rizzi, G.; Saini, R.; Cavaliere, E.; Gavioli, L.;

Cattelan, M.; Giallongo, G.; Marigo, A.; Granozzi, G. Polyvinyl Alcohol Electrospun Nanofibers Containing Ag Nanoparticles Used as Sensors for the Detection of Biogenic Amines. *Nanotechnology* **2015**, *26* (7), 1–9.

(41) Li, Y.; Zhang, P.; Ouyang, Z.; Zhang, M.; Lin, Z.; Li, J.; Su, Z.; Wei, G. Nanoscale Graphene Doped with Highly Dispersed Silver Nanoparticles: Quick Synthesis, Facile Fabrication of 3D Membrane-Modified Electrode, and Super Performance for Electrochemical Sensing. *Adv. Funct. Mater.* **2016**, *26* (13), 2122–2134.

(42) Chen, C.; Tang, Y.; Vlahovic, B.; Yan, F. Electrospun Polymer Nanofibers Decorated with Noble Metal Nanoparticles for Chemical Sensing. *Nanoscale Res. Lett.* **2017**, *12* (451), 1–15.

(43) Liu, N.; Fang, G.; Wan, J.; Zhou, H.; Long, H.; Zhao, X. Electrospun PEDOT:PSS-PVA Nanofiber Based Ultrahigh-Strain Sensors with Controllable Electrical Conductivity. *J. Mater. Chem.* **2011**, *21* (47), 18962–18966.

(44) Leibold, E. A.; Guo, B. Iron-Dependent Regulation of Iron-Responsive Element Binding Protein. **1992**.

(45) Jensen, T. R.; Malinsky, M. D.; Haynes, C. L.; Van Duyne, R. P. Nanosphere Lithography: Tunable Localized Surface Plasmon Resonance Spectra of Silver Nanoparticles. *J. Phys. Chem. B* **2000**, *104* (45), 10549–10556.

(46) Haes, A. J.; Van Duyne, R. P. A Nanoscale Optical Biosensor: Sensitivity and Selectivity of an Approach Based on the Localized Surface Plasmon Resonance Spectroscopy of Triangular Silver Nanoparticles. *J. Am. Chem. Soc.* **2002**, *124* (35), 10596–10604.

(47) Malinsky, M. D.; Lance Kelly, K.; Schatz, G. C.; van Duyne, R. P. Nanosphere Lithography: Effect of Substrate on the Localized Surface Plasmon Resonance Spectrum of Silver Nanoparticles. *J. Phys. Chem. B* **2001**, *105* (12), 2343–2350.

(48) Fuku, K.; Hayashi, R.; Takakura, S.; Kamegawa, T.; Mori, K.; Yamashita, H. The

Synthesis of Size- and Color-Controlled Silver Nanoparticles by Using Microwave Heating and Their Enhanced Catalytic Activity by Localized Surface Plasmon Resonance. *Angew. Chemie - Int. Ed.* **2013**, *52* (29), 7446–7450.

(49) Chen, Y. Q.; Lu, C. J. Surface Modification on Silver Nanoparticles for Enhancing Vapor Selectivity of Localized Surface Plasmon Resonance Sensors. *Sensors Actuators, B Chem.* **2009**, *135* (2), 492–498.

(50) Chen, C. Y.; Hinman, S. S.; Duan, J.; Cheng, Q. Nanoglassified, Optically-Active Monolayer Films of Gold Nanoparticles for in Situ Orthogonal Detection by Localized Surface Plasmon Resonance and Surface-Assisted Laser Desorption/Ionization-MS. *Anal. Chem.* **2014**, *86* (24), 11942–11945.

(51) Bao, Y.; Fong, H.; Jiang, C. Manipulating the Collective Surface Plasmon Resonances of Aligned Gold Nanorods in Electrospun Composite Nanofibers. *J. Phys. Chem. C* **2013**, *117* (41), 21490–21497.

(52) Davis, B. W.; Burris, A. J.; Niamnont, N.; Hare, C. D.; Chen, C.; Sukwattanasinitt, M.; Cheng, Q. Dual-Mode Optical Sensing of Organic Vapors and Proteins with Polydiacetylene (PDA)-Embedded Electrospun Nano Fi Bers. *Langmuir* **2014**, *30*, 9616–9622.

(53) Simpson, J.; Craig, D.; Faulds, K.; Graham, D. Mixed-Monolayer Glyconanoparticles for the Detection of Cholera Toxin by Surface Enhanced Raman Spectroscopy. *Nanoscale Horiz.* **2016**, *1* (1), 60–63.

(54) Simpson, J.; Craig, D.; Faulds, K.; Graham, D. ESI: Mixed-Monolayer Glyconanoparticles for the Detection of Cholera Toxin by SERS. *Nanoscale Horiz.* **2015**, No. 3.

(55) Kemp, M. M.; Kumar, A.; Mousa, S.; Park, T.-J.; Ajayan, P.; Kubotera, N.; Mousa, S.; Linhart, R. J. Synthesis of Gold and Silver Nanoparticles Stabilized with Glycosaminoglycans Having Distinctive Biological Activities. *Biotechnol. Bioeng.* **2010**, *27* (3), 2528–2543.

(56) P.K., Na.; D.P., K.; A., D.; D.K., D. Experimental Investigation of Viscosity and Specific Heat of Silicon Dioxide Nanofluid. *Micro Nano Lett.* **2007**, *2* (3), 67–71.

(57) Silva, A. M. B.; de Araújo, C. B.; Santos-Silva, S.; Galembeck, A. Silver Nanoparticle in Situ Growth within Crosslinked Poly(Ester-Co-Styrene) Induced by UV Irradiation: Aggregation Control with Exposure Time. *J. Phys. Chem. Solids* **2007**, *68* (5–6), 729–733.

(58) Balan, L.; Malval, J.-P.; Lougnot, D.-J. In Situ Photochemically Assisted Synthesis of Silver Nanoparticles in Polymer Matrixes. *Silver nanoparticles* **2010**, 79–92.

(59) Saquing, C. D.; Manasco, J. L.; Khan, S. A. Electrospun Nanoparticle-Nanofiber Composites via a One-Step Synthesis. *Small* **2009**, *5* (8), 944–951.

(60) Kong, H.; Jang, J. One-Step Fabrication of Silver Nanoparticle Embedded Polymer Nanofibers by Radical-Mediated Dispersion Polymerization. *Chem. Commun.* **2006**, No. 28, 3010–3012.

(61) Navarro, J. R. G.; Werts, M. H. V. Resonant Light Scattering Spectroscopy of Gold, Silver and Gold-Silver Alloy Nanoparticles and Optical Detection in Microfluidic Channels. *Analyst* **2013**, *138* (2), 583–592.

(62) Haddour, N.; Cosnier, S.; Gondran, C. Electrogeneration of a Poly(Pyrrole)-NTA Chelator Film for a Reversible Oriented Immobilization of Histidine-Tagged Proteins. *J. Am. Chem. Soc.* **2005**, *127* (16), 5752–5753.

(63) Huang, S. C.; Stump, M. D.; Weiss, R.; Caldwell, K. D. Binding of Biotinylated DNA to Streptavidin-Coated Polystyrene Latex: Effects of Chain Length and Particle Size. *Anal. Biochem.* **1996**, *237* (237), 115–122.

(64) Jarvis, R. A.; Bryers, J. D. Effects of Controlled Fibronectin Surface Orientation on Subsequent Staphylococcus Epidermidis Adhesion. *J. Biomed. Mater. Res. - Part A* **2005**, *75* (1), 41–55.

Chapter 4. Fabrication of 3D printed Prisms as Optical Components for LSPR Detection of Proteins

4.1 Introduction.

3D printing is an additive manufacturing process of fabricating three dimensional solid objects through fusing deposited material in a layer by layer process (see Chapter 1: Introduction for more details). This enables a wide complexity of shapes for rapid prototyping and mass production of custom objects for various applications[1–8]. 3D printing technology has open a new avenue in science through the facile fabrication of custom components with high resolution and cost efficiency of both additive manufacturing[1] and translating novel ideas into versatile applications[3,9,10].

While 3D printing has been focused on additive manufacturing for custom parts, it has recently been applied to fabricating whole sensor devices. The main route of application has been demonstrated in 3D printing microfluidic devices. This simplifies the traditional PDMS mask and mold techniques by fabricating a fully functioning device in one simple task and mitigates key issues such as improper sealing and bubbles in the PDMS. The application of 3D printing has been exploited for the fabrication of custom mechanical parts and microfluidic devices[11,12]. These advancements aid in sample preparation seen in the recent fabrication of silica gel patterns for chromatography[13] and solid-phase extraction[14,15], which can be used for sample enrichment[2,16] for further analysis.

This project aims to turn 3D printing into a different area of application, 3D printed optical components integrated into biosensors, specifically fabricating quality optical components that can substitute existing optical components in current experimental setups, such as prisms. The direct 3D printing of prisms allows for facile fabrication of custom-designed optical components with a notably high-quality surface for bio-sensing[4,17]. While this stereolithography technique does fabricate prisms with variable surface roughness, simple benchtop sanding procedures can generate a surface amenable to high precision optical techniques. Our previous work applied a thin film of gold to study surface for surface plasmon resonance performance compared against commercial prisms, in this work we focus on fabricating a biosensor without the need for cleanroom technology to increase the accessibility of optical biosensor to a larger community. The new 3D printed prism utilizes in-situ nanoparticle growth[18] to fabricate a local surface plasmon resonance responsive surface to carryout bio-sensing of proteins. Our group has recently been working with 3D printed prisms and studying their ability to mimic glass prisms to become disposable prims substrates for surface plasmon resonance (SPR) studies[4]. The 3d printed prisms coated in a thin gold film allows covalent binding to occur directly on the prism face. This removes the needs for matching fluids, which would be normally applied to transition the gap between the prism and a functionalized glass slide to retain proper optical configurations. This direct modification of the prisms will decrease the noise and variation from set up to set up, which will affect the reproducibility of both a thin gold film and a layer of gold nanoparticles for SPR and localized SPR (LSPR) respectively.

Localized surface plasmon resonance (LSPR) occurs when the excitation of the electrons on the dielectric interface of the metal nanoparticle is localized around the metal nanoparticle due to the size of the nanoparticle (see Chapter 1 for a detailed explanation of LSPR). The excitation can be induced using a photon guided through a prism. The LSPR is extremely sensitive to minor changes in the refractive index surrounding the nanoparticles. This allows the detection of changes in bulk refractive index and binding interaction that alter the localized refractive index. Protein binding interaction and changes on the nanoparticle surface can be observed through monitoring either the sensing layer absorption or reflectivity spectrum[19,20]. Shifts in the wavelength where these peaks occur can correlate to a direct shift in either the bulk refractive index or binding events that occur on the surface[20–22]. Traditionally LSPR studies are conducted with a homogenous solution of gold nanoparticles and utilize UV-VIS to track the changes to the LSPR peak of the gold nanoparticle in solution[23–26]. This method is very sensitive to the nM range[27] but prone to the aggregation of nanoparticles interfering with results. LSPR on substrate surfaces mitigates the aggregation issue using a homogenous solution of nanoparticles adhered to a substrate. This can greatly improve sensitivity compared to a polydisperse nanoparticle solution and slightly rough surface of 3D printed prism[28,29].

Table 4.1 DNA Oligonucleotides Sequences.

Oligomer	Sequence
T20-SH	5′−T20−(CH2)3−SH−3′
Biotin-T20-SH	5′−biotin−NH2−(CH2)2O(CH2)2−PO4−T20−(CH2)3− SH−3’

4.2 Experimental Design.

Materials. Polydopamine, Trizma hydrochloride (HCl), gold (III) chloride trihydrate ($AuCL_3$), and Streptavidin were obtained from Sigma Aldrich (St. Louis, MO). Clear Resin v2 was purchased from Formlab[30] (Somerville, MA). All-Purpose polishing blocks, Blue and Brown, were purchased from Enkay Polishing System (Edgewood, New York). Functionalized oligonucleotides **(Table 4.1)** were obtained from Integrated DNA Technologies (San Diego, CA).

Instrumentation. Sandpaper of 100, 400, and 600 grit were used to smooth the prism surface. One speed polishing wheel from Central Machinery was used to buffer the prism surface to increase optical clarity. 3D printed prisms were mass-produced by a Form2 3D printer from FormLab2(Somerville, MA). Absorbance spectra were collected using a USB 2000+ UV-Vis spectrometer with an HL2000 Tungsten-Halogen light source guided through 200 µm optical fibers (Ocean Optics, Dunedin, FL). FT-IR analysis was performed on a Nicolet 6700 spectrometer (Thermo Scientific, Rockville, IL), and ellipsometry was performed on a UVISEL M200 (Horiba Jobin Yvon, France). Scanning electron microscopy (SEM) was conducted on FEI NNS450 SEM (Hillsboro, OR) in CFAMM at UC Riverside. Atomic force microscopy was conducted on a Veeco Dimension 5000 (Santa Barbara, CA) under tapping mode at a scan rate of 1 Hz. Prisms parameters were designed in SketchUp: 3D Design Software from Trimble (Sunnyvale, CA). Preform from FormLabs (Somerville, MA) was used to upload the STL file to the Form2.

Fabrication of optical 3D printed prisms. The dove prism dimension was drafted in SketchUP software and exported to Preform to load object file ono the Form2 3D printer. Multiple prisms can be fabricated in a single print job with Formlab's Clear Resin v2 at 100nm resolution for the z-direction. The 3D-printed prisms were carefully removed from the build-stage and rinsed with isopropanol. These prisms were transferred to a UV-oven to cure any remaining resin for 1 hour at 405nm wavelength. The resulting cured prisms are opaque and require post-processing to achieve adequate optical properties for optical sensor development. The opaque prisms are hand sanded with 100 grit sandpaper for 30 seconds followed by an additional second 30 seconds sanding using 400 grit sandpaper to minimize the ridges created from layer by layer fabrication technique of 3D-printing. The sanded prism is subjected to two rounds of buffer treatment to increase optical clarity so that light can pass and reflect through a prism for LSPR detection[31]. The process can be seen in (**Figure 4.1)**. The surface of the finished 3D printed prism was characterized by AFM.

In-situ growth of gold nanoparticle on 3D printed prism. The 3D printed prism requires a coating of polydopamine to initiate and catalyze the in-situ growth of gold nanoparticles. A solution of 2mg/mL polydopamine in a Trizma-HCl buffer was incubated on the prism surface for 18 hours in a moisturized environment. The prism is thoroughly rinsed with deionized water and dried with nitrogen. This polydopamine coated surface is then incubated with a gold chloride solution for 24 hours to growth nanoparticles on the surface. After the nanoparticles' growth phase is complete, the prism is again thoroughly rinsed with deionized water and dried with nitrogen gas. The dove prisms are stored in a dried environment for later usage. High-resolution SEM was used to characterize the nanoparticle on the prism surface **(Figure 4.2)**. A simple salt calibration was used to test the LSPR sensitivity of the sensor surface **(Figure 4.3)**.

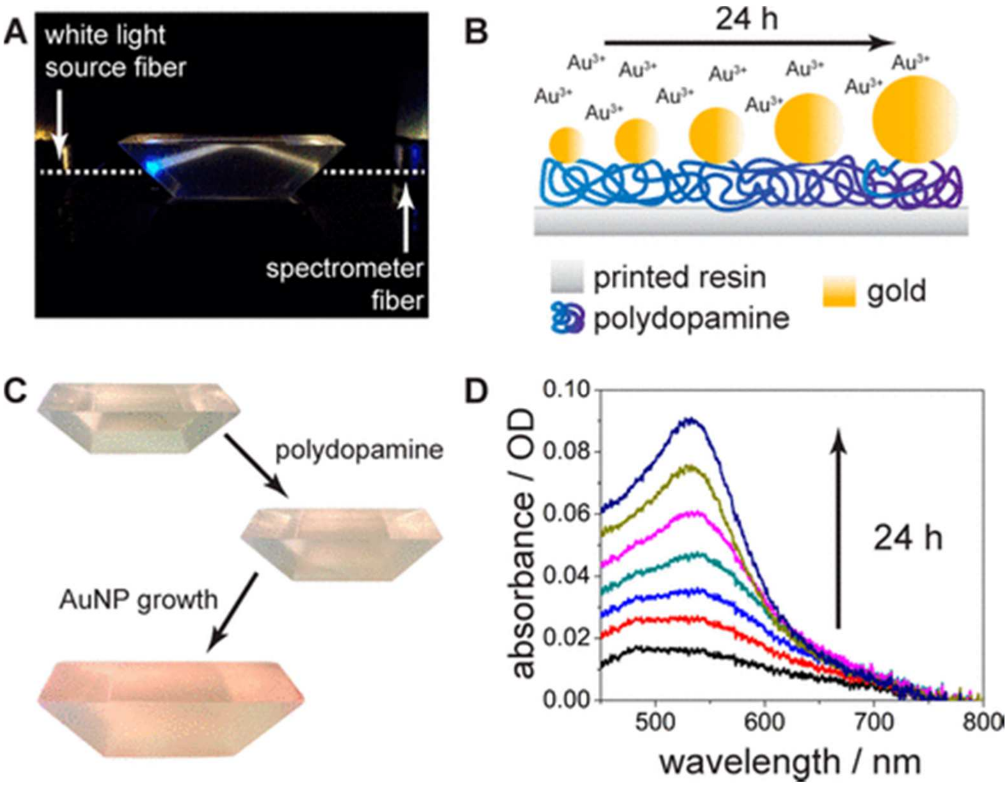

Figure 4.1 Dove prism fabrication. **(A)** Absorbance setup with dove prism, with total internal reflection of the light path depicted. **(B)** Polydopamine-mediated nanoparticle growth schematic. **(C)** Photographs of dove prisms during various stages of nanoparticle functionalization. **(D)** Absorbance spectra of nanoparticle growth on the polydopamine functionalized dove prism surface over a 24 h period. Reprinted from Ref#[4]

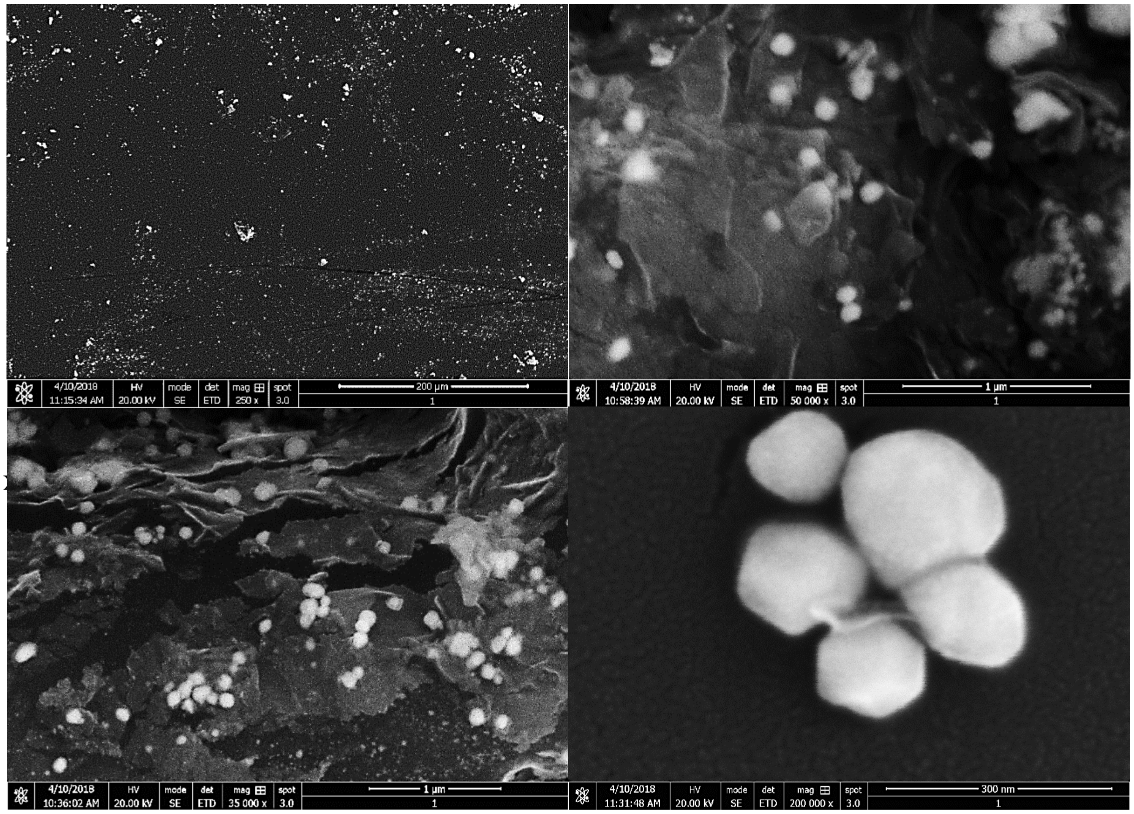

Figure 4.2 Characterization of the surface via SEM. **(A)** Density of gold nanoparticle catalytically grown via polydopamine on 3D printed prism surface is shown to distrusted across the surface and not highly packed. **(B)** Polydopamine sheets coating the prism surface supporting and adhering the gold nanoparticles. **(C)** The catalytic growth of the gold nanoparticles promotes large aggregation and clusters formation of gold nanoparticles in diverse sizes across surface. **(D)** Close up of nanoparticle clusters shows that individual nanoparticle diameter varies from 10-100nm with average at 50nm and forms clusters with diameter spanning from 50-300nm.

Surface Bindings of Proteins onto 3D printed prisms. The binding scheme for this experiment centers around DNA oligomers. The gold nanoparticles on the prism are functionalized with 10nM DNA oligomers, Biotin-T20-SH, via thiol-gold chemistry to activate the surface for selective capture of streptavidin. A range of streptavidin concentrations was exposed to the surface and tested the prism for its selective sensitivity and detection. Gold nanoparticles fabricated with DNA oligomer coating of a 1:1 mixture of Biotin-T20-SH: T20-SH[24] was used as a secondary set of a gold nanoparticle for signal enhancement.

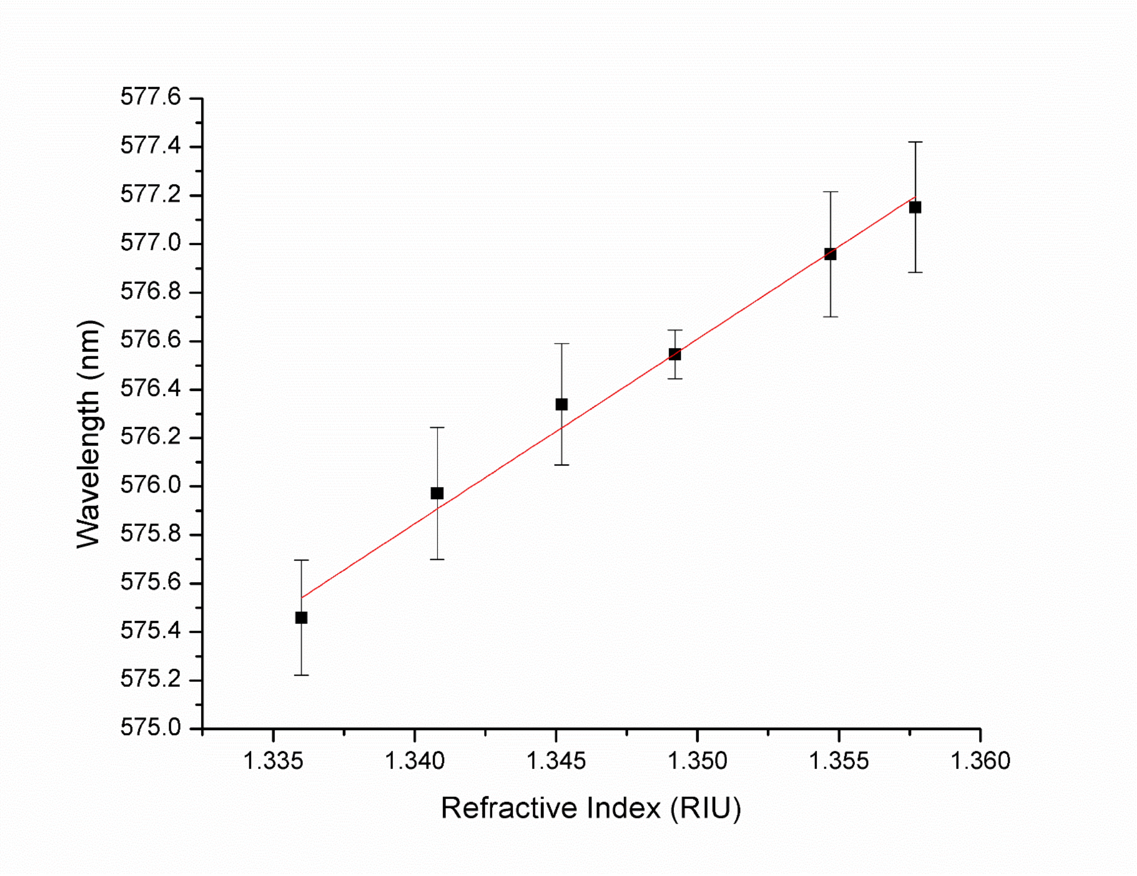

Figure 4.3 RI sensitivity of functionalized PDA-AuNP coated 3D printed prism.

4.3 Results and Discussion.

Characterization of 3D printed prism. The characterization of these 3D printed prisms as an alternative to commercial optical prisms was done in our group's previous work[4] and confirmed again in this project. The surface roughness is the main aspect of concern when comparing these 3D printed prototypes to commercial optical prisms. The surface roughness of the 3D printed prisms was characterized through atomic force microscopy (AFM) and had results an average surface roughness of 20nm and compared to data from commercial optical prisms with an average surface roughness of 2nm. The refractive index of the prism was measured through ellipsometry. The resin composition makeup was determined to resemble poly (methyl methacrylate) (PMMA) as the main polymer through FT-IR analysis. Our group's previous work investigated both the surface roughness of the sanding procedure and ellipsometry of the prism to find the wavelength-dependent refractive index and extinction coefficient of the printed resin. The results **(Figure 4.4)** show that the 3D printed prism is functionally comparable to conventional glass prisms with sensitivity to changes in refractive indexes.

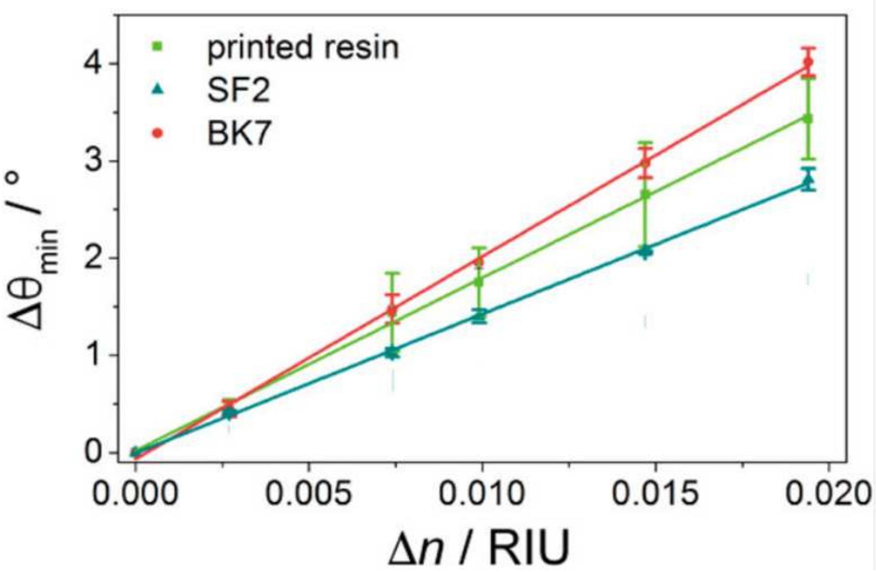

Figure 4.4 SPR Sensitivity comparison between 3D printed, SF2, and BK7 prisms.

Sensor Application of 3D printed prism. We have previously deposited both a thin gold film and a layer of gold nanoparticles onto the 3D printed prism as an integrated sensor prism as proof of concept for SPR and LSPR, respectively. This work continues the project for LSPR sensing with the in-situ growth of gold nanoparticle as the integrated sensor layer of these 3D printed prisms as a novel detection platform. Initially, 50nm gold nanoparticles were synthesized and incubated onto the prism surface. Nanoparticles will not naturally adhere to the PMMA surface of the 3D printed. These nanoparticles rinsed off randomly during experimentation, causing large unexpected changes in the signal observed.

Since gold nanoparticles do not naturally adhere to the polymer of the 3D printed prisms, another method was used to create an LSPR responsive surface. The in-situ growth of gold nanoparticle catalyzed by polydopamine was adapted from literature[32]. A polydopamine (PDA) in Trizma-HCl buffer is incubated on the surface of the 3D printed prism to form a coated layer of self-polymerizing PDA. This PDA layer serves as both an adhesive and a catalyst for in situ growth of gold nanoparticle from gold chloride solution incubated on top of the PDA coating of the prism to form gold nanoparticles on the surface of the prism for LSPR sensing[18]. These gold nanoparticles can be further functionalized to capture specific molecules using capture ligands, for example, antibodies or aptamers.

High-resolution SEM images **(Figure 4.2)** showed that the nanoparticles have varying diameters between 50nm to 200nm and form large clusters throughout the surface of the 3D printed prism. The lack of surface uniformity increases the variation of sensitivity due to the heterogeneous distribution of nanoparticle size[33,34] and surface fabrication reproducibility from the random aggregation pattern of the gold nanoparticles. Results from testing bulk sensitivity **(Figure 4.3)** demonstrate that the prism is LSPR sensitive to changes in the refractive index and has a linear correlation, R^2=0.986.

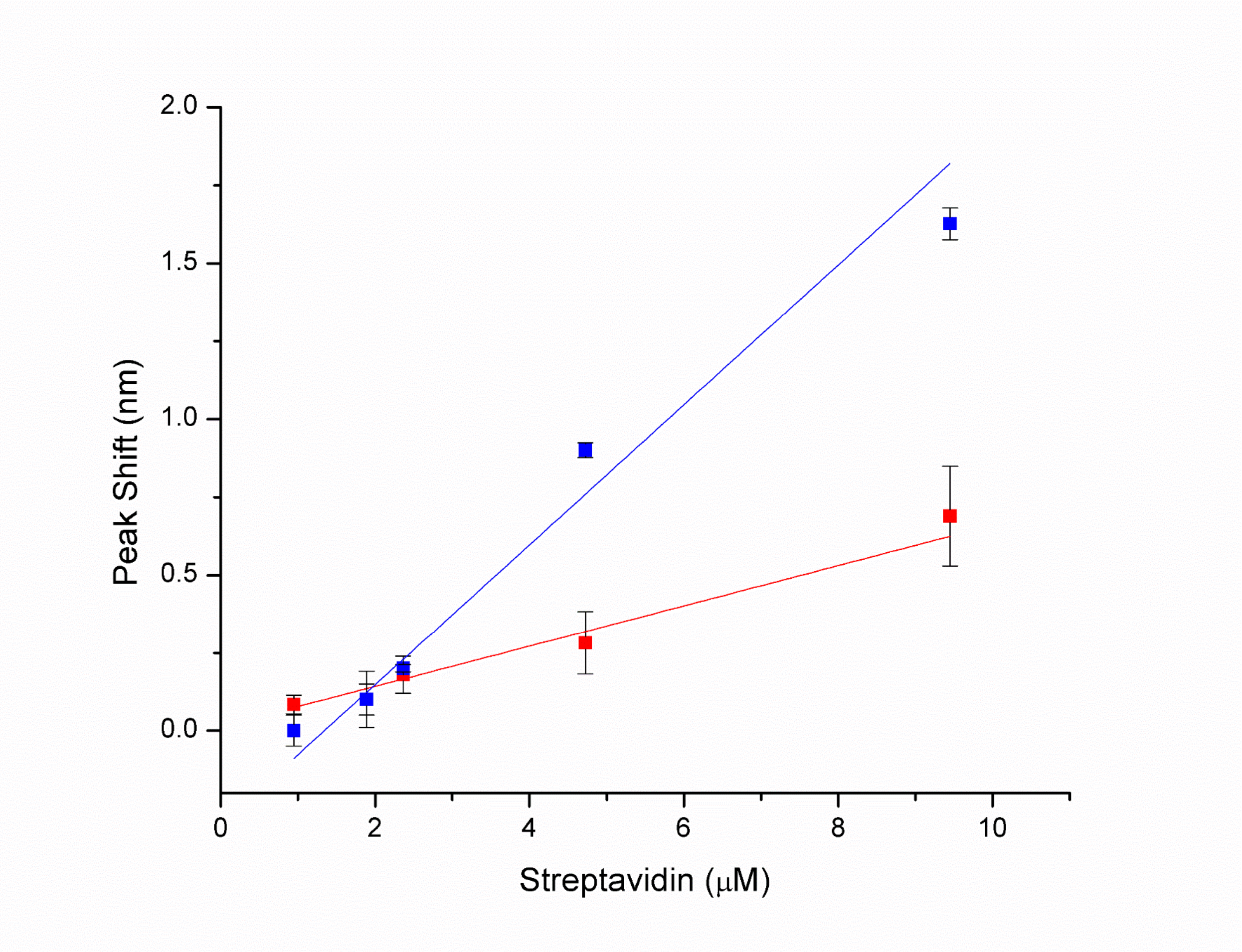

Figure 4.5 Streptavidin sensitivity of 3D Printed Prisms surface created with. (●) 0.5mM $AuCl_3$, (●) 1.5mM $AuCl_3$.

Surface Binding Sensitivity. Optimization of the concentration for initial gold (III) chloride was tested to examine the effects on gold nanoparticle distribution and resulting LSPR sensitivity. Two concentrations were examined, 0.5 and 1.5mM of AuCl3 **(Figure 4.5)**. At the higher concentration, the nanoparticle did increase in size and density on the prism surface compared to the nanoparticles formed at the lower concentration, resulting in an increase in the sensor surface area. The surface fabricated from the 1.5mM AuCl3 performed better as it had higher signal observed from protein binding than the surface formed from the 0.5mM AuCl3. An even higher concentration of 5mM AuCl3 was examined.

While the nanoparticles did form, the resulting layer was not sensitive to changes in the LSPR peak as the absorption peak was extremely broad. Thus, the concentration of 1.5mM AuCl3 was used in the rest of the experiment. The sensitivity of surface binding events on the localized surfaces of these gold nanoparticles coated prisms is tested with the model binding pair biotin and streptavidin. Concentrations of 1-10 μM streptavidin were exposed to the surface and observed the resulting linear, R^2=0.9-0.93, LSPR shift due to these binding events on the surfaces **(Figure 4.4)**. The sensor can detect binding response at a minimum of 0.668 μM of streptavidin and can accurately quantify at 2.228 μM of streptavidin. The variation in signal response of the protein binding is due to the non-homogenous structures of the self-assembled nanoparticle on the surface.

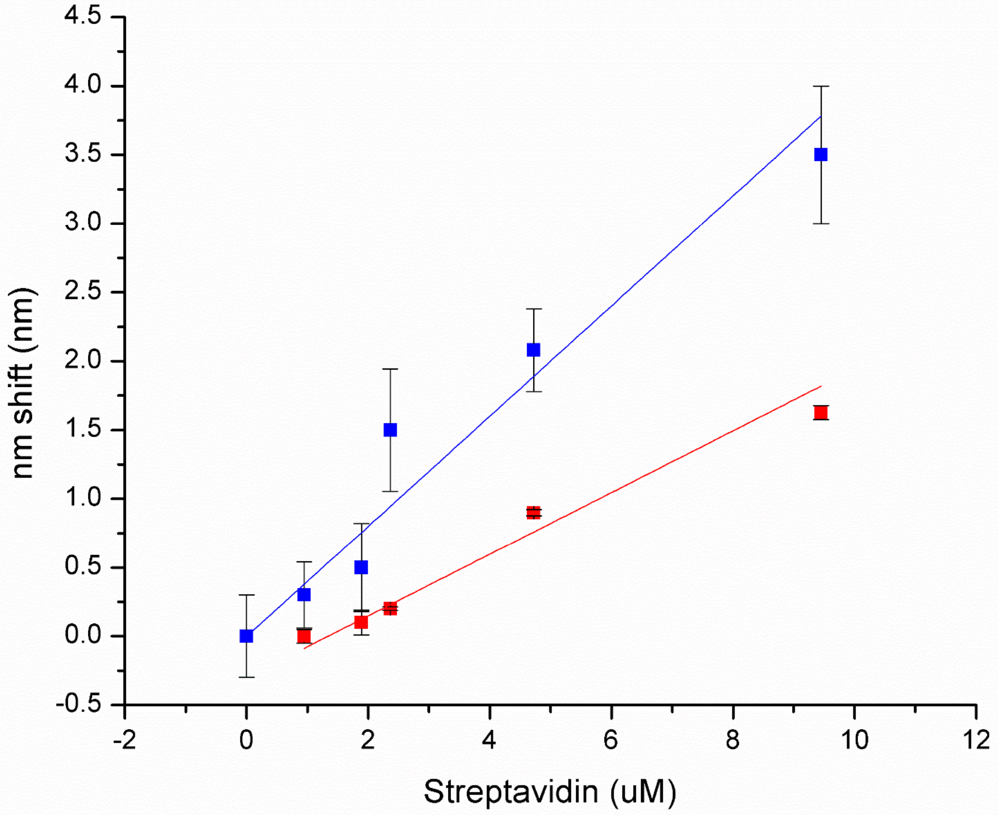

Figure 4.6 Secondary AuNP for signal enhancement *(•)* increases from protein bound to the surface *(•)*.

Secondary gold nanoparticles were utilized to increase signals from protein binding, allow the sensor to attempt to enhance sensor sensitivity at lower concentrations **(Figure 4.6)**. While the signal resolution at a lower concentration was enhanced by two-fold through the secondary nanoparticles, the sensor performance did drop with the limit of detection and quantification at 1.798 µM and 5.994 µM of streptavidin respectively due to nonspecific binding. The nanoparticle signal enhancement utilized 2nm gold nanoparticles coated with a 1:1 mixture of biotinylated and non-biotinylated DNA oligomer with a thiol group to facilitate binding between the protein and the secondary gold nanoparticle to induce a larger LSPR shift due to increase mass loaded on the analyte surface. There is a nonspecific binding interaction between the gold nanoparticles and the polydopamine surface, which hinders the lower limit of detection.

4.4 Conclusion.

Traditionally, the sensor chip is fabricated from a plasmonic material of a thin gold film deposited on a glass substrate. Careful handling of matching fluid is required to interface the glass substrate and the optical prism to allow light to travel correctly. While it is possible to simplify experimental setup by depositing a thin gold film directly onto the prism surface, most sensing schemes utilize covalent binding to the gold surface, rendering the prism non-reusable. This study emphasizes the integration of a thin layer of gold nanoparticle on the 3D printed prism for simple, convenient, and disposable integrated sensor component for the field of site usage

The simplicity of this prism fabrication does not require special tools or facilities to generate an LSPR responsive surface. The interface has a limit of detection and a limit of quantification of 0.668 μM and 2.228 μM of streptavidin, respectively. Secondary gold nanoparticles were successfully employed as a signal enhancement to differentiate signals at the lower concentration range of 0.5-3 μM range. However, this also decreases the sensor sensitivity as the limit of detection and limit of quantification shifted to 1.798 μM and 5.994 µM of streptavidin, respectively. This decrease in the sensor performance can be attributed to the nonspecific binding of the secondary gold nanoparticle to the sensing surface.

While the sensor performs in the µM range of streptavidin, the ideal concentration target of pM – nM range has yet to be achieved with this platform. The sensing layer would require further optimization to achieve higher sensitivity. Primarily focusing on optimizing the nanoparticle layer in multiple parameters: 1) size dispersion, 2) density, and 3) packing/arrangement on the prism face is important in controlling the LSPR responsive absorption peak. Ideally, a monolayer of densely packed monodispersed gold nanoparticle would result in a very tight absorption peak that would be extremely sensitive to changes and able to detect extremely low concentrations of targeted analytes.

In summary, these 3D printed prisms are easily mass-produced at a low cost and can be used as disposable units. The application of a 3D printed prism as an integrated optical sensor component was investigated in this project demonstrated proof of concepts for fabricating 3D printed prisms with parameters functionally comparable commercially available optical prisms. While there is still room for improvement for the 3d printed prisms to fully match the parameter of traditional prisms, the current parameters are suitable to allow integration of a thin layer of gold film or gold nanoparticle for SPR and LSPR detection, respectively. These 3D printed prisms can be used in substitution of commercially available optical prisms to facilitate the direct integration of a sensing layer onto the prism face.

References:

(1) Ligon, S. C.; Liska, R.; Stampfl, J.; Gurr, M.; Mülhaupt, R. Polymers for 3D Printing and Customized Additive Manufacturing. *Chem. Rev.* **2017**, *117* (15), 10212–10290.

(2) Pi, H.; Tong, J.; Bian, C.; Xia, S. 3D Printed Micro / Nanofluidic Preconcentrator for Charged Sample Based on Ion Concentration Polarization. *J. Micromech. Microeng* **2017**, *27*, 55008(1-7).

(3) Gross, B.; Lockwood, S. Y.; Spence, D. M. Recent Advances in Analytical Chemistry by 3D Printing. *Anal. Chem.* **2017**, No. 89, 57–70.

(4) Hinman, S. S.; Mckeating, K. S.; Cheng, Q. Plasmonic Sensing with 3D Printed Optics. *Anal. Chem.* **2017**, No. 89, 12626–12630.

(5) Bhattacharjee, N.; Urrios, A.; Kang, S.; Folch, A. Lab on a Chip The Upcoming 3D-Printing Revolution in Microfluidics. *Lab Chip* **2016**, *16*, 1720–1742.

(6) Dommati, H.; Ray, S.; Wang, J.; Chen, S. 3D Printing Technique for Ceramic Membrane Fabrication for Water Puri Fi Cation. **2019**, 16869–16883.

(7) Ngo, T. D.; Kashani, A.; Imbalzano, G.; Nguyen, K. T. Q.; Hui, D. Additive Manufacturing (3D Printing): A Review of Materials , Methods , Applications and Challenges. *Compos. Part B* **2018**, *143* (December 2017), 172–196.

(8) Wang, X.; Jiang, M.; Zhou, Z.; Gou, J.; Hui, D. 3D Printing of Polymer Matrix Composites : A Review and Prospective. *Compos. Part B* **2017**, *110*, 442–458.

(9) Meng, C.; Ho, B.; Mishra, A.; Hu, K.; An, J.; Kim, Y.; Yoon, Y. Femtosecond-Laser-Based 3D Printing for Tissue Engineering and Cell Biology Applications. *ACS Biomater. Sci. Eng.* **2017**, No. 3, 2198–2214.

(10) Jose, R. R.; Brown, J. E.; Polido, K. E.; Omenetto, F. G.; Kaplan, D. L. Polyol-Silk Bioink Formulations as Two-Part Room-Temperature Curable Materials for 3D Printing. *ACS Biomater. Sci. Eng.* **2015**, *1* (9), 780–788.

(11) Kataoka, E. M.; Murer, R. C.; Santos, J. M.; Carvalho, M.; Eberlin, M. N.; Augusto, F.; Poppi, R. J.; Gobbi, A. L.; Hantao, L. W. Simple, Expendable, 3D-Printed Micro Fl Uidic Systems for Sample Preparation of Petroleum. *Anal. Chem.* **2017**, No. 89, 3460–3467.

(12) Anciaux, S. K.; Geiger, M.; Bowser, M. T. 3D Printed Micro Free-Flow Electrophoresis Device. *Anal. Chem.* **2016**, No. 88, 7675–7682.

(13) Fichou, D.; Morlock, G. E. Open-Source-Based 3D Printing of Thin Silica Gel

Layers in Planar Chromatography. *Anal. Chem.* **2017**, No. 89, 2116–2122.

(14) Calderilla, C.; Maya, F.; Cerdà, V.; Leal, L. O. 3D Printed Device Including Disk-Based Solid-Phase Extraction for the Automated Speciation of Iron Using the Multisyringe Flow Injection Analysis Technique. *Talanta* **2017**, *175* (April), 463–469.

(15) De Middeleer, G.; Dubruel, P.; De Saeger, S. Molecularly Imprinted Polymers Immobilized on 3D Printed Scaffolds as Novel Solid Phase Extraction Sorbent for Metergoline. *Anal. Chim. Acta* **2017**, *986*, 57–70.

(16) Su, C. K.; Peng, P. J.; Sun, Y. C. Fully 3D-Printed Preconcentrator for Selective Extraction of Trace Elements in Seawater. *Anal. Chem.* **2015**, *87* (13), 6945–6950.

(17) Hernandez-Serrano, A. I.; Castro-Camus, E. Quasi-Wollaston-Prism for Terahertz Frequencies Fabricated by 3D Printing. *J. Infrared, Millimeter, Terahertz Waves* **2017**, *38* (5), 567–573.

(18) Sureshkumar, M.; Lee, P.; Lee, C. Stepwise Assembly of Multimetallic Nanoparticles via Self-Polymerized Polydopamine. *J. Mater. Chem.* **2011**, No. 21, 12316–12320.

(19) Willets, K. A.; Duyne, R. P. Van. Localized Surface Plasmon Resonance Spectroscopy and Sensing. *Annu. Rev. Phys. Chem.* **2007**, No. 58, 267–297.

(20) Hall, W. P.; Ngatia, S. N.; Duyne, R. P. Van. LSPR Biosensor Signal Enhancement Using Nanoparticle - Antibody Conjugates. *J. Phys. Chem. C* **2011**, No. 115, 1410–1414.

(21) Masson, J. F. Surface Plasmon Resonance Clinical Biosensors for Medical Diagnostics. *ACS Sensors* **2017**, *2* (1), 16–30.

(22) King, N. S.; Liu, L.; Yang, X.; Cerjan, B.; Everitt, H. O.; Nordlander, P.; Halas, N. J. Fano Resonant Aluminum Nanoclusters for Plasmonic Colorimetric Sensing. *ACS Nano* **2015**, *9* (11), 10628–10636.

(23) Wu, Q.; Sun, Y.; Ma, P.; Zhang, D.; Li, S.; Wang, X.; Song, D. Gold Nanostar-Enhanced Surface Plasmon Resonance Biosensor Based on Carboxyl-Functionalized Graphene Oxide. *Anal. Chim. Acta* **2016**, *913*, 137–144.

(24) Hinman, S. S.; McKeating, K. S.; Cheng, Q. DNA Linkers and Diluents for Ultrastable Gold Nanoparticle Bioconjugates in Multiplexed Assay Development. *Anal. Chem.* **2017**, *89* (7), 4272–4279.

(25) Banti, S.; Borah, D.; Baruah, S.; Mohammed, W. S.; Dutta, J. Heavy Metal Ion

Sensing By Surface Plasmon Resonance on Gold Nanoparticles. *ADBU-Journal Eng. Technol.* **2014**, *1*, 2–6.

(26) Li, C.; Wu, C.; Zheng, J.; Lai, J.; Zhang, C.; Zhao, Y. LSPR Sensing of Molecular Biothiols Based on Noncoupled Gold Nanorods. *Langmuir* **2010**, *26* (11), 9130–9135.

(27) McKeating, K. S.; Couture, M.; Dinel, M.-P.; Garneau-Tsodikova, S.; Masson, J.-F. High Throughput LSPR and SERS Analysis of Aminoglycoside Antibiotics. *Analyst* **2016**, *141* (17), 5120–5126.

(28) Feng, B.; Zhu, R.; Xu, S.; Chen, Y.; Di, J. A Sensitive LSPR Sensor Based on Glutathione-Functionalized Gold Nanoparticles on a Substrate for the Detection of Pb^{2+}Ions. *RSC Adv.* **2018**, *8* (8), 4049–4056.

(29) Li, X.; Jiang, L.; Zhan, Q.; Qian, J.; He, S. Localized Surface Plasmon Resonance (LSPR) of Polyelectrolyte-Functionalized Gold-Nanoparticles for Bio-Sensing. *Colloids Surfaces A Physicochem. Eng. Asp.* **2009**, *332* (2–3), 172–179.

(30) Formlabs Inc. Safety Data Sheet. Clear: Photoreactive Resin for Form1, Form 1+, Form 2. **2016**, 1–8.

(31) Hinman, S. S.; McKeating, K. S.; Cheng, Q. Supporting Plasmonic Sensing with 3D Printed Optics. *Anal. Chem.* **2017**, *89* (23), 12626–12630.

(32) Heath, G. R.; Li, M.; Polignano, I. L.; Richens, J. L.; Catucci, G.; Shea, P. O.; Sadeghi, S. J.; Gilardi, G.; Butt, J. N.; Jeuken, L. J. C. Layer-by-Layer Assembly of Supported Lipid Bilayer Poly-L-Lysine Multilayers. *Biomacromolecules* **2016**, No. 17, 324–355.

(33) Lee, T. K.; Kwak, S. K. E Ff Ects of LSPR of Gold Nanospheres by Surface Vacancies and Protruding Tips. *J. Phys. Chem. C* **2014**, No. 118, 5881–5888.

(34) Zeng, S.; Yu, X.; Law, W. C.; Zhang, Y.; Hu, R.; Dinh, X. Q.; Ho, H. P.; Yong, K. T. Size Dependence of Au NP-Enhanced Surface Plasmon Resonance Based on Differential Phase Measurement. *Sensors Actuators, B Chem.* **2013**, *176* (January), 1128–1133.

Chapter 5: Investigation of a Biomimetic Double lipid bilayer membrane interface for protein-lipid interactions via SPR.

5.1 Introduction.

Humans increasingly synthesize new chemical compounds for new pharmaceutical drugs, consumer products, and various other advances in productions. These compounds can be directly toxic to humans, have synergistic effects with known toxins, or rarely, inhibit toxins. Exposure to these compounds has increased as more of these compounds make their way into the environment from direct exposure or improper disposal. Because of the potentially dire effects on human and environmental health, it has become crucial to detect trace exposure of these toxic compounds before any adverse effect begins. An understanding of the toxin's mechanism of action, specifically with respect to how the toxin interact with cell membranes, provides a basis for developing biosensors that can take advantage of initial binding interactions to detect compounds, even at low concentrations.

Toxicity studies are conducted on cell assays to examine onset of adverse effects and which systems are affected. Cell culturing is time consuming and may obtain conflicting results due to varying cellular responses. Biosensors provide an alternative for simple analysis of biological interaction on a reproducible model interface to obtain quick and reproducible results. Previous research into the development of biophysical sensors use a highly simplified experimental model of the plasma membrane as an interface for protein and small chemical analyte interaction on the membrane surface. These surfaces have been tailored for optimized assay reactions, minimalizing cellular biological interferences, increasing reproducibility and reliability of examining protein interactions[1–3]. These studies drafted various strategies to tailor their single lipid bilayer interface for optimized binding interactions to its target of interest through a range of fabrication methods. In early studies employing SPR for investigating lipid membrane systems, the hybrid lipid bilayer constructed from hydrophobic tails of phospholipids adsorb to a monolayer of alkane thiols has been exploited extensively. Tethered lipid bilayers have been developed to model cellular membrane system constructed from isolated lipid vesicles originating from either mammalian or bacterial cells to form bilayer facsimiles of their in vivo counterparts. Recently, solid-supported lipid bilayer system has been developed to study interactions on a fluid single lipid bilayer membrane interface.

Experimental models of single lipid bilayer system have been extensively studied on sensor system such as surface plasmon resonance (SPR) and quartz crystal microbalance (QCM). These works provided novel insights into biomolecular interactions on the cellular membrane in a computational model[4–7] or a simplified experimental system[1,8–10]. These interactions of membrane protein, antibodies, and small molecules elucidates new pathways that can be exploited for novel binding mechanism for specific targeting and discover new potential drug candidates that target these interactions. While applications of single bilayer membrane systems will continue examine all possible novel interactions, single bilayer are not the only lipid layer system that requires elucidating. Double bilayer systems are unique to the membranes of mitochondria, chloroplasts, and gram-negative bacteria. While theoretically model and cell assays exist to examine interactions at these interfaces, an experimental model capable of monitoring interactions on this mimicked surface will aid in uncovering mechanisms that occur on these interfaces with greater speed and reproducibility.

The principle and technique behind single lipid bilayer computational[7,11] and experimental models[10,12–14] serve as the foundations for the experimental models of double lipid bilayer system, an important field of interest as these unique membrane interfaces serve vital roles in the mitochondria, chloroplast, and the gram-negative bacteria[5,7,11]. Modeling these systems will improve understanding of protein interactions at this unique lipid interface. Early examples of computational and simple experimental model of the double lipid bilayer membrane system have been reported in literature. These models demonstrated partial success as these surfaces is only capable of mimicking partial aspects of the mitochondria or gram-negative bacteria with no sensing or monitoring binding interactions. Interactions at a single lipid bilayer may behave differently when it is placed in a double bilayer system. This project aims to rectify this and develop a double lipid bilayer system that mimics gram-negative bacteria cell walls and investigate binding interaction studies as a proof of concept for a novel sensor design that will aid in discovering novel compounds for potential drug application.

Computational[4,6,15] and experimental models[6,16–19] of these double lipid bilayer systems will aid in improving the understanding mechanism involved in these energy producing organelles and uncovering novel drug-membrane interactions of gram-negative bacteria[5,7,11]. Early works in literature demonstrates the fabrication of multi-layers lipid membrane systems utilizing an assortment of tethered supported lipid bilayer[10,12,14,20–23], electrostatic interaction between lipid layers[24,25], and DNA hybridization[26–28] to form multiple stacked lipid bilayers . Simple facsimile[6,18,19] of the double lipid membrane system have attempted lackluster characterization of interactions occurring on this interface. This project applies a double lipid bilayer system (**Figure 5.1**) formulated from two stacked and adherent lipid bilayers facilitated by charge interaction between negatively charged lipid headgroups and positively charged polymers of poly-L-lysine[24,25] for SPR applications to elicit better understanding of protein-lipid interactions.

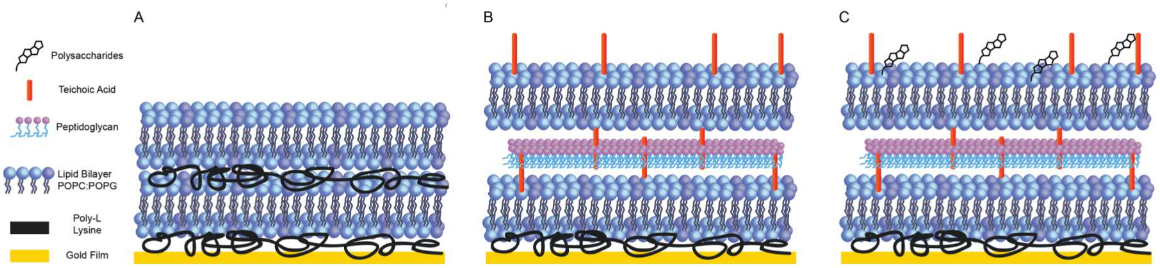

Figure 5.1 Double lipid model system for mimicking gram-negative bacteria cell walls begins with simple model **(A)** shown in this study and planned improvements to increase modelling accuracy by replacing PLL layer with peptidoglycans **(B)** and incorporating polysaccharides **(C)** to mimic bacteria recognition for potential drug interactions.

Surface plasmon resonance (SPR) has emerged as a robust technique employed in biosensor development for label free analysis of protein affinity, lipid specificity, and signal amplification through a diverse set of binding schemes.[8,12,13,22,29] Due to principles behind the resonance conditions explained in Chapter 1, SPR is very sensitive to changes on or near the sensing surface of a thin gold film. Many works have taken advantage of this to conduct analysis of small analyte binding through specific target binding of its specific ligands immobilized on gold surfaces to test protein binding affinity and kinetics. Other applications of SPR have aimed for the development of novel binding mechanisms to aid in complex binding assays and signal enhancement techniques to expand targetable analytes and amplify response signals from low concentration of analyte binding, respectively. Previously, SPR has been utilized to study single lipid membrane interactions using hybrid lipid bilayer on Biacore HPA hydrophobic hips, protein tethered membranes, and solid-supported lipid membranes for modeling and analyte binding analysis. While experimental model of single lipid bilayers systems has been extensively studied, experimental models of double lipid bilayers has sparked interest. The development of experimental models of double lipid bilayer systems can further elicit better understand of interactions at the surfaces of mitochondria, chloroplasts, and gram-negative bacteria. Thusly, this project aims do develop a SPR biosensor pairing biological interactions with measurable responses that can facilitate chemical characterization, toxin interaction, and dose-responses at the novel double lipid bilayer membrane interface for exploring primary molecular recognition events that are critical in understanding onset of adverse effects in organisms.

The step by step assembly of this complex double lipid bilayer system was monitored in real time using a BiacoreX unit and SPR analysis to confirm proper formation of the lipid membrane model. The model was probed with chemical and protein interactions to examined if the lipid layers properly formed into lipid bilayers through analysis of SPR response exhibited by the model interface. It is important to characterize the formation of the lipid bilayer to ensure proper formation of desired model system as improper formation will flaw the model design and application. The layer by layer assembly of double lipid bilayer system form from two full lipid bilayers adhered by charge interactions of PLL. Beside fabricating a double lipid bilayer membrane model, application of the membrane model for sensing binding interaction is also examined. For protein binding interactions, two model protein binding systems: Streptavidin to Biotin and Cholera Toxin to Ganglioside-monosialic acid (GM1), were used to study SPR responses at the single and double lipid bilayer interfaces. Additionally this model was used to examine Streptolysin O (SLO), a cholesterol-dependent pore forming toxin, incorporation into the membrane to facilitate self-assembly of large pore structures[24,30,31] and monitored its influence on protein interactions in this novel double lipid bilayer system. This novel double lipid bilayer system was examined a novel membrane model mimicking bacteria cell walls and applied as sensor interface which exhibited high sensitivity to cholera toxin down to nanogram per milliliter range. The utilization of SLO introduces the concept of biomimetic size selective filter via streptolysin O pores in the outer lipid membrane.

5.2 Experimental Details.

Materials and reagents. 16:0-18:1 PC (POPC) 1-palmitoyl-2-oleoyl-glycero-3-phosphocholine, 16:0-18:1 (PG) 1-palmitoyl-2-oleoyl-sn-glycero-3-phospho-(1'-rac-glycerol), 16:0-18:1 (PE) 1-palmitoyl-2-oleoyl-sn-glycero-3-phosphoethanolamine, 18:1

(PE-PEG5000)1,2-dioleoyl-sn-glycero-3-phosphoethanolamine-N-[methoxy (polyethylene glycol)-5000], 18:1 (Biotinyl PE) 1,2-dioleoyl-sn-glycero-3-phosphoethanolamine-N-(biotinyl) and 1-palmitoyl-2-6-[(7-nitro 2-1,3-benzoxadiazol-4-yl)amino]hexanoyl-sn-glycero-3-phosphocholine (NBD-PC) were obtained from Avanti Polar Lipids, Inc. (Alabaster, AL). Monosialoganglioside GM1 (NH4+salt) was obtained from Matreya LLC. (State College, PA). Cholesterol, Poly-L-lysine (PLL) hydrobromide (mol wt. 150,000-300,000), Cholera toxin (CT) from Vibrio cholerae, Streptolysin O (SLO) from Streptococcus pyogenes, Trypsin, Horseradish Peroxidase, 3,3',5,5'-Tetramethylbenzidine (TMB), Aniline, 1-Ethyl-3-(3-dimethylaminopropyl)carbodiimide (EDC), N-Hydroxysuccinimide (NHS) were obtained from Sigma-Aldrich (St. Louis, MO) . Streptavidin Pierce™ and Bk-7 microscope cover slips were obtained from Thermo Fisher Scientific (Waltham, MA). Chromium and gold used for electron-beam evaporation were acquired as pellets of 99.99% purity from Kurt J. Lesker (Jefferson Hills, PA).

Instrumentation. A BiacoreX (GE Healthcare Life Sciences, Chicago, IL) with a light source (λ_{max} ~ 800 nm)[32] was used for all real-time binding measurements. SPR Chip carriers protype were 3D printed with Formlab2 (Somerville, MA) and mass produced on Object 3D Pro (Eden Prairie, MN.) SPR experiments were conducted at ambient temperature (~23 °C), with 1×PBS (10 mM Na2HPO4, 1.8 mM KH2PO4, 137 mM NaCl, 2.7 mM KCl, pH 7.4) used as the running buffer set to a flow rate of 20 µL min^{-1}. Fluorescence microscopy was carried out on an inverted Leica TCS SP5 II (Leica

Microsystems, Buffalo Point, IL) using the 488 nm Argon laser line (for NBD), in conjunction with a 40× objective and Leica HyD hybrid detector.

SPR Gold Chip Fabrication. BK-7 glass microscope coverslips (18mm x18mm) were first cleaned using a boiling piranha solution (3:1 v/v H2SO4 and 30% H2O2) for 30 min, followed by rinsing with deionized water and drying under compressed nitrogen. 2 nm of chromium (0.5 Å s-1), followed by 46 nm of gold (1.0 Å s-1) were then deposited using electron-beam evaporation (Temescal, Berkeley, CA) at 5.5×10-6 Torr in a Class 1000 cleanroom facility (UCR Center for Nanoscale Science & Engineering). The gold coated coverslips were split in half (18mm x 9mm) using a glass cutter and cleaned with isopropanol and ultrapure water before mounting via Gorilla Super Glue (Cincinnati, OH)on painted 3D printed Biacore chip carriers from Object 3D Pro (Eden Prairie, MN) that were reversed engineered to be operate on the BiacoreX.

Table 5.1 Lipid vesicle composition used in this study for layer by layer assembly and optimization of double lipid bilayer system and protein binding interactions.

Lipid	**Lipid Vesicle composition**
POPC	100% POPC
Pegulated Vesicles	99.5% POPC 0.5% PE-PEG5000
POPC: POPG	1:1 (50% POPC 50% POPG) 3:1 (75% POPC 25% POPG)
3:1 POPC: POPG w/ (GM1 or Biotin)	72.5% POPC, 22.5% POPG, 5% GM1 72.5% POPC 22.5% POPG] 5% Biotinyl-PE
3:1POPC: POPG w/ Cholesterol	37.5% POPC 12.5% POPG 50% Cholesterol 67.5% POPC 22.5% POPG 10% Cholesterol

Vesicle Preparation. Appropriate amounts of POPC, PE, Biotinyl-PE, PE-PEG5000, PG, NBD-PC, Cholesterol, and/or GM1 from stock solution in chloroform were dried in a glass vial under nitrogen to form a thin lipid film of varying ratios ***(Table 5.1)***. The vial was stored in a vacuum desiccator for at least two hours to aid in the removal any residual solvent. These dried lipids films were resuspended in 1×PBS to reconstitute a lipid concentration of 1.0 mg mL^{-1}. Vigorous vortexing was required to desorb all remnants of the lipid film from the vial wall, resulting in a partially cloudy solution. This solution was then bath sonicated for a minimum of thirty minutes to obtain a clear solution, indicating the large lipid clouts had broken down into smaller vesicles. The vesicle solution was then extruded repeatedly through a lipid extruder kit equipped with a polycarbonate filter (100nm) to produce small unilamellar vesicles (SUVs) of uniform size. All prepared vesicle solutions were used within a week and stored at 4 °C. Vesicles with a 1:1 molar ratio of lipid content to cholesterol were specially prepared to from Streptolysin O incubated vesicles. Incubation of a final concentration of 10 hemolytic units (HU) Streptolysin O into the cholesterol filled vesicles was done thirty minutes prior to injection onto the BiacoreX unit.

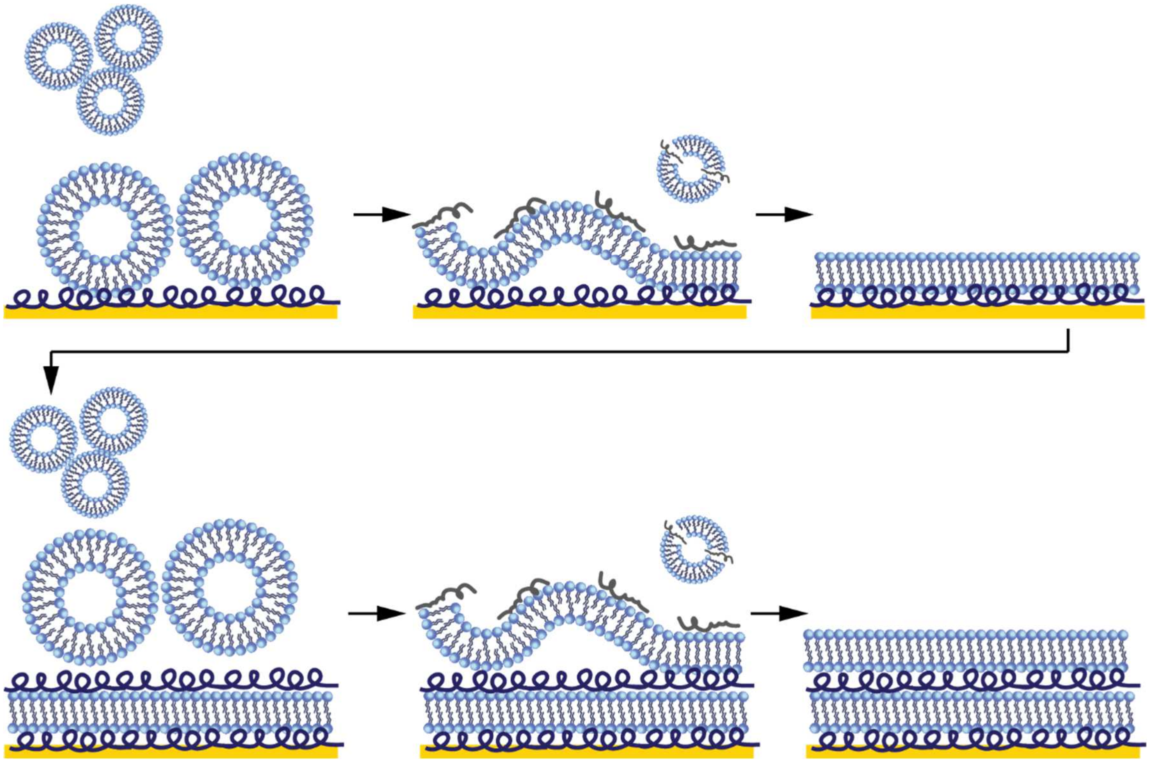

Figure 5.2 Fabrication of double lipid bilayer system through layer by layer assembly of poly-L-Lysine (PLL) and 3:1 POPC: POPG lipid vesicles with additional PEG5000 incubation to induce vesicle rupture to ensure lipid bilayer formation.

Double Lipid Bilayer Formation. All incubation and rinsing steps were conducted and monitored on the BiacoreX with intervals at thirty minutes to allow injected compounds time to interact to the surface and remove any unbound compounds from the system to acquire signal corresponding directly to surface binding interaction and minimizing signal from nonspecific binding. The gold chip sensor is first incubated with 0.01mg/mL poly-L-lysine (mw 150kda-300kda) to form a monolayer of PLL on the surface. Initial lipid bilayer solution was then injected and incubation to assemble a base layer of lipids on the PLL coated gold surface. The self-assembly process of the lipid bilayer requires assistance from an incubation of a 10% Peg5000 solution to ensure full vesicle rupture to confirm self-assembly of bilayer on the PLL monolayer. Another 0.01mg/mL PLL solution was incubated to initiate layer by layer stacking of the proceeding lipid bilayer. The second solution of vesicles is injected, forming the second bilayer, with another sequential incubation of 10% Peg5000 to ensure lipid bilayer formation on the second PLL monolayer. This fully formed double lipid bilayer platform (**Figure 5.2**) mimics double bilayer systems found in nature and can be used in applications to improve understanding of lipid-protein interactions at these specific biological interfaces.

5.3 Results and Discussion.

Traditional studies utilizing a single lipid bilayer on a Biacore instrument require branded hydrophobic HPA chips which uses a self-assemble monolayer of alkane-thiols to facilitate a formation of a hybrid lipid bilayer. This project employs a BiacoreX instrument and custom 3D printed Biacore chip carriers paired with bare gold sensor surfaces to monitor the fabrication of our single and double lipid bilayer system and to measure protein binding response via SPR. Our lab has previously shown that lipid vesicles readily self-assemble into lipid bilayers on silicated gold surfaces[13,29,33–35] due to the hydrophilic interaction between the silica and the head groups of the lipid vesicles. Due to the hydrophobicity of a bare gold surface, POPC lipid vesicles will not readily adsorb to the surface and self-assemble into a lipid bilayer. Tethered lipid bilayers have been studied as a method to attach lipid bilayers; but covalently tethering can decrease the fluid mobility of the assembled bilayer. To retain lipid fluidity of a self-assemble lipid bilayer on bare gold surfaces, we first proposed to harness POPC/PE-PEG5000 lipids to formulate polymer supported lipid bilayers to facilitate vesicles adsorption and lipid bilayer assembly on the gold surface. Upon examination on the BiacoreX instrument, the observed response of the PEG-PE bilayer resulted in less than 200 Resonance Units (RU) which indicates little to no adsorption and self-assembly of the into a lipid bilayer compared to non-pegylated lipid vesicles which achieved a signal response of approximately 4000 RU.

Silicated gold sensor chips fabricated by depositing a thin layer of silica (2-4nm) were initially employed to facilitate lipid vesicles adsorption, but initial testing of these silicated chips revealed a major flaw in surface integrity when initial baseline attempts resulted in unstable signal. Thusly, poly-L-lysine (PLL), frequently applied in culture plate for cell adhesions was applied to the surface via incubation of a 0.01mg/mL solution of PLL resulting in an SPR signal of ~500 RU. The process of layering and adhering the bilayers to the PLL was facilitated through charge interaction between the positively charged poly-L-lysine and the negatively charge lipid heads groups of PEs. Two sets of lipid molar ratios, a 1:1 and a 3:1 of POPC to POPG, were examined to determine optimal lipid ratio for lipid membrane assembly onto the PLL layer. The 3:1 ratio induced stronger and reproducible SPR signals of 4000 RU compared to the 1:1 ratio SPR signal response of 1300 RU, thusly this 3:1 ratio was set as the standard for the lipid vesicles used in this double lipid bilayer system. The successful application of PLL and additional lipid vesicle adsorption with SPR responses of 500 RU and 3000 RU respectively, formed the second bilayer. This system mimics the double lipid membrane systems found in the mitochondria and the bacteria cell wall-membrane.

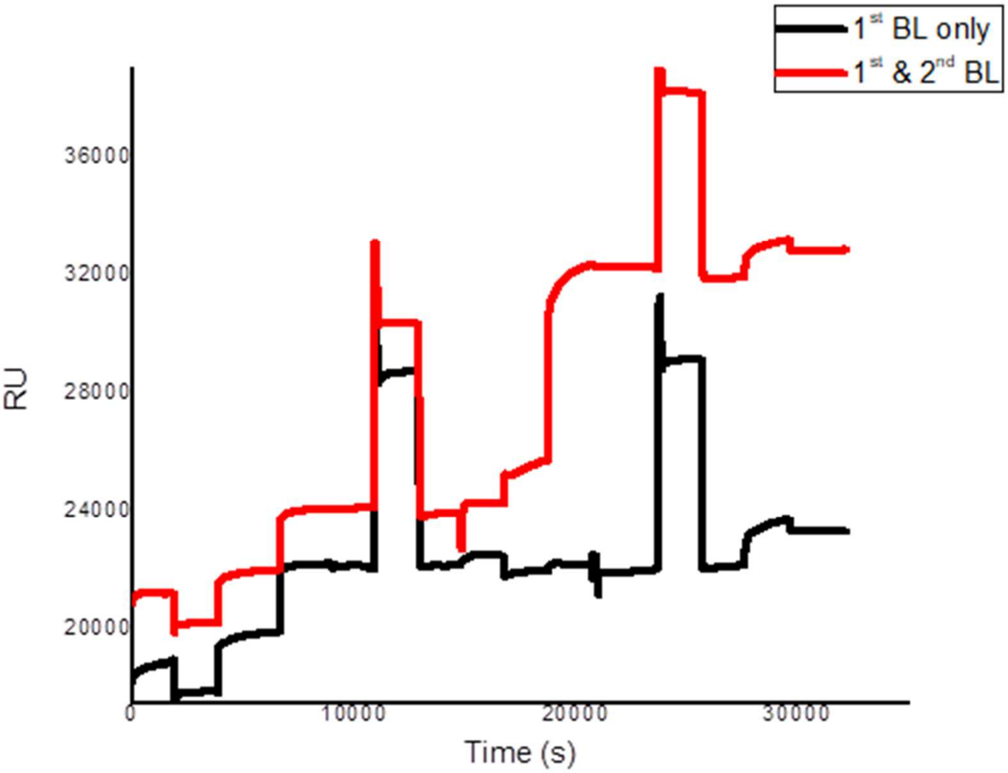

Figure 5.3 Sensorgram of single (black) and double (red) lipid bilayer system. PLL is first incubated onto the surface to facilitate adsorption of a 1:1 POPC: POPG vesicles. PEG5000 incubation ruptures intact vesicles to ensure full formation of lipid bilayer. Another round of PLL is incubated followed by a 3:1 POPC: POPG vesicles repeated with PEG5000 incubation. Streptavidin exposure on surface to show nonspecific binding on both bilayer sets.

Investigation of the double lipid membrane system as a platform for SPR detection using model protein binding pairs with the protein specific target embedded into the lipid bilayer. Both biontinyl-PE and GM1 were incorporated at 5% of the lipid ratio to ensure high surface coverage of the antigen was available for lipid-protein binding interactions. Biotinyl-PE and Streptavidin binding pair was used as a proof of concept (**Figure 5.3**) with SPR response of 900 RU for 1mg/mL of streptavidin to confirm that biotin embedded in the first bilayer and that when antigen is covered by the second bilayer that no streptavidin binding occurs. To test the sensitivity of the sensor platform, cholera toxin and GM1 binding interaction was exploited to compare the SPR response to binding on the surface of a single bilayer versus on a double bilayer system (**Figure 5.4**).

The resulting calibration curve (**Figure 5.5**) show that SPR sensitivity is similar on both the single and double bilayer system. The sensor was able to detect binding at low concentration of Cholera toxin, at 0.1ng/mL on both a single and double bilayer system with high linear correlation of R^2=0.999. The binding sensitivity is slightly higher on the single bilayer as the binding interaction is closer to the surface. The linear detection range spans from 0.1ng to 10 ng/mL and the signal begins to saturate at 100ng/mL with SPR response ranging from 50 to 6000 RU. This quantitate analysis provides suitable confirmation that the double lipid bilayer system can be applied as a sensor surface for studying binding interactions imitating the surface interfaces of biological targets such as mitochondria, chloroplasts, and gram-negative bacteria cell walls by slightly altering lipid to match targeted lipid profile.

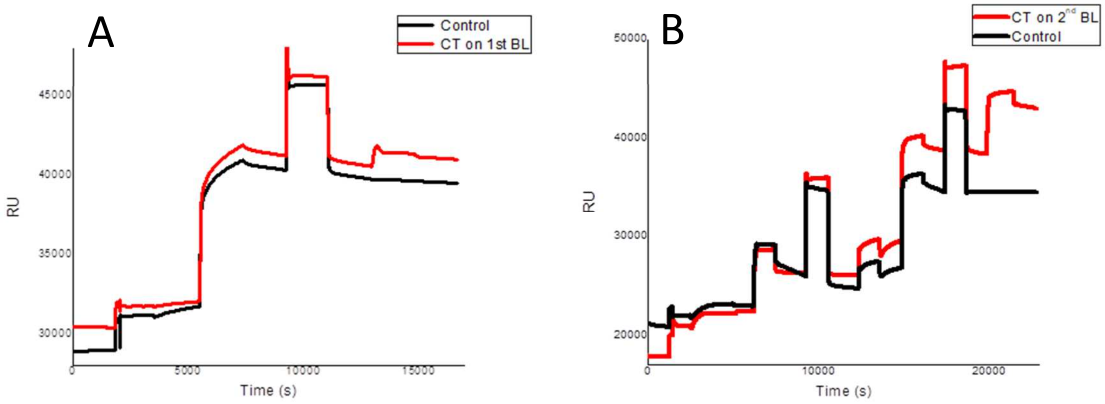

Figure 5.4 Sensorgram of Cholera Toxin binding on a **(A)** single lipid bilayer and **(B)** double lipid bilayer system. PLL incubated onto the surface to facilitate adsorption of a 3:1 POPC: POPG vesicles. PEG5000 incubation ruptures intact vesicles to ensure full formation of lipid bilayer. Second set of PLL followed by 3:1 POPC: POPG vesicles with 5% GM1 incubated on the surface. Incubation PEG5000 again to ensure lipid bilayer formation followed by 10μ/mL**(A)** and 0.1mg/mL**(B)** Cholera Toxin exposure (red) to bind to the exposed GM1 on the second bilayer.

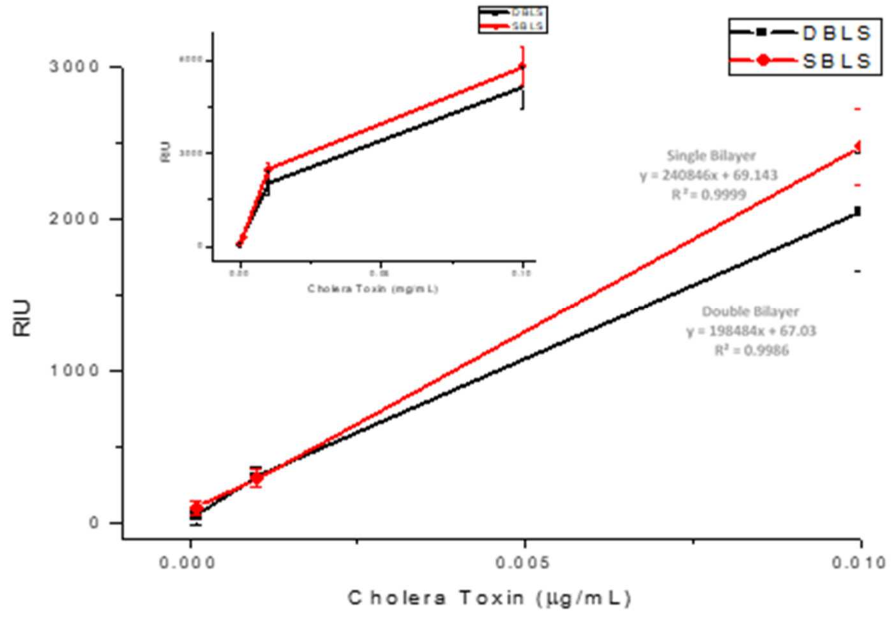

Figure 5.5 Calibration curve of cholera toxin (CT) binding to GM1 embedded in a single (Red) or double (Black) lipid bilayer system showing high sensitivity and linear correlations with detection limits at 0.1ng/mL of CT, linear range up to 10ng/mL CT, and upper limit of detection at 0.1mg/mL CT shown in inset.

Streptolysin O incorporation into lipid bilayer model system.

Proteins are major constituents of a lipid membrane profile, particularly transmembrane proteins which play major roles either as signal transduction and cascades for intra-cellular signaling or as transport channel to actively or passively facilitate movement of important molecules across the cellular membranes. Additionally, proteins can interact with specific polysaccharides that extends from the lipid membrane for various functions such as cell-to-cell recognition, antibody interaction, and many other protein interactions that may be either beneficial or detrimental to cellular health. In this work, a specific protein, Streptolysin O (SLO) was selected as it behaves as toxic transmembrane protein capable of self-insertion into lipid bilayers concertedly forming pores with diameters up to thirty nanometers. It is to be noted that this insertion process is heavily assisted by the presence of cholesterol embedded in the lipid bilayer as described in the following.

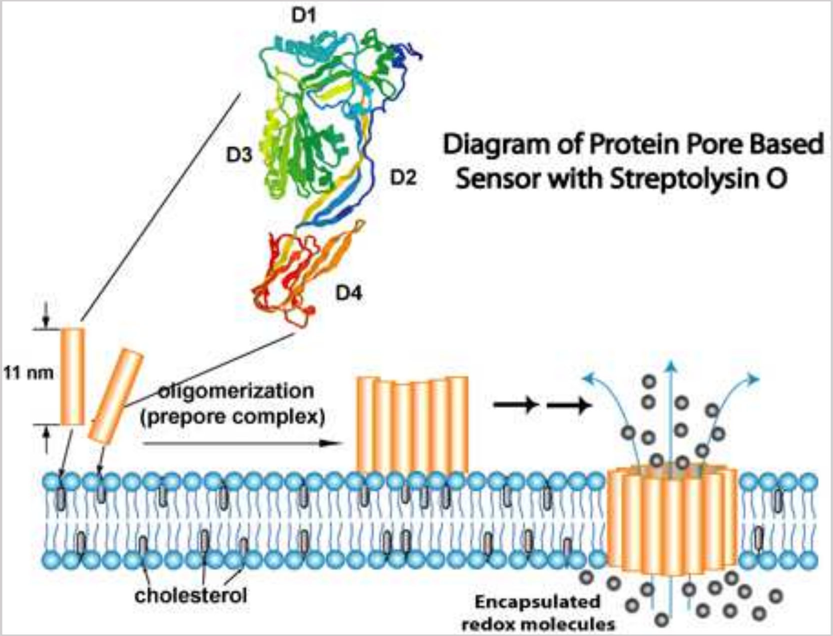

Figure 5.6 Diagram illustrating the pore formation process of streptolysin O.

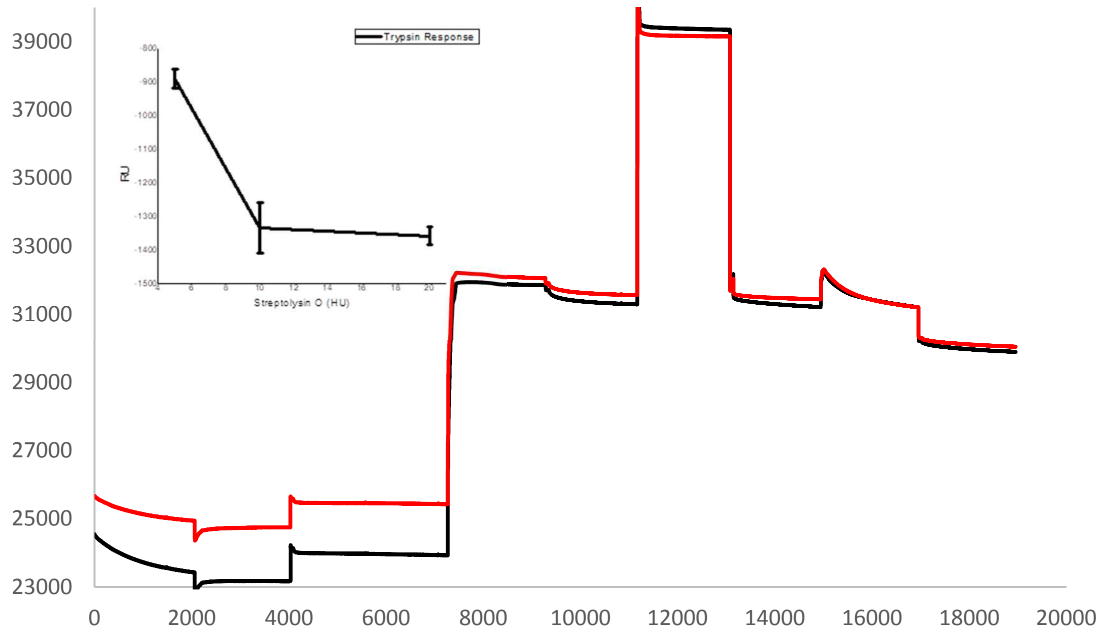

Figure 5.7 Sensorgram of single lipid bilayer formation followed by trypsin incubation and digestion. (Inset) Calibration curve of Trypsin digestion of Streptolysin O embedded in lipid bilayer demonstrating correlation between increasing streptolysin O concentration and increasing signal (RU) loss.

The consensus mechanism of pore forming toxins self-assembly into proper formation to form pores is a multi-staged process starting with initial individual monomeric binding to the lipid membrane facilitated by cholesterol **(Figure5.6)**. Proceeded by oligomerization and pore formation in the protein complex structure forming C-structure lesion and full open pores with diameters ranging up to 30nm in size[31,36–38]. The inclusion of streptolysin O into the outer membrane transforms a protecting bilayer into a biological facsimile of a size selective filters that can be exercised in conjunction with lipid bilayer surfaces. This altered model of a double lipid bilayer system will examine this potential surface for a sensor design applying this size selective filter aspect for selective binding of small biomolecules within a certain size range.

Based on our group's previous electrochemistry work[39,40], the optimal cholesterol concentration exhibited at a one-part lipid content to one-part cholesterol, which retain high lipid fluidity assisting in the transition of the transmembrane protein and the diffusing of lipids away from the site of pore formation. This project aims to confirm similar findings via surface plasmon resonance on the BiacoreX. To achieve this, trypsin digestion was harnessed as a mean of simple confirmation that streptolysin O was embedded successfully in a single lipid bilayer model. The SPR data (**Figure 5.7**) exhibits a correlation between increasing concentration of streptolysin O incorporated into the bilayer and SPR signal loss as the trypsin digestion removed the streptolysin O off the surface of the membrane, confirming the presences of embedded streptolysin O in the lipid bilayer.

While this does indicate that streptolysin O is associated with the lipid bilayer, this SPR response does not prove that the protein is correctly inserted in the membrane; an alternative conclusion could be that streptolysin O is adsorbed to the membrane surface which will exhibit similar results upon exposure to trypsin digestion. To fully confirm structural orientation, streptolysin O pore forming functionality can be exploited to determine if the toxin self-inserts and assembles into pores on the lipid membranes. The first study attempted to repeat previous work[40] utilizing horseradish peroxidase (HRP) to catalyze a 3,3',5,5'-Tetramethylbenzidine (TMB) precipitation reaction that would generate precipitate that would adsorb onto the surface generating a corresponding

SPR response. The experiment begins with functionalizing the base poly-L-lysine (PLL) monolayer on the gold surface with EDC/NHS linking reaction to covalently attach HRP. An incubation of SLO infused vesicles solution was then injected onto the surface to self-assemble into a bilayer, followed by a 10% w/w PEG5K injection to rupture any remaining intact vesicle, and ensure full lipid bilayer formation. If the streptolysin O toxin is embedded in the lipid bilayer and forming pores, TMB will have access to the HRP bound to the PLL beneath the membrane catalyzing TMB precipitate formation which should adsorb to the bilayer surface resulting in increased SPR response. Unfortunately, the SPR response did not match expectation as the hydrogen peroxide induced unstable and unexpected SPR responses during the TMB incubation and lack of SPR signal increase indicates either that TMB precipitate did not form or did not adsorb to the bilayer surface. SPR responses recorded did not correspond to colorimetric changes observed in the experimental sample outflow. In control runs testing pure membranes, the eluents exhibited no colorimetric change as predicted with matching SPR data indicates lack of TMB reaction and intact lipid bilayer. However, in experimental runs with using streptolysin O incubated vesicles, the eluent that exits the channel has changed into dark blue indicating the TMB reaction did occur and that TMB had direct access to the HRP below the lipid bilayer through the SLO pores. But the corresponding experimental SPR data did not indicate any signal shift due to TMB reaction, it was nearly identical to the sensorgram recorded from control runs.

With conflicting findings from the TMB precipitation reaction, another strategy was implemented to confirm formation of streptolysin O pores. Biotin-PEG2000-SH was functionalized directly on the bare gold surface to facilitate specific binding of streptavidin. Subsequent incubation of PLL solution formed a thin monolayer of PLL immersed with Biotin-PEG2000 to adhere the subsequent SLO incubated lipid vesicles. As per protocol, a 10% PEG5000 incubation to ensure full lipid formation followed the vesicle incubation. Streptavidin was then incubated onto the interface to monitor binding interaction directly on the lipid bilayer via SPR. After subtracting non-specific binding, the resulting data did exhibit correlating results as SPR signal did increase, ~900 RU for 0.5mg/mL of streptavidin in channels utilizing streptolysin O incubated vesicles confirming successful formation of pores induced by incubation of streptolysin O into the vesicle solutions.

Advancing this proof of concept to the double bilayer system, the experiment scheme alters the previously stated double bilayer formation procedure by embedding a target molecule, GM1, into the first lipid bilayer and incorporating streptolysin O into the second bilayer to form pores. The SLO pore formation allows cholera toxin to bind to the previously covered GM1 in the first bilayer, and this process can be monitored through SPR (**Figure 5.8**). By operating a control channel to account for non-specific binding, signal for specific binding of CT to GM1 can be approximated and this data demonstrates that channels containing streptolysin incubated lipid vesicles does elicit a stronger response upon exposure to cholera toxin indicating that the streptolysin O pores did successfully form on the outer lipid bilayer.

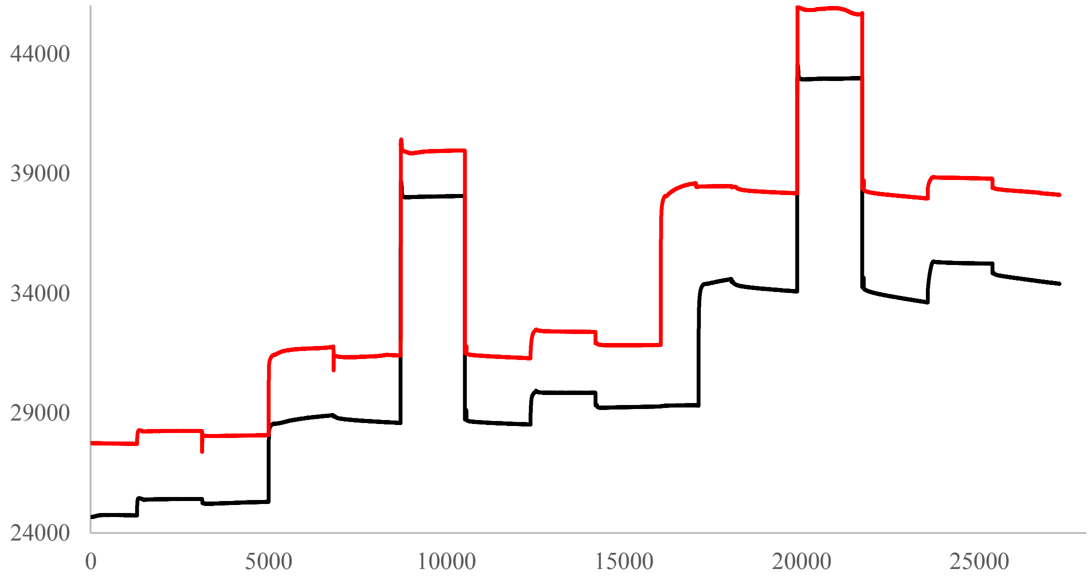

Figure 5.8 Sensorgram of double lipid bilayer formation with streptolysin incubated vesicle. PLL facilitates adsorption of 3:1 POPC to POPG with 5% GM1 lipid vesicles followed by 10% PEG5000 to rupture intact vesicles to ensure full lipid bilayer formation. Second PLL layer facilitates the second set vesicles with cholesterol at a 1:1 molar ratio (Red) and incubated with 10 HU of streptolysin O (Black) again followed by 10% PEG5000 to ensure full lipid bilayer formation. Upon exposure to 1ug/mL of cholera toxin (CT), indicates successful streptolysin O pore formation as the resulting in signal difference ~700 RU for specific binding of CT to GM1 embedded in the first lipid bilayer.

Notably, non-specific binding is present and is attributed to high cholesterol content, which literature suggests promotes the disassociation of the catalytic CTA1 subunit from the rest of the toxin and self-insertion into the lipid membrane[41]. Upon exposure to a minimum of 1ug/mL of CT, an SPR response of 100 RU can be induced and confirms that cholera toxin can pass through the pores, but the sensor interface is quickly saturated at 100ug/mL of CT with SPR responses of 1000 RU. The narrow limit of detection and comparability smaller detection range of this novel double lipid bilayer interface can be attributed to the physical dynamics of local diffusion limit in order to pass the pores and hinderance of the second PLL monolayer poses to CT from reaching the GM1 embedded in the primary lipid bilayer.

Optimizations of PLL and cholesterol were conducted to elicit how PLL and cholesterol affects binding interaction between Cholera Toxin and its target GM1 embedded in the base lipid bilayer of this double lipid bilayer system. Firstly, concentrations of PLL were investigated to determine optimal concentration to form a monolayer that retains its adhesive property for formation of the double lipid bilayer structure yet does not hinder cholera toxin interaction with GM1 on the surface of the first bilayer underneath the PLL monolayer. Data from low concentration of PLL (0.001mg/mL) exhibits substantially lowered SPR signal ~100 RU for the PLL and ~ 500 RU for the second lipid bilayer formation step, this difference in SPR response indicates that low concentration (0.001mg/mL) of PLL did not fully adsorbed vesicles to fully form an intact lipid bilayer. Data from high concentration of PLL (0.1mg/mL) exhibits proper self-assembly of second lipid bilayer, yet the SPR response of ~20 RU upon 10μg/mL cholera toxin exposure lead to an abnormally weak interaction likely due to the steric hindrance from an increase in the PLL monolayer thickness hindering the binding between CT to GM1.

Cholesterol concentration was briefly investigated as the high lipid fluidity may be a cause of non-specific interaction within this system[31,42]. A comparatively lower cholesterol ratio of 9:1 lipid to cholesterol was examined to observe the effects of a lowered cholesterol concentration on streptolysin O pore formation. Data from second lipid bilayer with lowered cholesterol concentration did exhibit an overall decrease in SPR response of cholera toxin interaction, this decrease in specific binding can be attributed to weaker streptolysin O pore formation within the second lipid bilayer which in turns reduces access to GM1 embedded in the first lipid bilayer. Non-specific binding is also reduced, aligning to the previously inferred[41] that non-specific binding is attributed to CTA1 subunit integration into the second lipid bilayer due to high cholesterol content.

5.4 Conclusion.

In summary, this double lipid bilayer system investigated in this project provided proof of concepts for a biomimetic of double lipid bilayers interface for modeling complex lipid membranes systems present in nature such as the mitochondria, chloroplasts, and gram-negative bacteria on a SPR based sensor. Comparison of the single lipid bilayer and double lipid bilayer systems demonstrated that this surface interface is capable as a biomolecule sensor with sensitivity spanning from 0.1ng/mL to 10ng/mL of cholera toxin with upper limit of detection of 100ng/mL similar to previous SPR immunosensors using antibody bindings[43,44]. Streptolysin O toxin was utilized to examine this sensor interface potential to interrogate transmembrane protein and protein-lipid interaction via SPR. Streptolysin O toxin was confirmed to have self-assembled into the lipid bilayer and form pores, this additionally tested the novel application of streptolysin O pore functionalized lipid bilayer as a size selective membrane system. Optimization of double lipid bilayer system were examined to the PLL layer density to obtain balance between successful adsorption of the second bilayer onto the surface and allowing cholera toxin reach GM1 within the first lipid bilayer underneath the PLL layer.

To increase accuracy of modeling gram negative bacteria cell walls, the lipid composition was adjusted to mimic lipid ratios found within living gram-negative bacteria of 81% PE and 19% POPC and the double bilayer system was successfully formed with similar sensitivity to streptavidin-biotin binding. This double lipid bilayer system is a novel platform for SPR analysis of complex lipid bilayer assembly as a sensor for protein-lipid interactions. This platform can be directed towards discovering new potential drug-protein interaction directly at the lipid membrane interface without need for antibodies or signal amplification techniques. To aid in this avenue of interest, revamping the model to improve gram-negative bacteria wall model accuracy is essential. Restructuring the current model by replacing the base PLL layer with silicate gold surface to improve lipid membrane mobility and the second PLL layer with peptidoglycan will better resemble gram negative bacteria and may improve the platform’s ability to elicit understanding of interactions directly at membrane interfaces.

References:

(1) Tanabe, M.; Ando, K.; Komatsu, R.; Morigaki, K. Nanofluidic Biosensor Created by Bonding Patterned Model Cell Membrane and Silicone Elastomer with Silica Nanoparticles. *Small* **2018**, *14* (49), 1802804.

(2) Osaki, T.; Takeuchi, S. Artificial Cell Membrane Systems for Biosensing Applications. *Anal. Chem.* **2017**, *89* (1), 216–231.

(3) Qiu, L.; Zhang, T.; Jiang, J.; Wu, C.; Zhu, G.; You, M.; Chen, X.; Zhang, L.; Cui, C.; Yu, R.; et al. Cell Membrane-Anchored Biosensors for Real-Time Monitoring of the Cellular Microenvironment. *J. Am. Chem. Soc.* **2014**, *136* (38), 13090–13093.

(4) Sharma, S.; Kim, B. N.; Stansfeld, P. J.; Sansom, M. S. P. A Coarse Grained Model for a Lipid Membrane with Physiological Composition and Leaflet Asymmetry. *PLoS One* **2015**, *10* (12), 1–21.

(5) Pasenkiewicz-Gierula, M.; Baczynski, K.; Markiewicz, M.; Murzyn, K. Computer Modelling Studies of the Bilayer/Water Interface. *Biochim. Biophys. Acta - Biomembr.* **2016**, *1858* (10), 2305–2321.

(6) Schindler, T.; Kröner, D.; Steinhauser, M. O. On the Dynamics of Molecular Self-Assembly and the Structural Analysis of Bilayer Membranes Using Coarse-Grained Molecular Dynamics Simulations. *Biochim. Biophys. Acta - Biomembr.* **2016**, *1858* (9), 1955–1963.

(7) Marrink, S. J.; Corradi, V.; Souza, P. C. T.; Ingólfsson, H. I.; Tieleman, D. P.; Sansom, M. S. P. Computational Modeling of Realistic Cell Membranes. *Chem. Rev.* **2019**, *119* (9), 6184–6226.

(8) Moriwaki, H.; Yamada, K.; Nakanishi, H. Evaluation of the Interaction between Pesticides and a Cell Membrane Model by Surface Plasmon Resonance Spectroscopy Analysis. *J. Agric. Food Chem.* **2017**, *65* (26), 5390–5396.

(9) Stahelin, R. V; Bement, W. Surface Plasmon Resonance : A Useful Technique for Cell Biologists to Characterize Biomolecular Interactions. *Mol. Biol.* **2013**, *24*, 883–886.

(10) Andersson, J.; Köper, I. Tethered and Polymer Supported Bilayer Lipid Membranes: Structure and Function. *Membranes (Basel).* **2016**, *6* (2).

(11) Andoh, Y.; Okazaki, S.; Ueoka, R. Molecular Dynamics Study of Lipid Bilayers Modeling the Plasma Membranes of Normal Murine Thymocytes and Leukemic GRSL Cells. *Biochim. Biophys. Acta - Biomembr.* **2013**, *1828* (4), 1259–1270.

(12) Taylor, J. D.; Linman, M. J.; Wilkop, T.; Cheng, Q. Regenerable Tethered Bilayer Lipid Membrane Arrays for Multiplexed Label-Free Analysis of Lipid−Protein Interactions on Poly(Dimethylsiloxane) Microchips Using SPR Imaging. *Anal. Chem.* **2009**, *81* (3), 1146–1153.

(13) Hinman, S. S.; Ruiz, C. J.; Drakakaki, G.; Wilkop, T. E.; Cheng, Q. On-Demand Formation of Supported Lipid Membrane Arrays by Trehalose-Assisted Vesicle Delivery for SPR Imaging. *ACS Appl. Mater. Interfaces* **2015**, *7* (31), 17122–17130.

(14) Jackman, J. A.; Knoll, W.; Cho, N. J. Biotechnology Applications of Tethered Lipid Bilayer Membranes. *Materials (Basel).* **2012**, *5* (12), 2637–2657.

(15) Wilson, B. A.; Ramanathan, A.; Lopez, C. F. Cardiolipin-Dependent Properties of Model Mitochondrial Membranes from Molecular Simulations. *Biophys. J.* **2019**, *117* (3), 429–444.

(16) Michel, J. P.; Wang, Y. X.; Kiesel, I.; Gerelli, Y.; Rosilio, V. Disruption of Asymmetric Lipid Bilayer Models Mimicking the Outer Membrane of Gram-Negative Bacteria by an Active Plasticin. *Langmuir* **2017**, *33*, 11028–11039.

(17) Andersson, J.; Fuller, M. A.; Wood, K.; Holt, A. A Tethered Bilayer Lipid Membrane That Mimics Microbial Membranes. *PCCP* **2018**, *20*, 12958–12969.

(18) Maynard, J. A.; Lindquist, N. C.; Sutherland, J. N.; Lesuffleur, A.; Warrington, A. E.; Rodriguez, M.; Oh, S.-H. Next Generation SPR Technology of Membrane-Bound Proteins for Ligand Screening and Biomarker Discovery. *Biotechnol J.* **2019**, *4* (11), 1542–1558.

(19) Robertson, J. L. The Lipid Bilayer Membrane and Its Protein Constituents. *J. Gen. Physiol.* **2018**, *150* (11), 1472–1483.

(20) Squillace, O.; Esnault, C.; Pilard, J.-F.; Brotons, G. Electrodes for Membrane Surface Science. Bilayer Lipid Membranes Tethered by Commercial Surfactants on Electrochemical Sensors. *ACS Sensors* **2019**, *4* (5), 1337–1345.

(21) Raguse, B.; Braach-Maksvytis, V.; Cornell, B. A.; King, L. G.; Osman, P. D. J.; Pace, R. J.; Wieczorek, L. Tethered Lipid Bilayer Membranes: Formation and Ionic Reservoir Characterization. *Langmuir* **1998**, *14* (3), 648–659.

(22) Taylor, J. D.; Phillips, K. S.; Cheng, Q. Microfluidic Fabrication of Addressable Tethered Lipid Bilayer Arrays and Optimization Using SPR with Silane-Derivatized Nanoglassy Substrates. *Lab Chip* **2007**, *7* (7), 927–930.

(23) Wang, Z.; Wilkop, T.; Cheng, Q. Characterization of Micropatterned Lipid

Membranes on a Gold Surface by Surface Plasmon Resonance Imaging and Electrochemical Signaling of a Pore-Forming Protein. *Langmuir* **2005**, *21* (23), 10292–10296.

(24) Heath, G. R.; Li, M.; Polignano, I. L.; Richens, J. L.; Catucci, G.; Shea, P. O.; Sadeghi, S. J.; Gilardi, G.; Butt, J. N.; Jeuken, L. J. C. Layer-by-Layer Assembly of Supported Lipid Bilayer Poly-L-Lysine Multilayers. *Biomacromolecules* **2016**, No. 17, 324–355.

(25) Heath, G. R.; Li, M.; Rong, H.; Radu, V.; Frielingsdorf, S.; Lenz, O.; Butt, J. N.; Jeuken, L. J. C. Multilayered Lipid Membrane Stacks for Biocatalysis Using Membrane Enzymes. *Adv. Funct. Mater.* **2017**, *27* (17).

(26) Hartman, K. L.; Kim, S.; Kim, K.; Nam, J.-M. Supported Lipid Bilayers as Dynamic Platforms for Tethered Particles. *Nanoscale* **2015**, *7* (1), 66–76.

(27) Chung, M.; Boxer, S. G. Stability of DNA-Tethered Lipid Membranes with Mobile Tethers. *Langmuir* **2011**, *27* (9), 5492–5497.

(28) Chung, M.; Lowe, R.; Chan, Y.-H. M.; Ganesan, P. V.; Boxer, S. G. DNA-Tethered Membranes Formed by Giant Vesicle Rupture Boxer*. *J. Struct Biol.* **2009**, *168* (1), 190–199.

(29) Chen, C. Y.; Hinman, S. S.; Duan, J.; Cheng, Q. Nanoglassified, Optically-Active Monolayer Films of Gold Nanoparticles for in Situ Orthogonal Detection by Localized Surface Plasmon Resonance and Surface-Assisted Laser Desorption/Ionization-MS. *Anal. Chem.* **2014**, *86* (24), 11942–11945.

(30) Bhakdi, S.; Tranum-Jensen, J.; Sziegoleit, A. Mechanism of Membrane Damage by Streptolysin-O. *Infect. Immun.* **1985**, *47* (1), 52–60.

(31) De, S.; Bubnys, A.; Alonzo, F.; Hyun, J.; Lary, J. W.; Cole, J. L.; Torres, V. J.; Olson, R. The Relationship between Glycan Binding and Direct Membrane Interactions in Vibrio Cholerae Cytolysin, a Channel-Forming Toxin. *J. Biol. Chem.* **2015**, *290* (47), 28402–28415.

(32) Biacore. Biacore Sensor Surface Handbook. *Biaore* **2003**.

(33) Duan, J.; Linman, M. J.; Cheng, Q. Ultrathin Calcinated Films on a Gold Surface for Highly Effective Laser Desorption/ Ionization of Biomolecules. *Anal. Chem.* **2015**, *82* (12), 5088–5094.

(34) Hinman, S. S.; McKeating, K. S.; Cheng, Q. DNA Linkers and Diluents for Ultrastable Gold Nanoparticle Bioconjugates in Multiplexed Assay Development. *Anal. Chem.* **2017**, *89* (7), 4272–4279.

(35) Hinman, S. S.; Mckeating, K. S.; Cheng, Q. Plasmonic Sensing with 3D Printed Optics. *Anal. Chem.* **2017**, No. 89, 12626–12630.

(36) Feil, S. C.; Ascher, D. B.; Kupler, M. J.; Tweeten, R. K.; Parker, M. W. Structural Studies of Streptococcus Pyogenes Streptolysin O Provide Insights into the Early Steps of Membrane Penetration Susanne. *J. Mol. Biol.* **2015**, *426* (4), 785–792.

(37) Fujinaga, Y.; Wolf, A. A.; Rodighiero, C.; Wheeler, H.; Tsai, B.; Allen, L.; Jobling, M. G.; Rapoport, T.; Holmes, R. K.; Lencer, W. I. Gangliosides That Associate with Lipid Rafts Mediate Transport of Cholera and Related Toxins from the Plasma Membrane to Endoplasmic Reticulm. *Mol. Biol. Cell* **2003**, *14*, 5069–5081.

(38) Krueger, E.; Brown, A. C. Inhibition of Bacterial Toxin Recognition of Membrane Components as an Anti-Virulence Strategy. *J. Biol. Eng.* **2019**, *13* (1), 1–14.

(39) Wilkop, T.; Xu, D.; Cheng, Q. Electrochemical Characterization of Pore Formation by Bacterial Protein Toxins on Hybrid Supported Membranes. *Langmuir* **2008**, *24* (10), 5615–5621.

(40) Wilkop, T.; Xu, D.; Cheng, Q. Characterization of Pore Formation by Streptolysin O on Supported Lipid Membranes by Impedance Spectroscopy and Surface Plasmon Resonance Spectroscopy. *Langmuir* **2007**, *23* (3), 1403–1409.

(41) Ray, S.; Taylor, M.; Banerjee, T.; Tatulian, S. A.; Teter, K. Lipid Rafts Alter the Stability and Activity of the Cholera Toxin A1 Subunit. *J. Biol. Chem.* **2012**, *287* (36), 30395–30405.

(42) Soo, J. C.; Zhang, J.; He, Q.; Agarwal, S.; Li, H.; Zhang, H.; Chen, P. Surface Immobilized Cholera Toxin B Subunit (CTB) Facilitates Vesicle Docking, Trafficking and Exocytosis. *Integr. Biol.* **2010**, *2* (5–6), 250–257.

(43) Liu, Y.; Dong, Y.; Jauw, J.; Linman, M. J.; Cheng, Q. Highly Sensitive Detection of Protein Toxins by Surface Plasmon Resonance with Biotinylation-Based Inline Atom Transfer Radical Polymerization Amplification. *Anal. Chem.* **2010**, *82* (9), 3679–3685.

(44) Hodnik, V.; Anderluh, G. Toxin Detection by Surface Plasmon Resonance. *Sensors* **2009**, *9* (3), 1339–1354.

Chapter Six: Conclusion and Future Work

The work in this dissertation has demonstrated the development of various biosensors for VOCs, biochemicals, and bacterial analysis using nanofibers and surface plasmon resonance. Nanofibers were developed into biosensor designed for detecting and quantifying VOCs (Chapter 2) and biochemical analytes (Chapter 3). Localized surface plasmon resonance was used in tandem with 3D printing to develop novel biosensors for biochemical analysis (Chapter 4). In the last experimental chapter (Chapter 5), an experimental bacterial cell wall model was developed for SPR analysis as a novel tool for studying compound interactions at the double lipid bilayer interface.

In Chapter 2, we detailed the successful approach to VOCs monitoring through composite polyaniline (PANi) nanofiber chemiresistor to achieve PPM level of sensitivity towards aliphatic alcohols. Chemiresistor sensors is a mature application of conductive nanofiber that has generated a significant amount of interest due to its facile development and customization to sensitively detect various gaseous analytes. We have demonstrated both the conductivity and sensitivity of composite PANi nanofiber chemiresistor can be tuned by incorporating various states of reduced graphene oxide (rGO). We also have compared the performances of the nanofiber sensors with their thin-film counterparts.

Like many nanofiber chemiresistor, not only is the sensor susceptible to noise from humidity but also analyte selectivity remains an issue[1–4]. A pressurized sample chamber can be employed to maintain a consistent testing environment to mitigate noise from humidity. This chapter has shown that the pattern of the analyte responses from the various rGO component can be analyzed and used to identify the analyte through principal component analysis (PCA). After identifying the analyte, the response can be compared to the calibration curves to quantify the analyte with PPM sensitivity.

The future direction of this project focuses on coating the nanofibers with nanoparticles to further tune the conductivity of nanofibers and incorporate molecular binding interactions to improve the biological recognition element. Coaxial electrospinning, a well-studied strategy to fabricate nanofibers with a distinct outer and inner layer, has recently been used to coat nanofibers with nanoparticles[5,6]. Not only will conductive nanoparticles further increase the conductivity, but it may also improve the sensor sensitivity by increasing the sensor response when exposed to the analyte. The lack of a selective biorecognition element of the PANi/HCSA/rGO composite nanofiber sensor can also be addressed using these nanoparticles. The nanoparticles reside on the nanofiber exterior exposed to the analytes. The nanoparticle surfaces can be either modified before electrospinning or post electrospinning to introduce target analyte-specific binding interactions for this sensor surface to improve its selectivity.

In Chapter 3, we detailed the application of polyvinyl alcohol (PVA) nanofibers as a sensor substrate functionalized with silver nanoparticles (AgNPs) for fluorescence detection of biochemical analytes. Recently reported works using nanofibers and silver nanoparticles have employed the nanofibers as a scaffold that inherits the AgNPs' antimicrobial properties for applications in medical or food industrial purposes. In this project, the nanofiber also serves as a scaffold, but the AgNPs have not used for its antimicrobial properties, but as a biorecognition element in a fluorescent-based sensor for biochemical analysis. This is accomplished by functionalizing the AgNPs with ethylenediaminetetraacetic acid (EDTA) to chelate metal ions. These metal ions are used to bind metal-binding ligands or proteins such as nitrilotriacetic acid (NTA) and poly-histidine tagged proteins, respectively. NTA can be added to ligands to selectively bind specific analytes. In this case, NTA was functionalized to biotin to allow the sensor to selectively bind NeutrAvidin with sub-micromolar sensitivity.

In this chapter, we have also demonstrated that the AgNPs are also capable of localized surface plasmon resonance (LSPR) detection as the sensor surface was sensitive to changes in the bulk refractive index with a strong linear correlation (R2=0.98). The sensor was sensitive to changes in the bulk refractive index, yet experimental studies of detecting metal ions resulted in no correlation between the observed LSPR response and the concentrations of metal ions bound on the sensor surface. The binding of NTA-Biotin also suffered from a lack of LSPR detection due to the small size. While nanoparticle LSPR is known to be able to detect small analytes like metal ions, this is normally facilitated through the amplification effect of the aggregation of free nanoparticle in solution[7,8]. The aggregation of the AgNPs is not possible as they are adsorbed onto the nanofiber surface. However, this arrangement creates a surface capable of binding metal ions proven through the fluorescent study. can still be applied to large compounds such as proteins. The current density of the nanofiber mat influenced the light scattering, which some complications for LSPR detection. Future direction for this project focuses on optimizing the parameters of the nanofiber substrate to reduce the interfering scattering effect. A single layer of nanofiber functionalized with the EDTA-AgNPs should have the least interference and would improve the LSPR signal for protein detection and possible the metal ion detection as well.

In Chapter 4, we demonstrated the novel application of 3D printing to fabricate a cost-effective and disposable surface for LSPR detection of biochemical analytes. The 3D printed prisms were modified with several rounds of hand-sanding and polishing to obtain parameters that are functionally comparable to commercial prisms. These prisms were coated with gold nanoparticles (AuNPs) grown in-situ on the prism surface to fabricate an LSPR responsive surface. The biorecognition element was crafted by functionalizing the AuNPs with DNA oligomers. These DNA oligomers can either capture complementary DNA single strands or be directly functionalized with a ligand to directly capture a targeted analyte. Complimentary strands functionalized with biotin were recruited to DNA functionalized AuNPs surfaces to selectively capture streptavidin with sub-micromolar sensitivity. Because avidin has been used as a bridge to recruit biotin-tagged antibodies, this sensor can incorporate the same strategy to selectively detect an increased range of target analytes. However, increasing the number of binding steps tends to further decrease sensitivity and increase variance in signal response. There are many directions for future work that can be derived from this project.

First and foremost, the ten-fold difference in the surface roughness between the 3D printed and commercial prisms can be reduced by increasing the thoroughness of the post-fabrication treatment. By reducing the surface roughness, this will reduce the difference of the light scattering effect experienced on the AuNPs due to differential z position on the sensor surface[9–11], which in turn will decrease the width of the absorption peak and increase the sensor sensitivity for all future applications. Another solution is the alteration of the nanoparticle synthesis to create nanoparticles with homogenous diameters. This will also decrease the broadness of the absorbance peak, which again will increase the sensor sensitivity[12–14].

The next future direction is to modify the DNA oligomers functionalized to the AuNPs surface to capture complementary single-strand DNA or RNA that serves as disease biomarkers. Because these nanoparticles are immobilized on the surface, normal DNA-AuNPs aggregation strategies will not work. A strategy to ensure sensitive detection is to customize the DNA oligomer sequence to capture a majority (50-80%) of the targeted complementary strand. This signal can be amplified through signal enhancement from AuNPs. The AuNPs' large mass will cause a significant increase in the LSPR shift and can also couple with the LSPR exhibited by the bound AuNPs. The secondary set of AuNPs will be functionalized with DNA oligomers to only capture the remaining (20-50%) of the targeted DNA strand. Focusing the oligomers with unique DNA sequences will aid in minimizing nonspecific binding from interfering DNA or RNA sequences that may also be present in the sample[15–18].

In Chapter 5, we detailed the fabrication of a double lipid bilayer model system for SPR analysis to serve as a novel tool to investigate interactions that occur on bacterial membranes. Current bacterial membranes models are mostly theoretical models[19–21] with a few simplified experimental models[22–25] without any sensing applications. This experimental double lipid bilayer model was designed to mimic the membrane system of the gram-negative bacteria. This model aid in eliciting understanding of chemical and biological interaction occurring at this unique interface, which can be a useful tool for novel drug discovery. Experimental studies exploring this model's potential as a sensor system used cholera toxin (CT) binding to monosialic gangliosides (GM1) demonstrated nanomolar level of sensitivity. The study also showed that there was minimal sensitivity loss at the double lipid bilayer interface compared to the single lipid bilayer interface. This model demonstrated the ability to monitor and detect transmembrane protein interactions using a pore-forming toxin, streptolysin O (SLO). Because of the rigidity of this lipid bilayer from the poly-L-lysine (PLL) adhesive layer, the actual intercalation of the SLO toxin was not observed. Thus, the SLO toxin was incubated with the lipids forming the outer lipid membrane as an alternative. The incorporation of SLO was investigated and confirmed through several methods.

The future direction of this work focuses on improving the model accuracy of replicating the gram-negative bacteria cell wall and membrane. Adjustment of the lipid fluidity within this double lipid bilayer model is required. The strategy of utilizing PLL as an adhesive between the lipid bilayers was sourced from Heath et al's work[26]. PLL was also implemented as the adhesive layer between the gold surface and the initial lipid bilayer. As mentioned previously, the low lipid mobility negatively affects the model performances as intercalation of transmembrane protein strongly is affected by lipid mobility. The first step in solving this issue is to silicate the surface of the gold substrate. This is silication has already been proven and implemented in our groups work[27–30] with SPR and lipid bilayers but was not adapted to this project due to concerns with the BiacoreX instrument. These concerns have recently been addressed and silicate gold surface can now be utilized with this instrument. This silication will remove the need for the first PLL layer underneath the double lipid bilayer model, which would improve the lipid mobility of the model.

To further improve lipid mobility, the remaining PLL is to be substituted with peptidoglycans. Peptidoglycans are naturally found on the surface of gram-positive bacteria and between the lipid layers of a gram-negative bacteria. While peptidoglycans serve as surface antigens of gram-positive bacteria, they facilitate the anchoring of the two sets of lipid bilayers in gram-negative bacteria. This process is facilitated by teichoic acid (TA) and lipoteichoic acids (LTA) present in the inner layers of both the lipid membranes. The LTA interacts with the peptidoglycans layer to tie the two sets of lipid bilayer together. By incorporating LTA into both sets of lipid membranes, peptidoglycan can substitute the remaining PLL layer. Not only will the incorporation of peptidoglycan facilitate the mimicking of a gram-positive bacteria membrane, but also the peptidoglycan replacement of PLL should further increase lipid fluidity to match natural membranes of the gram-negative bacteria.

In conclusion, the development of biosensors and experimental models utilized on these sensors are important to aid in monitoring chemicals and biological analytes of interest in the industrial and medical fields. The objective of this research was to fabricate several types of biosensors to address some of these issues that are assessed in environmental and health related issues. As new biosensor designs develop and evolve, they will create new tools for detection and analysis of trace analytes vital for diagnosing, monitoring, and preventing the degradation of both environmental and human health.

References:

(1) Xie, Z.; Ramakrishnam Raju, M. V.; Stewart, A. C.; Nantz, M. H.; Fu, X. A. Imparting Sensitivity and Selectivity to a Gold Nanoparticle Chemiresistor through Thiol Monolayer Functionalization for Sensing Acetone. *RSC Adv.* **2018**, *8* (62), 35618–35624.

(2) Kwak, C. H.; Kim, T. H.; Jeong, S. Y.; Yoon, J. W.; Kim, J. S.; Lee, J. H. Humidity-Independent Oxide Semiconductor Chemiresistors Using Terbium-Doped SnO2 Yolk-Shell Spheres for Real-Time Breath Analysis. *ACS Appl. Mater. Interfaces* **2018**, *10* (22), 18886–18894.

(3) Kim, I. D.; Rothschild, A.; Lee, B. H.; Kim, D. Y.; Jo, S. M.; Tuller, H. L. Ultrasensitive Chemiresistors Based on Electrospun TiO 2 Nanofibers. *Nano Lett.* **2006**, *6* (9), 2009–2013.

(4) Avossa, J.; Paolesse, R.; Di Natale, C.; Zampetti, E.; Bertoni, G.; De Cesare, F.; Scarascia-Mugnozza, G.; Macagnano, A. Electrospinning of Polystyrene/Polyhydroxybutyrate Nanofibers Doped with Porphyrin and Graphene for Chemiresistor Gas Sensors. *Nanomaterials* **2019**, *9* (2).

(5) Prado-Prone, G.; Silva-Bermudez, P.; Almaguer-Flores, A.; García-Macedo, J. A.; García, V. I.; Rodil, S. E.; Ibarra, C.; Velasquillo, C. Enhanced Antibacterial Nanocomposite Mats by Coaxial Electrospinning of Polycaprolactone Fibers Loaded with Zn-Based Nanoparticles. *Nanomedicine Nanotechnology, Biol. Med.* **2018**, *14* (5), 1695–1706.

(6) Yu, D. G.; Zhou, J.; Chatterton, N. P.; Li, Y.; Huang, J.; Wang, X. Polyacrylonitrile Nanofibers Coated with Silver Nanoparticles Using a Modified Coaxial Electrospinning Process. *Int. J. Nanomedicine* **2012**, *7*, 5725–5732.

(7) Praig, V. G.; McIlwee, H.; Schauer, C. L.; Boukherroub, Rabah Szunerits, A. Localized Surface Plasmon Resonance of Gold Nanoparticle-Modified Chitosan Films for Heavy-Metal Ions Sensing. *J. Nanosci. Nanotechnol.* **2009**, *9* (1), 350–357.

(8) Jayabal, S.; Pandikumar, A.; Lim, H. N.; Ramaraj, R.; Sun, T.; Huang, N. M. A Gold Nanorod-Based Localized Surface Plasmon Resonance Platform for the Detection of Environmentally Toxic Metal Ions. *Analyst* **2015**, *140* (8), 2540–2555.

(9) Cao, L.; Sendur, K. Surface Roughness Effects on the Broadband Reflection for Refractory Metals and Polar Dielectrics. *Materials (Basel).* **2019**, *12* (19).

(10) Lu, Y. W.; Li, L. Y.; Liu, J. F. Influence of Surface Roughness on Strong Light-

Matter Interaction of a Quantum Emitter-Metallic Nanoparticle System. *Sci. Rep.* **2018**, *8* (1), 1–11.

(11) Byun, K. M.; Yoon, S. J.; Kim, D. Effect of Surface Roughness on the Extinction-Based Localized Surface Plasmon Resonance Biosensors. *Appl. Opt.* **2008**, *47* (31), 5886–5892.

(12) Ruffino, F.; Piccitto, G.; Grimaldi, M. G. Simulations of the Light Scattering Properties of Metal/Oxide Core/Shell Nanospheres. *J. Nanosci.* **2014**, *2014*, 1–11.

(13) Jeon, H. Bin; Tsalu, P. V.; Ha, J. W. Shape Effect on the Refractive Index Sensitivity at Localized Surface Plasmon Resonance Inflection Points of Single Gold Nanocubes with Vertices. *Sci. Rep.* **2019**, *9* (1), 1–8.

(14) Guo, L.; Jackman, J. A.; Yang, H. H.; Chen, P.; Cho, N. J.; Kim, D. H. Strategies for Enhancing the Sensitivity of Plasmonic Nanosensors. *Nano Today* **2015**, *10* (2), 213–239.

(15) Ye, Y.; Gao, J.; Zhuang, H.; Zheng, H.; Sun, H.; Ye, Y.; Xu, X.; Cao, X. Electrochemical Gene Sensor Based on a Glassy Carbon Electrode Modified with Hemin-Functionalized Reduced Graphene Oxide and Gold Nanoparticle-Immobilized Probe DNA. *Microchim. Acta* **2017**, *184* (1), 245–252.

(16) Kumarasamy, J.; Camarada, M. B.; Venkatraman, D.; Ju, H.; Dey, R. S.; Wen, Y. One-Step Coelectrodeposition-Assisted Layer-by-Layer Assembly of Gold Nanoparticles and Reduced Graphene Oxide and Its Self-Healing Three-Dimensional Nanohybrid for an Ultrasensitive DNA Sensor. *Nanoscale* **2018**, *10* (3), 1196–1206.

(17) Matsishin, M.; Rachkov, A.; Lopatynskyi, A.; Chegel, V.; Soldatkin, A.; El'skaya, A. Selective Amplification of SPR Biosensor Signal for Recognition of RpoB Gene Fragments by Use of Gold Nanoparticles Modified by Thiolated DNA. *Nanoscale Res. Lett.* **2017**, *12* (1), 0–5.

(18) Rashid, J. I. A.; Yusof, N. A. The Strategies of DNA Immobilization and Hybridization Detection Mechanism in the Construction of Electrochemical DNA Sensor: A Review. *Sens. Bio-Sensing Res.* **2017**, *16* (September), 19–31.

(19) Sharma, S.; Kim, B. N.; Stansfeld, P. J.; Sansom, M. S. P. A Coarse Grained Model for a Lipid Membrane with Physiological Composition and Leaflet Asymmetry. *PLoS One* **2015**, *10* (12), 1–21.

(20) Pasenkiewicz-Gierula, M.; Baczynski, K.; Markiewicz, M.; Murzyn, K. Computer Modelling Studies of the Bilayer/Water Interface. *Biochim. Biophys. Acta - Biomembr.* **2016**, *1858* (10), 2305–2321.

(21) Schindler, T.; Kröner, D.; Steinhauser, M. O. On the Dynamics of Molecular Self-Assembly and the Structural Analysis of Bilayer Membranes Using Coarse-Grained Molecular Dynamics Simulations. *Biochim. Biophys. Acta - Biomembr.* **2016**, *1858* (9), 1955–1963.

(22) Stahelin, R. V; Bement, W. Surface Plasmon Resonance : A Useful Technique for Cell Biologists to Characterize Biomolecular Interactions. *Mol. Biol.* **2013**, *24*, 883–886.

(23) Andersson, J.; Köper, I. Tethered and Polymer Supported Bilayer Lipid Membranes: Structure and Function. *Membranes (Basel).* **2016**, *6* (2).

(24) Lind, T. K.; Skoda, M. W. A.; Cárdenas, M. Formation and Characterization of Supported Lipid Bilayers Composed of Phosphatidylethanolamine and Phosphatidylglycerol by Vesicle Fusion, a Simple but Relevant Model for Bacterial Membranes. *ACS Omega* **2019**, *4* (6), 10687–10694.

(25) Hsia, C. Y.; Chen, L.; Singh, R. R.; DeLisa, M. P.; Daniel, S. A Molecularly Complete Planar Bacterial Outer Membrane Platform. *Sci. Rep.* **2016**, *6* (April), 1–14.

(26) Heath, G. R.; Li, M.; Polignano, I. L.; Richens, J. L.; Catucci, G.; Shea, P. O.; Sadeghi, S. J.; Gilardi, G.; Butt, J. N.; Jeuken, L. J. C. Layer-by-Layer Assembly of Supported Lipid Bilayer Poly-L-Lysine Multilayers. *Biomacromolecules* **2016**, No. 17, 324–355.

(27) Hinman, S. S.; Ruiz, C. J.; Drakakaki, G.; Wilkop, T. E.; Cheng, Q. On-Demand Formation of Supported Lipid Membrane Arrays by Trehalose-Assisted Vesicle Delivery for SPR Imaging. *ACS Appl. Mater. Interfaces* **2015**, *7* (31), 17122–17130.

(28) Wang, Z.; Wilkop, T.; Cheng, Q. Characterization of Micropatterned Lipid Membranes on a Gold Surface by Surface Plasmon Resonance Imaging and Electrochemical Signaling of a Pore-Forming Protein. *Langmuir* **2005**, *21* (23), 10292–10296.

(29) Linman, M. J.; Cheng, Q. J. Surface Plasmon Resonance: New Biointerface Designs and High-Throughput Affinity Screening. In *Optical Guided-wave Chemical and Biosensors I*; Zourob, M., Lakhtakia, A., Eds.; Springer Berlin Heidelberg: Berlin, Heidelberg, 2009; pp 133–153.

(30) Liu, Y.; Dong, Y.; Jauw, J.; Linman, M. J.; Cheng, Q. Highly Sensitive Detection of Protein Toxins by Surface Plasmon Resonance with Biotinylation-Based Inline Atom Transfer Radical Polymerization Amplification. *Anal. Chem.* **2010**, *82* (9), 3679–3685.